Studying Electrostatic Polarization Forces at the Nanoscale

Dielectric constant of supported biomembranes measured in air and liquid environment

Georg Gramse

UNIVERSITAT DE BARCELONA

Studying Electrostatic Polarization Forces at the Nanoscale

Dielectric constant of supported biomembranes measured in air and liquid environment

Georg Gramse

Barcelona, May 2012

DOCTORAL THESIS

UNIVERSIDAD DE BARCELONA
Facultad de Física
Departamento de Electrónica

Estudios de Fuerzas de Polarización Electrostática a la Nanoescala

La constante dieléctrica de biomembranas suportadas medido en aire y liquido

Programa de Doctorado:

Nanociencias

Línea de Investigación:

Nanobiotecnología

Director de Tesis:

Gabriel Gomila Lluch

Autor:

Georg Gramse

Contents

1 Introduction

Scientific progress was long confined to its subject areas, but at least since ground braking inventions and discoveries like the double helix model by Watson and Crick it got obvious that interdisciplinarity can often be the key to access still unexplored fields of science. Nanotechnology or Nanoscience is one of the big examples for interdisciplinary fields, since in principle it does not mean anything more specific than science of very tiny things including all the areas from Physics over Chemistry to Biology. I believe to be more interdisciplinary is almost impossible. In a more critical way one might also say that a vaguer definition is impossible. But actually when looking for example at the number of scanning probe techniques for nanoscale characterization that were developed in last 30 years and since then had great impact on science, one finds also that nowadays most of them can be applied to investigate very diverse problems reaching from molecular biology to solid state physics. So at the end, it might be not necessary to be more specific, because all the problems are somewhat related to the type of interaction that occur and that are ultimately determined by the length scale that is the nanometer. Although the context or background, be it Biology or Physics, might be different, when you go to the actual problem the science is the same. I think this is what Nanoscience makes also so attractive and brings many different people together.

My work of the last four years was devoted to the development of a nanoscale characterization technique and to make it more interdisciplinary by extending its application range to the field of Biology. In particular the objective was to develop a novel technique to probe the dielectric properties of biomembranes in their native physiological environment. The dielectric constant of biomembranes is a parameter especially important in cell electrophysiology as it ultimately determines the ion membrane permeability, the membrane potential formation or the action potential propagation velocity, among others. Knowing the dielectric properties of biomembranes

with nanoscale spatial resolution is very important due to the nanoscale hetereogeneous composition of plasma membranes (e.g. lipid rafts). However, no technique is able to provide this quantity with the required nanoscale spatial resolution and in electrolyte solution.

In recent years, AFM has proved to be an extremely powerful tool and today it is a well established technique to image the surface topography of a biological sample at the nanoscale and in its physiological environment. Moreover, it is extremely versatile since it can be combined with many techniques formerly working only at the macro-scale so that today magnetic, optical, electrical and many other properties can be investigated simultaneously with the topography of the sample.

In particular, a vast number of electrical characterization techniques have been developed for the nanoscale electric characterization of materials, mainly driven by the needs of the semiconductor industry since structures were continuously shrinking deep into the nanoscale. Also for organic materials and in the field of biology, electrical properties have been measured at the nanoscale, but in no case the polarization properties of biomembranes could be measured in the physiological environment.

Even for measurements made in air, data interpretation is complex and until now it has been difficult to extract quantitative dielectric constant values from the performed measurements in many cases. This is even complicated further when working with organic samples like biomembranes which very often could not be adsorbed on flat metallic substrates and insulating substrates like glass or mica have to be used.

The other aspect mentioned is that when performing electrical measurements with biomembranes, it is often necessary to work in an ion containing liquid environment to ensure that the function and the natural structure of the biological specimen under investigation is conserved.

The objective of my work was therefore to extend dielectric imaging methods to the liquid environment and to develop a new electric AFM technique and corresponding models that work in ionic solution in order to address the nanoscale dielectric properties of biomebranes their physiological environment. The successful realization of this goal is presented here.

In order to reach this objective, I followed a step by step approach to the problem. In a first step, I investigated further the quantification of the dielectric constant of biomembranes on metallic substrates and in air

environment by using DC Electrostatic Force Microscopy measurements also with the objective to gain deeper insight into the problem. Further, I showed that a conveniently modified approach could be followed for the case that a thick dielectric substrate (like glass or mica more appropriated for biomembranes) was used. In this case AC-EFM was used in order to increase the measuring sensitivity and more effectively decouple the dielectric response from the surface potential properties. Finally, I worked out the adaptation of the previous methodologies to the liquid environment, requiring the introduction of important innovation with respect to the approaches used in air measurements.

The thesis is organized into *eight chapters*. After this *first chapter* I will give a short introduction into AFM techniques for electric and dielectric characterization (*second chapter*). This follows the *third chapter* dealing with the developed methodologies to extract quantitative values of the dielectric constant from the performed measurements. The *fourth chapter* will present the first quantitative nanoscale measurements of the dielectric constant on biomembranes (purple membrane) and thin films on metallic substrates using DC electrostatic force microscopy. Thereafter the *fifth chapter* will deal with the quantitative extraction of the dielectric constant values on insulating substrates. Finally, the *sixth chapter* will be about the first successful polarization imaging measurements of lipid bilayers in ionic solution. The *seventh* and *eighth chapter* will contain a conclusion and an appendix.

2 Electrical Atomic Force Microscopy techniques

2.1 Scanning Probe Microscopy & Atomic Force Microscopy

A **Scanning Probe Microscope (SPM)** is an instrument for surface imaging with the capability to measure a number of physical surface properties with a resolution down to the atomic level. Although just 30 years have gone since its invention, it has proved to be an invaluable tool for investigation in all areas of science starting from solid state physics to molecular biology.

Two fundamental components of a SPM are the scanner and the probe. The scanner is responsible for the precise lateral and vertical positioning of the probe with respect to the sample. It consists of a piezoelectric ceramic that changes its geometry according to an applied voltage with sub-nanometric precision. The probe, brought very close to the sample, interrogates the surface of the specimen using a given physical interaction that reveals a certain local material property. In any case, the interaction sensed by the probe is very sensitive to the probe-sample distance and using a feedback-control that adapts the vertical scanner position, the probe- sample distance can be controlled while scanning the sample laterally in the x and y direction. From the acquired movement of the scanner one can finally reconstruct an image of the studied sample surface as shown in Figure 2.1.

Depending on the kind of probe-sample interaction that is sensed, a vast number of scanning probe techniques with different names have evolved. The first SPM was a scanning tunneling microscope. It was invented by G. Binning and H. Rohrer in 1982[1, 2] and senses a dc tunneling current between the conducting probe and sample.

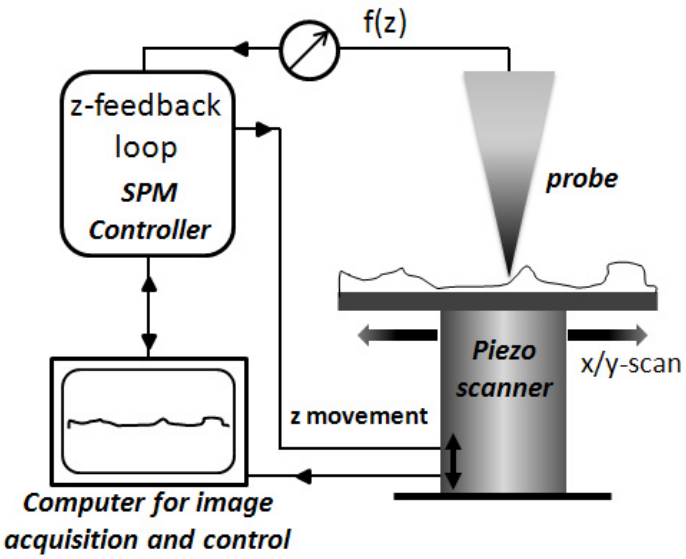

Figure 2.1 *Simplified set up for a scanning probe microscope. The piezo scans the sample laterally and adjusts the tip sample distance, z. The probe senses the sample and gives a signal that is dependent on the probe-sample distance. The control and feedback circuit maintains the probe-sample distance so that a surface image can be acquired.*

The tunneling current goes exponentially with the probe sample separation, what makes the technique so sensitive and enables atomic resolution. However, the measurement of DC-currents requires conductive samples or at least very thin insulating samples on a conductive substrate. The invention of STM triggered the development of the Atomic Force Microscope a few years later and a series of ground breaking results in various fields of science, all based on the strength of SPM techniques to work under natural ambient conditions with resolutions down to the sub-nanometer scale.

The **Atomic Force Microscope (AFM)** or Scanning Force Microscope (SFM) is a surface imaging tool and was invented in 1986 a few years after the STM by G. Binning, C.F. Quate and Ch. Gerber[3] at the Stanford University and the IBM San Jose Research Laboratory. Its development was a consequence of the limitation of STM to conductive samples. In contrast to STM the AFM senses attractive or repulsive *atomic forces* like for example the van-der-Waals force.

The AFM probe consists of a sharp tip with an apex that has just a few tens of nanometers in diameter. To sense the force when the apex interacts with the sample, the tip is located at the free end of a cantilever that is usually between 100 and 400 µm in length. The interaction force leads to a bending of the cantilever that can be measured by the deflection of a laser spot focused onto the cantilever. The deflection is registered by a position sensitive four quadrant photo-diode giving the cantilever position with sub-nm precision as shown in Figure 2.2. In this way, depending on the dimensions of the cantilever, it is possible to measure forces down to the range of pN, just limited by the thermal noise.

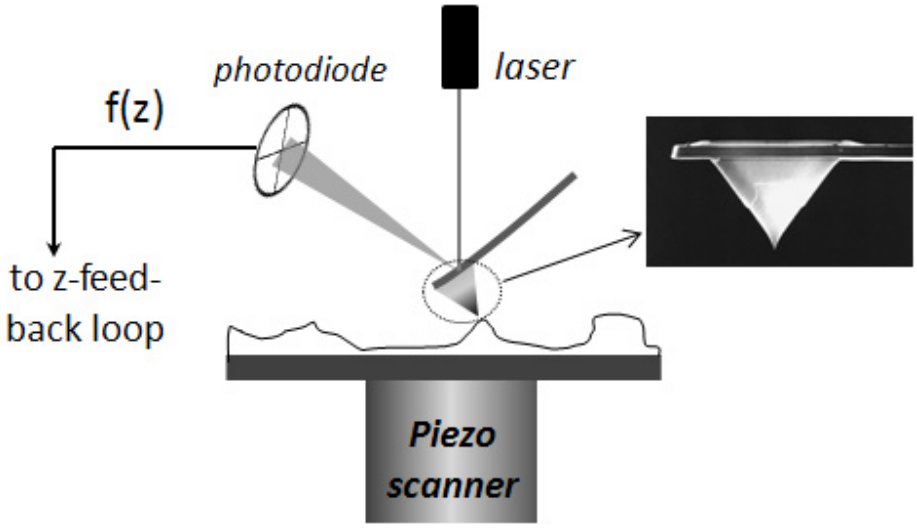

Figure 2.2 *Atomic Force Microscope a special type of SPM. The probe consists of a very sharp tip mounted at the free end of a cantilever that bends when the probe senses the sample. The bending is precisely acquired by a position sensitive photodiode sensing the deflection of a laser beam reflected on the backside of the cantilever. The probe-sample distance dependent signal is used to maintain the contact with the sample and acquire an image like in Figure 2.1. The inset shows the side view of the cone and cantilever obtained with SEM (source: AFM-tip catalogue from Atomic Force at www.atomicforce.de).*

2.1.1 AFM Topography scanning modes

Most commonly Atomic Force Microscopy is used to scan the topography of the sample surface. As mentioned earlier, the interaction typically sensed in this case is the short range van-der-Waals force. The van-der-Waals Force can be attractive or repulsive depending on the distance between the sample and probe and according to which part of the force is sensed in the AFM-experiment, different operation modes were developed. A schematic of the van der Waals interaction potential as a function of the probe-sample distance is shown in Figure 2.3. At far distance (typically >5-10 nm) the potential is zero and no force is sensed. Reducing the distance the force gets attractive and one speaks of the *non-contact* region. Approaching further the potential rises again and for very close distances the interaction force is repulsive and rises steeply when probe and sample continue to approach. AFM images acquired in the repulsive region of the van-der-Waals potential are acquired in *contact* whereas when working in both the repulsive and the attractive region one speaks of the *intermittent contact* region.

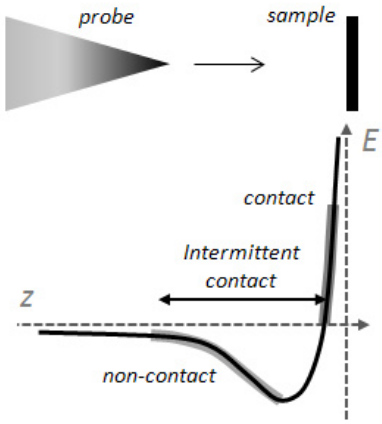

Figure 2.3 *Interaction regimes for Atomic Force Microscopy. At large separations when the sensed forces are just attractive images are acquired in non-contact. At close distance and repulsive forces – contact mode. Covering both ranges - intermittent contact mode.*

Contact mode

Contact mode works in the repulsive region of the interaction potential. It is usually performed with soft cantilevers (k<1N/m) to avoid the damage of the sample surface. There are two different operation modes: The constant height mode where the probe remains at a fixed vertical distance in contact on the sample, while the piezo is scanning the sample in x and y direction without any feedback activated. From the acquired deflection of the cantilever in each point one can obtain the sample topography. This mode is preferable for very flat samples and where fast scanning is desired. On samples with big topography changes one has to assure that the interaction force is not changing too much, what can lead to modifications of the probe or the sample, and one fixes its value by defining a force set-point. An electronic feedback between the cantilever deflection signal and the scanner elongation maintains the force then constant. This constant-force mode is much gentler to probe and sample, but the available scanning speed is usually limited by feedback circuit.

Amplitude modulation mode

The amplitude modulation mode, or depending on the AFM-company also called dynamic or tapping mode™, is operated in the intermittent contact region. It is a dynamic mode where instead of measuring just the static cantilever-deflection in contact, the cantilever gets excited to oscillate at its mechanical resonance frequency. The amplitude of the oscillation gets precisely detected by measuring the oscillation of the photodiode signal with a lock-in amplifier. The lock-in amplifier is very sensitive, since it is able to cancel out noise in the frequency range that does not agree with the excitation frequency.

The excitation is usually realized in a so called acoustic mode with the help of a small piezo mounted close to the cantilever chip. But there exist also alternative modes that excite the cantilever oscillation by varying magnetic

forces (eg. MAC-Mode™) or thermally using an additional laser heating up the cantilever and inducing a bending[4, 5]. These alternative excitation modes have been proven to be especially effective when AFM is performed in liquid environment where sometimes the acoustic mode leads to an increased noise and instabilities, since it excites not only cantilever oscillation modes but also mechanical modes in the liquid.

The measured oscillation amplitude is finally used to drive the feedback that keeps the distance between tip and sample constant. Therefore one defines a set-point for the amplitude smaller than the oscillation amplitude out of contact that is maintained during the scan by the feedback control-circuit as shown in Figure 2.4.

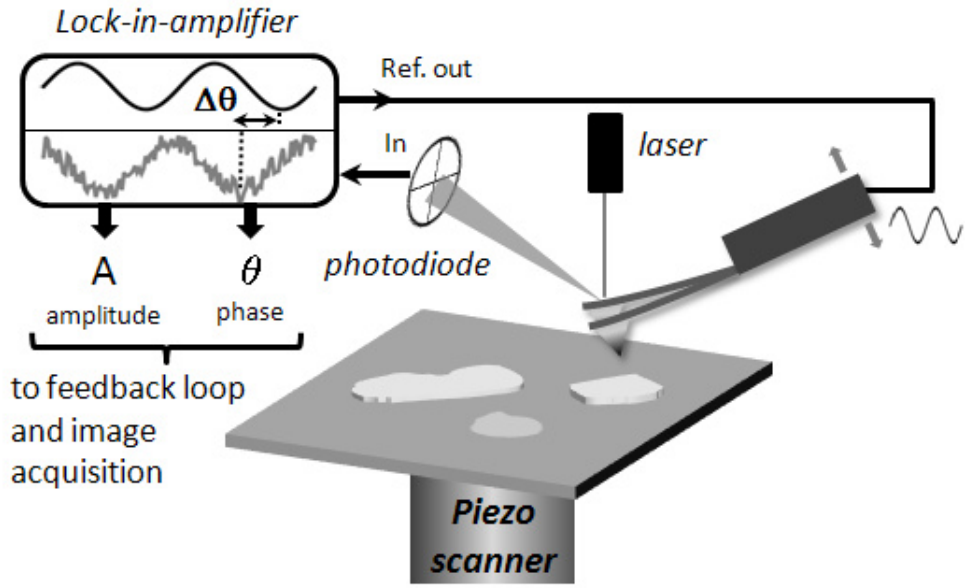

Figure 2.4 *Set up for amplitude modulation AFM. The cantilever is excited mechanically to oscillate at its resonance frequency. The oscillation is monitored by the deflection of the laser spot on the photodiode. A lock-in amplifier detects from this oscillation the amplitude and phase of the cantilever oscillation that change when getting into contact with the sample. The amplitude signal is used to maintain the probe sample distance and acquire a topography image.*

The big advantage of the amplitude modulation mode is that it is less invasive than contact mode, since the interaction can be tuned to be much softer. There is also no lateral force present during scanning that can lead to a modification of the sample like in contact mode. In general amplitude modulation mode is very effective and can be used on nearly any kind of sample allowing also the scan of very big areas. Usually cantilevers with a higher spring constant (*k>1 N/m*) are used so that the resonance frequency is high enough (f_{res}*>10 kHz*) and the increased quality factor leads to good signal to noise ratios. This is especially important in liquid where the resonance frequency drops by about 50% due to hydrodynamic drag.

Apart from the amplitude that is used to measure the sample topography, the lock-in also acquires the phase shift of the cantilever oscillation with respect to the excitation signal for every image point. This phase image gives access to additional material properties like the stiffness of the sample or the local adhesion. These properties allow the detection of changes in the material composition or simply differentiation of different materials that cannot be detected by the topography.

Non-contact frequency modulation AFM

To acquire AFM-images sensing the attractive forces in the non-contact regime, again, the cantilever has to be oscillated at its resonance frequency. To sense the force, the microscope detects the change of the oscillation amplitude or the shift of the cantilever resonance frequency with a phase lock loop circuit to maintain the feedback.

To understand in more detail how the frequency shift or modulation image is generated, one has to take a look at the mechanics of the cantilever. Assuming the cantilever is a damped oscillator (damping γ, mass m) that gets excited by some external periodic force $F_{ext}(t)$, the differential equation for the cantilever movement satisfies, in a lumped element description:

$$m\frac{d^2z(t)}{dt^2}-\gamma\frac{dz(t)}{dt}-k\cdot z(t)=F_{ext}\left(t\right) \tag{2.1}$$

Under the condition that the force is just time dependent, the solution of this system is well known and given by the equations (2.2)-(2.6) (see a plot of the harmonic oscillator amplitude in the frequency space in Figure 2.5).

$$A(w)=\frac{F_{el}/m}{\left[\left(\omega_r{}^2-\omega^2\right)^2+\frac{\omega_r^2\omega^2}{Q^2}\right]^{1/2}} \tag{2.2}$$

$$\tan\phi=\frac{\omega_r\omega/Q}{\omega_r{}^2-\omega^2} \tag{2.3}$$

$$\omega_r=\omega_0\sqrt{1-\frac{1}{2Q^2}} \tag{2.4}$$

$$\omega_0=\sqrt{\frac{k}{m}} \tag{2.5}$$

$$Q=\sqrt{\frac{\omega_0 m}{\gamma}} \tag{2.6}$$

However, when imaging, the tip feels an additional interaction that can be the the van-der-Waals-Force or an electrostatic force. These forces are dependent on the distance between tip and sample, especially when approaching close to the surface, and couple with the motion of the cantilever. To see the effect one can follow a perturbation approach and the force resulting from the interaction with surface can be developed by:

$$F_{vdW}(z_0+z(t),t)=F(z_0)+\frac{\partial F(z_0)}{dz}(z(t)-z_0)+\ldots \tag{2.7}$$

For small cantilever displacements, it is sufficient to consider the first two terms that are shown. Putting this into equation (2.1) we find that the spring constant and the resonance frequency get modified to:

$$\tilde{k}=k+F'(z_0) \tag{2.8}$$

$$\tilde{\omega}_0=\sqrt{k-F'(z_0)\big/m}=\omega_0\sqrt{1-\frac{F'(z_0)}{k}} \tag{2.9}$$

This result is graphically displayed in Figure 2.5 and explains why detecting the shift of the resonance frequency yields the gradient of the sensed force.

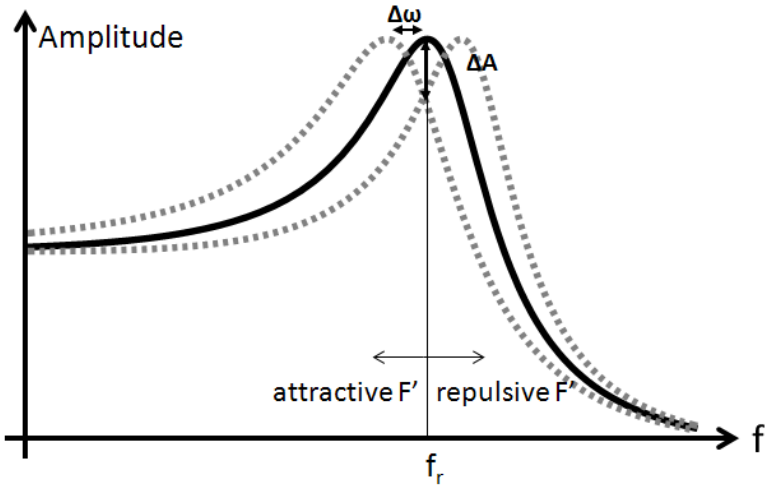

Figure 2.5 *Shift of the cantilever resonance peak due to the effect of a force gradient acting on the cantilever.*

Since the measured forces are much smaller than in contact or intermittent contact mode and the cantilevers have to be chosen very stiff in this mode (k>10N/m), the oscillation-detection has to be more sensitive compared to the other modes, thus making it more difficult to maintain a good feedback in non-contact AFM.

2.2 Atomic force microscopy techniques for electrical characterization

Like in STM it is possible to measure also electrical properties with an AFM. In this case it is necessary to use conductive probes, additional electronics and usually a conductive substrate to apply an electric field between the tip and the substrate. The big advantage of AFM with respect to STM is that it offers the possibility to measure the topography simultaneously with the electric property of interest, because the probe sample distance can be controlled independently. Another advantage is that also measurements on thicker insulating samples are possible.

A number of electrical characterization techniques have been developed over the years each specific to probe different material properties. In the scheme in Figure 2.6 the most important of them are shown. In general, one has to distinguish between two different approaches:

1. *Current detection techniques* where the current flowing from substrate to tip is measured to access the electrical property of interest.

2. *Force detection techniques* where the electrostatic force induced by the applied electric field is measured by the bending of the cantilever which depends on the electric property of interest.

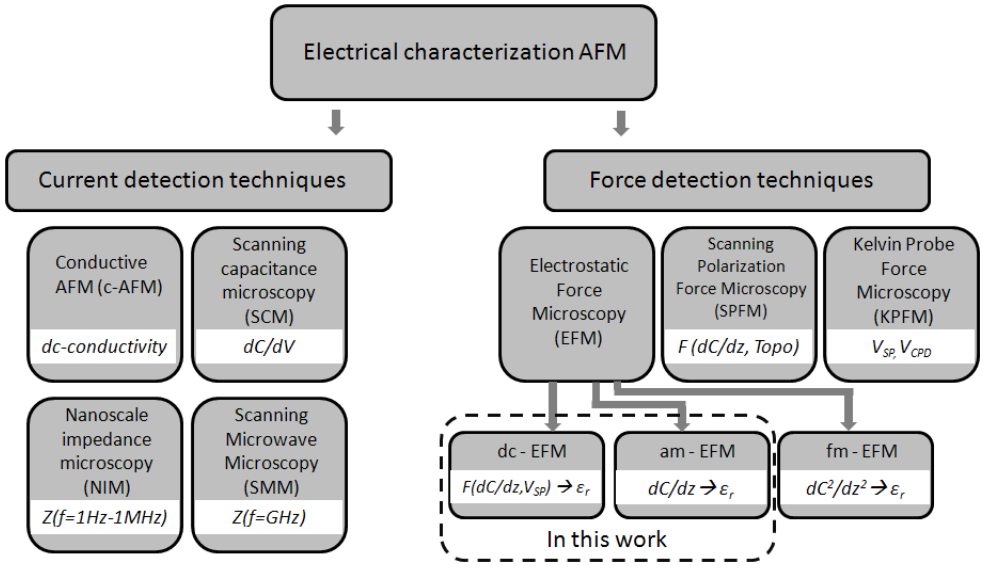

Figure 2.6 *Classification of AFM-techniques for electrical characterization. The measured electrical property is shown with the white background. This work is focusing on EFM-techniques.*

2.2.1 Conductive Atomic Force Microscopy

In conductive Atomic Force Microscopy (C-AFM) the DC current, I_{dc}, is measured when applying a DC voltage between tip and substrate. To measure I_{dc} a current to voltage amplifier is mounted close to the tip as shown in Figure 2.7 and the tip is kept in electrical contact with the sample. In this way the conductivity of a sample at a fixed DC-potential can be imaged while scanning the topography in contact mode. Alternatively, it is also possible to acquire *I/V*-curves on certain points of interest of the sample to study the resistivity and its voltage dependence of the sample. A very much related technique is scanning spreading resistance microscopy (SSRM).

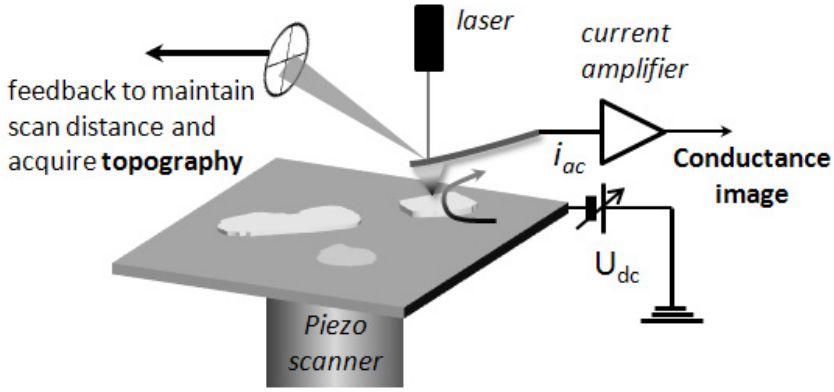

Figure 2.7 *Experimental set up for Conductive Atomic Force Microscopy.*

It basically consists of the same setup and usually a logarithmic amplifier is used to measure currents. To maintain good contact the surface is scanned with high load. Therefore usually very hard probes with diamond coating are used[6]. SSRM was mainly applied to characterize semiconductor structures[7, 8] and lateral resolutions down to one nanometer can be reached.

2.2.2 Scanning Capacitance Microscopy (SCM)

In Scanning Capacitance Microscopy a high frequency *AC* potential (GHz range) is applied between tip and sample to measure with an electronic resonance circuit the change of the capacitance between sample and tip. To investigate the dependency of the differential capacitance on the DC-potential of the sample one applies an additional DC-potential to the sample. To improve sensitivity the DC-potential can also be modulated at low frequency (some kHz) to make use of lock-in detection and to obtain the differential capacitance (*dC/dV*). The concept of SCM was already developed[9] in 1985 and subsequently improved[10]. Today SCM is a standard technique to probe the dopant concentration in a semiconductor at the nanoscale. A schematic of the nowadays commercially available set up for SCM is shown in Figure 2.8. The

probe scans the sample in contact and the AC voltage is applied in parallel.

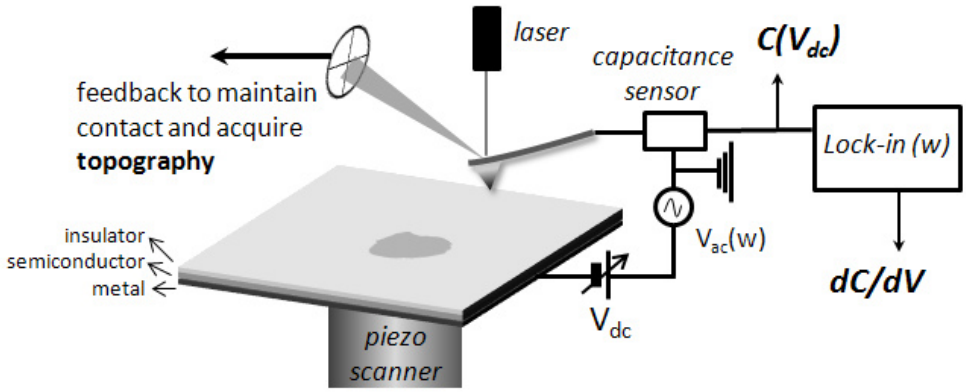

Figure 2.8 Experimental set up for Scanning Capacitance Microscopy (SCM) for imaging the dopant concentration in a semiconductor covered by a thin insulating oxide layer.

2.2.3 Nanoscale Impedance Microscopy (NIM)

In order to investigate electrical transport processes in the frequency regime, an AC-current sensing technique that is able to measure the impedance *Z(ω)* was recently developed[11]. Within the here presented current sensing techniques Nanoscale Impedance Microscopy is the least developed one and still not commercially available.

NIM can be run in imaging mode in order to acquire an impedance image at a fixed frequency simultaneously with the topography or it can be run in spectroscopy mode where the probe is kept fixed in one point of the sample and an impedance spectrum is acquired.

An AC-voltage is applied between the conducting tip and the substrate. But in contrast an impedance analyzer is used to measure directly the impedance *Z(ω)*[11, 12].

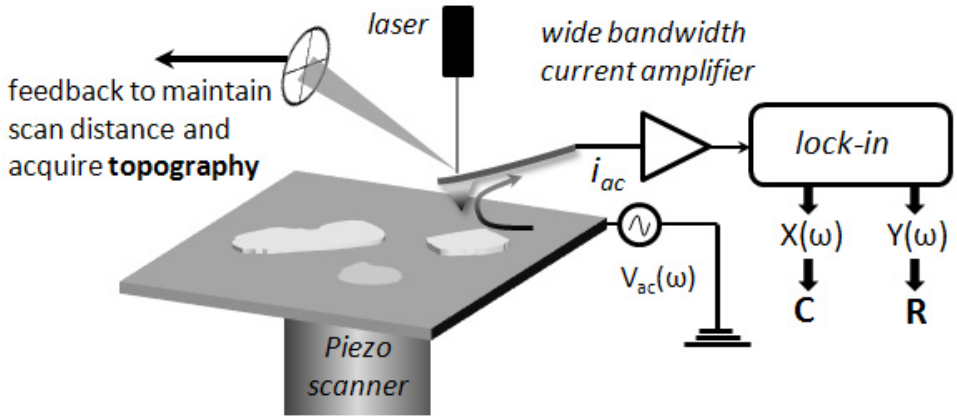

Figure 2.9 *Experimental set up for Nanoscale Impedance Microscopy (NIM) with the implementation consisting of a wide bandwidth current amplifier and a lock-in to demodulate resistive (X) and capacitive (Y) current.*

Another approach is to detect the very small AC-current flowing from the tip using a low-noise current-to-voltage amplifier and couple it with a lock-in detector to obtain the capacitive and resistive current and so the impedance *Z(ω)*[13, 14]. An important difference with conductive AFM is that this technique probes both the (AC) conductivity and dielectric properties of the samples. For this reason it can be used in non contact mode if desired.

Based on the former approach, in recent years our group developed methodologies and instruments to measure the local capacitance of insulating samples at the nanoscale like for example oxide thin films[15-18] or even 5nm thin biomembrane patches[19]. The main goal of these measurements was to extract in a quantitative way the local sample capacitance and its local dielectric constant. For this reason we introduced the names *Nanoscale Capacitance Microscopy* (NCM) and *Nanoscale Dielectric Microscopy* (NDM) for the developed methodologies and techniques.

Contrary to the case of DC measurements, in AC measurements a major difficulty appears, namely, that the measured electric current has capacitive contributions associated to the whole AFM-probe including the chip and non-screened connecting cables. These so called *stray capacitances* are orders of magnitude bigger (~30fF) than the local capacitance of the very end of the tip (10aF) that is actually of interest for our measurement. Therefore an ultra-

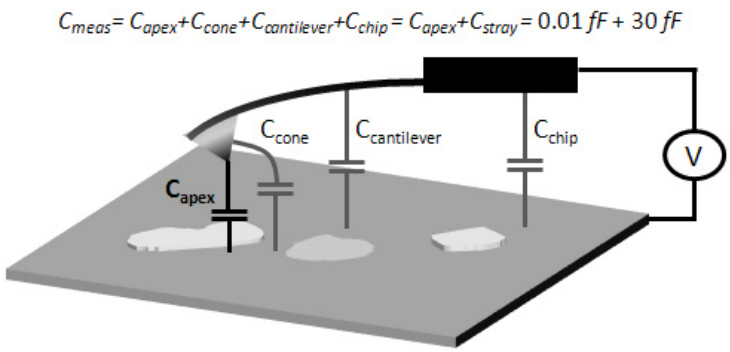

Figure 2.10 *Schematic of the tip sample configuration with involved capacitances in a NIM-experiment.*

sensitive amplifier had to be developed capable of still resolving local capacitance signals[15, 20]. To illustrate these complexities, Figure 2.10 shows a schematic drawing of the tip-substrate configuration and involved capacitances.

Finally, the capacitance difference between having a 5nm thin bio-membrane and the bare metallic substrate is in range of 1aF. To resolve such differences, stray capacitances have to be carefully shielded and then **noise levels of 0.1aF** need to be reached[19] using still reasonable averaging times compatible with AFM imaging.

Further challenges for NCM arise from the interpretation of the measured capacitance in order to extract a local dielectric constant. As will be shown in chapter 3 the measured capacitance depends on the geometry of the conductive AFM-probe so that a calibration of the tip geometry before or after imaging is necessary. Apart from this it has been demonstrated that the capacitance signal is more sensitive to the tip substrate distance than to the dielectric properties of the sample. In consequence capacitance imaging has to be performed out of contact at constant height above the substrate, to prevent contributions coming from the vertical movement of the scanning stage.

2.2.4 *Scanning Microwave Microscopy (SMM)*

Scanning Microwave Microscopy (SMM) is a technique that complements NIM at higher frequencies from 0.1-100 GHz, but its frequencies lie below those used in optical SPM-techniques like Near-field Scanning Optical Microscopy (NSOM) (>THz). Like NIM, also SMM has the capability to image conductivity and dielectric properties at the nanoscale. Nanoscale studies with SMM have been conducted on different types of materials reaching from solid state materials to biological samples[21, 22]. SMM has been made only recently available on commercial AFM-products. In SMM the magnitude measured is the microwave scattering parameters (S-parameters) which can be related to the local impedance of the probe substrate system.

The general experimental setup of SMM is shown in Figure 2.11. The two main differences with respect to NIM are the employed probe and the electronics to generate the microwave and detect it. The function of the probe is to conduct the microwave signal to the very end of the probe that acts like an antenna and emits the microwave-signal. First implementations used needle like probes[23], but recently also cantilever-based probes were developed[24, 25] that are compatible with commercially available AFM-systems. Like in NIM an important issue in the design of the probes is the stray contribution arising

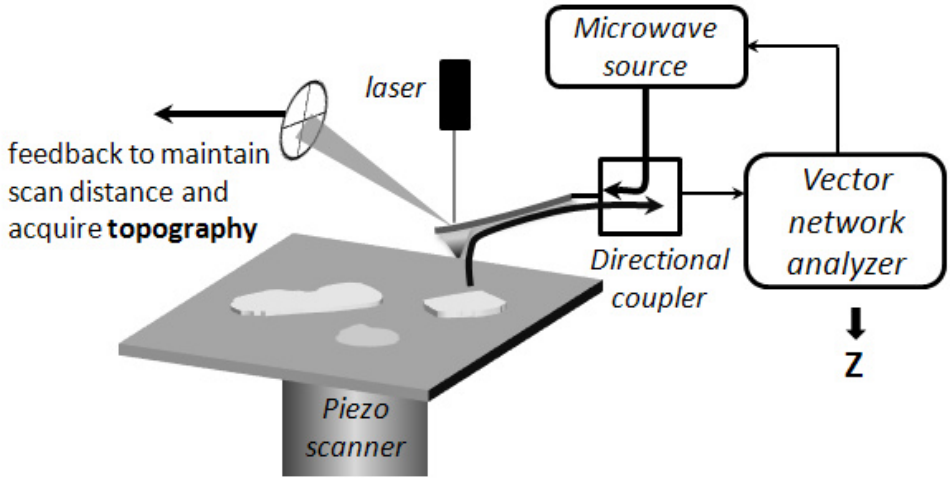

Figure 2.11 *Simplified experimental set up for Scanning Microwave Microscopy (SMM).*

from the nonlocal parts of the tip (like cantilever and so on) that have to be shielded to improve sensitivity[21].

There are different solutions to realize the electronics detecting the microwave signal. The implementation that is commercially available from *Agilent Technologies* consists of a network analyzer that sends a microwave signal through a diplexer to the probe. The signal gets reflected and travels through the tip back to the network analyzer where it gets separated into the reflection scattering coefficient (S_{11}) which is related to the local impedance probed by the tip. Typical noise levels of such setups are in the range of 1aF[22].
One of the great difficulties in SMM is like in NIM the quantitative extraction of the electric and dielectric properties of the sample from the measured impedances. Therefore adequate models have to be developed that take into account the specific tip geometry. This goal can be achieved to some extend by analytical approximations and finite element modeling[26, 27]

2.2.5 DC-Electrostatic Force Microscopy (DC-EFM)

The basis of all electric force sensing AFM techniques is the attractive force that arises when applying an electric field, V_0, between the conductive probe and the substrate that reads:

$$F_{el}(z,\varepsilon_r) = -\frac{1}{2}\frac{\partial C_T(z,\varepsilon_r)}{\partial z}\left(V_0 + V_{sp}\right)^2 \tag{2.10}$$

Here z is the distance between tip and sample and C_T is the total capacitance between the cantilever probe and the sample. (Note, different than in cs-AFM the chip and cables do not contribute). This *electrostatic force* can be sensed by the bending of the cantilever and essentially two material properties, the surface potential, V_{sp}, and the sample dielectric constant, ε_r, can be extracted from the measured signal. Experimentally the simplest way to get information on ε_r and V_{sp} is to apply a dc potential, V_0, and to measure the static bending of the cantilever (DC-EFM).

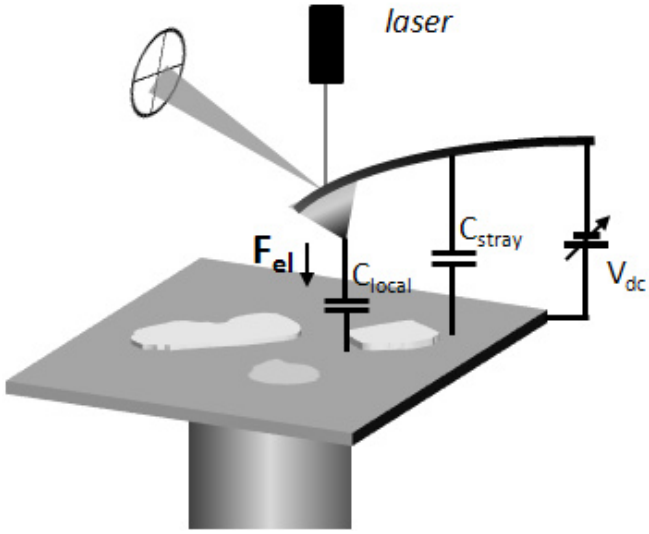

Figure 2.12 Experimental set up for DC Electrostatic Force Microscopy (DC-EFM).

In principle to extract for example ε_r from the force signal, V_{sp} has to be already known, but when working with high applied DC-voltages the error induced by an unknown V_{sp} is negligible.

Also, the sensitivity is limited by thermal and other, for example electronic noise. However, it is a very clear and simple method, as I will show in detail in chapter 4 and it is possible to extract a quantitative value of the dielectric constant of thin insulating films from measurements in this mode.

2.2.6 Amplitude Modulation Electrostatic Force Microscopy (AM-EFM)

To get information on both the capacitance gradient and the surface potential separately a dynamic detection scheme has to be applied. Therefore an alternating voltage

$$V = V_0 \sin(\omega t) \tag{2.11}$$

with the frequency ω is applied between tip and substrate. This voltage leads to a static electrostatic force, F_{dc}, a force oscillating at the excitation frequency F_ω and a force oscillating at the double of this frequency $F_{2\omega}$:

$$F_{dc}(z) = -\frac{1}{2}\frac{\partial C_T(z)}{\partial z}\left[\frac{1}{2}V_{ac}^2 + \left(V_{dc} + V_{sp}\right)^2\right] \tag{2.12}$$

$$F_{\omega}(z) = -\frac{\partial C_T(z)}{\partial z}\left(V_{dc} + V_{sp}\right)V_{ac}\sin(\omega t) \tag{2.13}$$

$$F_{2\omega}(z) = \frac{1}{4}\frac{\partial C_T(z)}{\partial z}V_{ac}^2\cos(2\omega t) \tag{2.14}$$

The second harmonic force, $F_{2\omega}$, just contains information on the capacitance, C_T, of the system and so also on the dielectric constant of the sample. However, the capacitance is not a simple function only of the sample dielectric constant, it also depends on the nanoscopic and microscopic geometry of the probe as will be detailed in chapter 3.

The harmonic forces F_{ω} and $F_{2\omega}$ can be precisely measured using the detection scheme shown in Figure 2.13. The lock-in amplifier excites the oscillation by applying the ac-voltage well below the resonance frequency of the cantilever. This oscillation are acquired by the photodiode and the amplitudes at the first and second harmonic (*A(ω), A(2ω)*) of the excitation frequency get measured by a lock in amplifier. Finally, by calibrating the spring constant of the cantilever, the corresponding electrostatic force can be calculated.

As mentioned before the advantage of AM-EFM is the high sensitivity (due to the lock in detection scheme) and the possibility to measure the force related to the capacitance and to the surface potential separated by the two harmonics. Although the first harmonic signal, *A(ω)*, contains contributions from both components, it is possible to calculate the surface potential by dividing *A(ω)* and *A(2ω)* as has been shown[28]. Another more common approach to obtain the surface potential is shown in section 2.2.8. The lowest detectable force is: [29]

$$F_{\min} = \sqrt{\frac{2 \cdot k \cdot k_B \cdot T \cdot Bw}{\pi \cdot Q \cdot \omega_r}} \tag{2.15}$$

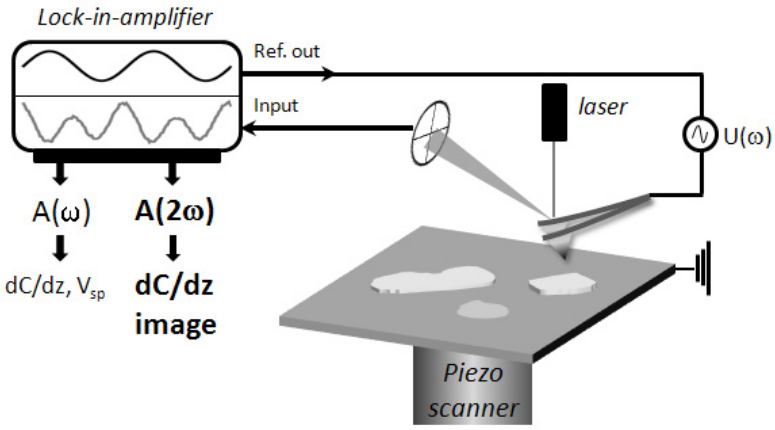

Figure 2.13 *Experimental set up for Amplitude Modulation Electrostatic Force Microscopy (AM-EFM).*

(k_B Boltzmann constant, T temperature, Bw lock-in bandwidth, Q cantilever quality factor, ω_r resonance frequency).So for typical values of k=0.1 N/m, Bw=100 Hz, Q=100 and ω_r=30 kHz would give F_{min}=0.1 pN or with V_{ac}=3 V **the minimal detectable capacitance gradient is $dC_{T,min}/dz$= 0.02 zF/nm**. This is almost four orders of magnitude better than what is currently possible with current sensing methods.

2.2.7 Frequency Modulation Electrostatic Force Microscopy (FM-EFM)

Apart from the amplitude modulation mode, EFM can also be operated in frequency modulation mode what can improve the resolution of the electric image. As has been shown in section 2.1.1, an electrostatic force acting on the cantilever leads to a modification of the spring constant, k, what leads to a frequency shift of the resonance frequency. The measured frequency shift, $\Delta\omega$, is related to the force gradient by[30]:

$$\Delta\omega = \frac{\omega_0}{2k}\frac{\partial F}{\partial z} \tag{2.16}$$

where ω_0 the free resonance frequency and z the probe-sample separation. This shift oscillates with the frequency of the applied electric potential and can be detected. The experimental realization of FM-EFM is schematically shown in Figure 2.14. It requires two lock-in amplifiers. Like in AM-EFM one applies with a first lock-in the alternating electric field of the frequency ω_{el} between tip and sample. Simultaneously, the cantilever is excited mechanically at its resonance frequency by the second lock-in. The electrical excitation leads to a shift of the mechanical resonance frequency that oscillates with ω_{el} ($\Delta\omega_r=\Delta\omega_{r,0}$ $sin(\omega_{el}t)$). Notice, ω_{el} should be clearly lower than the resonance frequency. The oscillating resonance frequency gets locked by the second lock-in using a phase lock loop circuit. This signal is fed into the first lock-in where the amplitude of the frequency shift, $\Delta\omega_{r,0}$, is measured.

The advantage of such a heterodyne detection scheme like it is used in FM-EFM is that the measured force gradient is more local since it suppresses further the nonlocal contributions from cantilever and cone. Nevertheless, it is more complex and the additional PLL-feedback loop makes a further calibration neccessary[31].

The minimal detectable force gradient in this method is:

$$F'_{\min} = \sqrt{\frac{4 \cdot k \cdot k_B \cdot T \cdot Bw}{Q \cdot \omega_r \cdot A_{\omega_r}^2}} \tag{2.17}$$

(k_B Boltzmann constant, T temperature, B_w lock-in bandwidth, Q cantilever quality factor, ω_r resonance frequency, A_ω mechanical oscillation amplitude). So for typical values of A_ω=5nm, k=0.1 N/m, Bw=100 Hz, Q=100 and ω_r=30 kHz

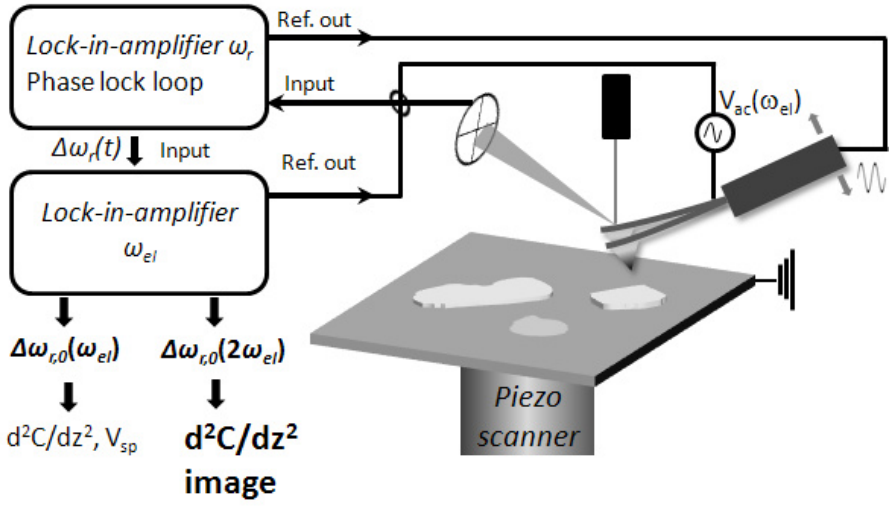

Figure 2.14 *Experimental set up for Frequency Modulation Electrostatic Force Microscopy (FM-EFM). The technique provides the electrostatic force gradient or the second derivative of the capacitance.*

would give F_{min}=0.05 pN/nm or with V_{ac}=3 V the **minimal detectable capacitance gradient** is $d^2C_{T,min}/dz^2$=**0.01 zF/nm²**.

2.2.8 Kelvin Probe Force Microscopy (KPFM)

Kelvin Probe Force Microscopy was invented in 1991[32] and is an EFM mode especially dedicated to measure the surface potential, V_{sp}, or the work function, W_a, of the sample. The surface potential is related to the surface charges on the sample and they are of special interest on biosamples[33], organic samples[34] but also on inorganic samples like graphene[35]. Studies of the local work function are mainly performed on materials like semiconductors [36, 37].

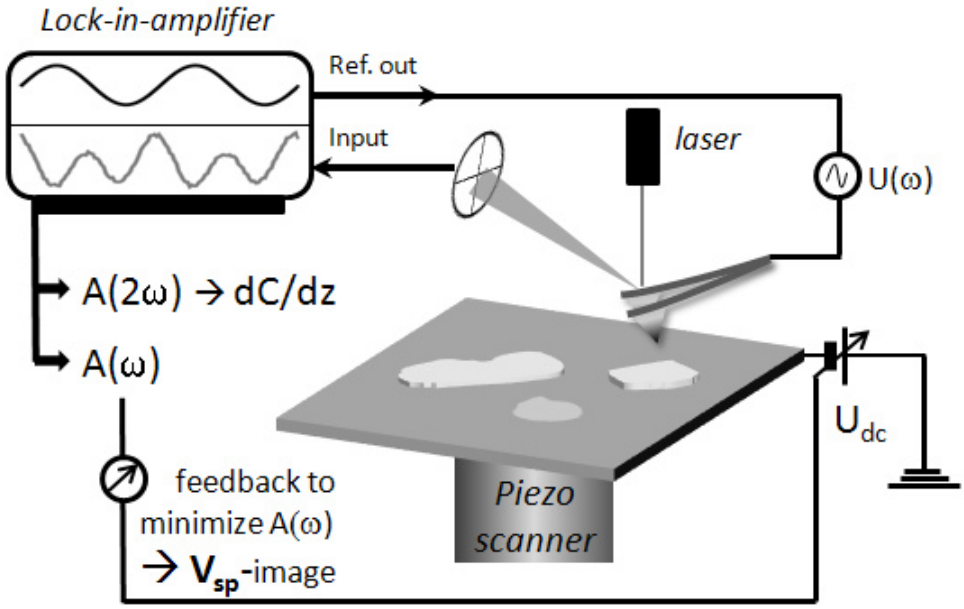

Figure 2.15 Experimental set up for Kelvin Probe Force Microscopy (KPFM). KPFM can be run in AM (shown here) or FM mode. An additional feedback tries to cancel out the first harmonic signal to obtain the surface charge.

The experimental set up for KPFM is the same like in FM-EFM or AM-EFM, but in order to get direct access to the local surface potential or work function, an additional feedback is applied that tries to minimize the first harmonic amplitude A(ω) by applying a dc potential at the sample as shown in Figure 2.15. The first harmonic amplitude is exactly zero when the dc-potential is opposite of the surface potential, as can be seen from equation (2.13).

The applied DC-potential is acquired simultaneously with the topography and gives direct access to the surface potential without further calculations.

KPFM images can be acquired in two different scanning modes. Either in a single pass mode in tapping acquiring simultaneously topography and surface potential in the same scan line or alternatively in a double pass mode, the so called lift mode™ acquiring first the topography and then retracing the last scan line just lifted a few tens of nanometers above it. The advantage of the single pass method is its speed and higher resolution, however with certain samples there the chance to have crosstalk between topography and surface charge. Today, KPFM is available, both in frequency and amplitude modulation, on many commercially available AFMs. However, its application is limited to the use in vacuum or air.

2.2.9 Scanning Polarization Force Microscopy (SPFM)

Scanning Polarization Force Microscopy is an EFM technique that was developed in 1994[38] and was extensively used to image very thin and soft dielectric materials like water layers[39, 40] that are difficult or impossible to image with conventional AFM-modes. It takes advantage of the relative long range of the electrostatic interaction compared to the van der Waals force in order to realize a real non-contact measurement of the sample. The used experimental set up is similar to the am-EFM set up, but by applying a feedback between the measured A(2ω)-signal and the controller of the piezo z-movement the probe-sample distance is controlled like shown in Figure 2.16. Beside the topography also variations of the ionic mobility and the surface potential can be measured[41-43] when an additional feedback is applied like in KPFM.

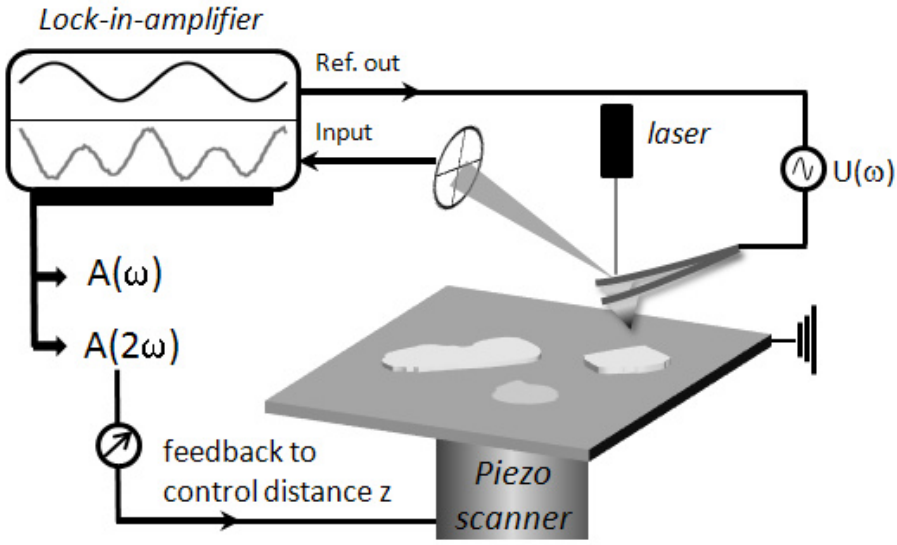

Figure 2.16 *Experimental set up for Scanning Polarization Force Microscopy (SPFM). A feedback with the second harmonic signal controls the probe sample distance.*

2.2.9.1 AFM techniques for electrical characterization in liquid

The study of nanoscale material properties in their natural liquid environment is one of the most import reasons why scanning probe microscopy has become so popular in life science. A liquid and ion-containing environment is not only the natural environment of many organic and inorganic specimen and allows so more realistic studies, it also enables for example (electro)-chemical reactions to take place and therefore to study the specimen in function.

When moving with the AFM from dry into ion containing liquid environment a number of electrical properties change. The most evident one is that the water provides a media where ions and electro-active species can dissociate and move, what leads to a solution conductivity, σ, of the media and to the possibility of electrochemical reactions. Another point is that the dielectric constant of water is clearly higher than in air ($\varepsilon_{r,water}$~78 versus $\varepsilon_{r,air}$=1). Finally, a very important and particular aspect of ionic water-solutions is the formation of *electrical double layers*.

An *electrical double layer* (or just *double layer*) is formed when a metallic electrode surface is exposed to an electrolyte solution. Excess charges from the metal form a space charge region that gets compensated by the adsorption of counter ions from the solution to reach a thermodynamic equilibrium.

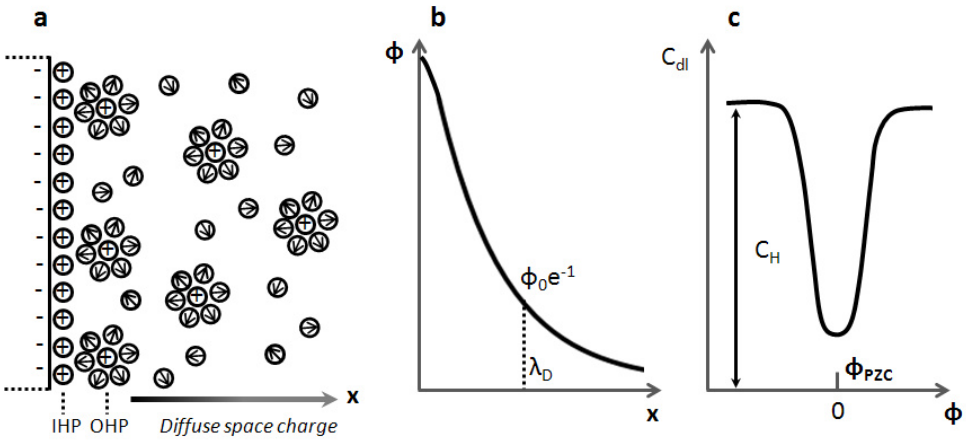

Figure 2.17 *(a) Cartoon of the electrical double layer developing at the charged metal interface. (b) Potential distribution in the double layer: Until the Outer Helmholtz Layer the potential drops off linearly. In the diffuse layer it drops off exponentially. (c) The Double Layer Capacitance in dependency of the electrode potential.*

The locus of this single layer of ions is the so called *Inner Helmholtz Plane (IHP).* The dipoles formed by these two opposite space charge layers attract solvated ions. These solvated ions experience an attractive force, but also possess thermal energy so that they still diffuse around randomly. However, they cannot get closer to the electrode surface than to the so called *Outer Helmholtz Plane (OHP).* The solvated ions, that form the so called *diffuse layer,* exhibit a from the electrode surface nearly exponentially decaying concentration distribution, as shown in Figure 2.17b. In consequence, also the potential drops off in this way. In the limit of small electrode potentials (ϕ<50mV), the potential decay with the distance *x* is:

$$\phi(x) = \phi_0 \cdot e^{-x/\lambda_D}; \lambda_D = \left(\frac{k_B T \varepsilon_0 \varepsilon_r}{2 z^2 e^2 n^0} \right)^{1/2} \approx \frac{0.304nm}{\sqrt{z \cdot c[mol/L]}} \qquad (2.18)$$

Here, *e* is the elementary charge, *z* the number of charges per ion, n^0 the charge concentration, k_B the Boltzmann constant, *T* the temperature, ϕ_0 the electrode potential and c the concentration. The characteristic length of this

decay is defined by the *Debeye Length,* λ_D, that is just 10 nm short for concentrations of 1mM.

As derived for example in detail in textbooks like *Electrochemical Methods* from *Bard & Faulkner*[44] the space charge regions and the diffuse layer lead to the formation of the so called *Helmholtz Capacitance*[45], C_H, and the *Gouy-Chapman-Capacitance*[46], C_G.

$$C_H = \frac{\varepsilon_0 \varepsilon_r}{d_{OHP}} \tag{2.19}$$

$$C_G = \left(\frac{2z^2 e^2 \varepsilon_0 \varepsilon_r n^0}{k_B T} \right)^{1/2} \cosh\left(\frac{ze\phi}{2k_B T} \right) \approx 228\left[\mu F / cm^2 \right] z\sqrt{c[mol/l]} \cosh(19.5z\phi) \tag{2.20}$$

Both capacitances are in series and form the total double layer capacitance, C_d. Also important to notice, the double layer capacitance in this model is potential depend as it was also suggested by experimental observations. It takes its lowest value at the potential of zero charge, ϕ_{PZC}, a characteristic value for every material. For high voltages it gets limited by the Helmholtz capacitance as shown in Figure 2.17c.

This short overview about the properties of the electric double layer should show that the potential distribution at the solution/electrode interface is clearly different than in air. The electric double layer leads to a rapid decay of applied potentials so that electrostatic forces are effectively *shielded*. This has also consequences when detecting electrical currents instead of forces.

I want to emphasize that the above considerations are only strictly valid under static conditions. As reviewed for example by Bazant et al.[47-49] and others[50], at higher frequencies other effect have to be taken into account. In chapter 6 I will also show that under certain conditions for force measurements the effect of double layer capacitance can be neglected.

Scanning Electrochemical Microscopy (SECM)

The most common current sensing AFM-technique in liquid is probably Scanning Electrochemical Microscopy (SECM). Although some SECMs are commercially available, they are often only operated at the microscale since nanometric SECM-probes are difficult to manufacture. SECM is used to probe local electrochemical reactions by applying specific electrochemical potentials to the metallic probe and/or sample using a potentiostat.

To access also the nanoscale, different implementations of the probe have been reported, some using tuning forks in combination with ultramicroelectrodes to acquire topography and electrochemical current simultaneously[51], others use cantilever-tips containing just a small exposed electrode-part close to the apex to sense the current[52]. Though, SECM-AFM is mainly used to sense dc-currents of electrochemical reaction. Only a small number of works apply alternating electric fields and measure the frequency dependent current in AC-SECM. These studies were recently reviewed by Eckhard and Schuhmann[53]. However, none of these works deals with the measurement of dielectric properties of the sample; instead they are centered on the resistive component of the current.

Scanning Microwave Microscopy in liquid (SMM)

Scanning Microwave Microscopy has the great capability to image conductivity but also dielectric properties of the sample under study and this at still relatively low frequencies compared to optical techniques like for example in NSOM. The big difficulty for the operation in liquid solutions consists on the one hand in having probes being sufficiently sensitive to the sample and at the same time keeping the capability to scan the topography. Indeed, recently it has been shown that at the micrometer scale a scanning microwave microscopy can be also operated in liquid using a NSOM-like tuning fork detector to control the tip sample distance[54]. Maybe in the near future it will be possible to increase the resolution of such systems and also cantilever based probes in principle might be operative in liquid at some point.

On the other hand a mayor complexity lies in the very different electric properties in solution (high conductivity and dielectric constant) that will also require new theoretical models in order to reach quantitative results like in air. For these reasons until now, SMM has not been shown to provide quantitative dielectric imaging in liquid environment.

2.2.10 Electrostatic Force Microscopy in liquid

The formation of the electrical double layer at the surface of a two charged electrode surfaces separated a certain distance z from each other, leads to the development of an electrostatic force[55, 56]. Using an AFM these forces can be measured and quantified assuming the AFM-tip to be a cone with a sphere as apex and solving the Poisson-Boltzmann equation. Therefore one has to assume that either tip and substrate are at constant potential (cp) or that they have a constant charge (cc). Then, as has been shown further revised by Butt et al.[57, 58], the force evolving from the double layer interaction of such a tip with a planar surface is:

$$F_{el}^{cc} = \frac{2\pi\lambda_D R}{\varepsilon_0\varepsilon_r}\left[2\sigma_s\sigma_t e^{-z/\lambda_D} + (\sigma^2{}_s + \sigma^2{}_t)e^{-2z/\lambda_D}\right] \tag{2.21}$$

$$F_{el}^{cp} = \frac{2\pi R\varepsilon_0\varepsilon_r}{\lambda_D}\left[2\psi_s\psi_t e^{-z/\lambda_D} - (\psi^2{}_s + \psi^2{}_t)e^{-2z/\lambda_D}\right] \tag{2.22}$$

In these equation ψ_t *(*σ_t*)* and ψ_s *(*σ_s*)* is the potential (surface charge) of the tip and the substrate, respectively, R the apex radius and λ_D is the Debye length, introduced earlier. Recently, also alternative approaches like the *constant regulation approximation*[59] that combine both conditions were proposed.

By the direct measurement of these double layer forces with AFM, a number of studies have contributed in the last 20 years a lot to the basic understanding of charged interfaces in electrolyte solutions. Investigations were carried out studying the electric double layer of noble metals like gold[60-66] for various sorts

of ions and concentrations applying different DC-potentials at the sample with a (bi-)potentiostat. Also other materials like HOPG[62], semiconductors[67] or gold with thin adsorbed SAM-layers[68] were studied. As mentioned, most of these publications were performed under potential control using a potentiostat.

Other authors worked with insulating AFM-tips (SiN) and substrates (mica) in the constant charge condition, investigating for example the surface charges of phospholipid-membranes[69-71]. In these studies, images of the electrostatic double layer interaction-force acquired in lift mode, show that it is possible to distinguish different types of phospholipids by their surface charge. It was also argued, that the dipole potential of the phospholipid-headgroup can be measured[70]. In other works patches of bacteria membrane were studied[72]. Also recently, DNA molecules on flat substrates could be resolved sensing their electric double layer[71, 73].

However, all studies mentioned so far in this section were performed measuring the static double layer interaction and so probing the surface charges. In contrast, almost no work is dealing with the detection of the AC electrostatic force like it can be performed with **AM-EFM** in air (cp. section 2.2.6). The first who tried to perform AM-EFM in liquid by using a bipotentiostat were Hirata et al.[74] They could show for solutions of very low ion concentration (c<0.1mM) and at low frequency that one can measure some electrostatic force and they acquired force versus distance curves. Nevertheless, the origin of this force was not clear and the same theoretical background like in air was used to interpret the experiments. Indeed studies from Raiteri et al.[75] indicate that the measured forces are mainly induced by electrochemical surface stress of the cantilever or the presence of electrochemical reactions. Also other authors follow this argumentation[76]. However, recently a new method was proposed[77] to the probe surface charge in the AM-EFM mode but using slightly higher frequencies up to 30 kHz. As will be shown in chapter 6, I share the idea to use higher frequencies to perform AC-EFM in ionic solution with the aim to investigate dielectric sample properties, but theoretical considerations will show that much higher frequencies are necessary to obtain measurements sensitive to the local dielectric properties from the sample.

2.3 Quantitative dielectric material properties from electrical AFM-based techniques.

One of the most important properties of an insulating material is its relative permittivity also referred to as dielectric constant, ε_r. It represents how electric dipoles in a given medium react on an external electric field and how they change their orientation and polarize according to the field. This is expressed by the equation

$$D = \varepsilon_0 \varepsilon_r E = \varepsilon_0 E + P \tag{2.23}$$

where D is the electric displacement field, ε_0 the vacuum permittivity, E the electric field and P the polarization (the second equality is valid for linear isotropic materials). It is important to notice that the dielectric constant is a material property that is related to the microscopic structure of the material under study and how fast this structure changes into its new orientation upon an applied electric field. The response time of the process is called the relaxation time. This means that the dielectric constant is time-or frequency dependent. Indeed, ε_r is a dielectric function dependent on the frequency of the applied field and can be written in the form:

$$\varepsilon(\omega) = \varepsilon'(\omega) + i\varepsilon''(\omega)\,. \tag{2.24}$$

The real part ε' is related to the stored energy in the media, while dissipation is characterized by the imaginary part ε''. The form of this dielectric function depends on which dipole in the material has to be polarized:

In *Electronic and atomic polarization* the electric field displaces the center of charge of the electrons with respect to the nucleus or opposite charged atoms in a molecule. This take place up to very high frequencies (infrared to visual

light) since the involved masses and charges lead to a very short relaxation time.

In *Ionic polarization* the dipoles formed from opposite charged ions (for example in a salt crystal) are displaced, what takes place at lower frequencies (below IR).

Orientation polarization occurs in molecules (often liquids or gases) that possess natural dipoles like for example water. The dipoles can rotate and align according to the electric field. The relaxation frequency of water is in the microwave frequency range.

Interface polarization takes place with mobile charged particles forming space charges in the bulk of a material or at the interface of different materials. (The formation of the electric double layer is for example an interface polarization). Interface polarization relaxation occurs at low frequency (mHz-MHz).

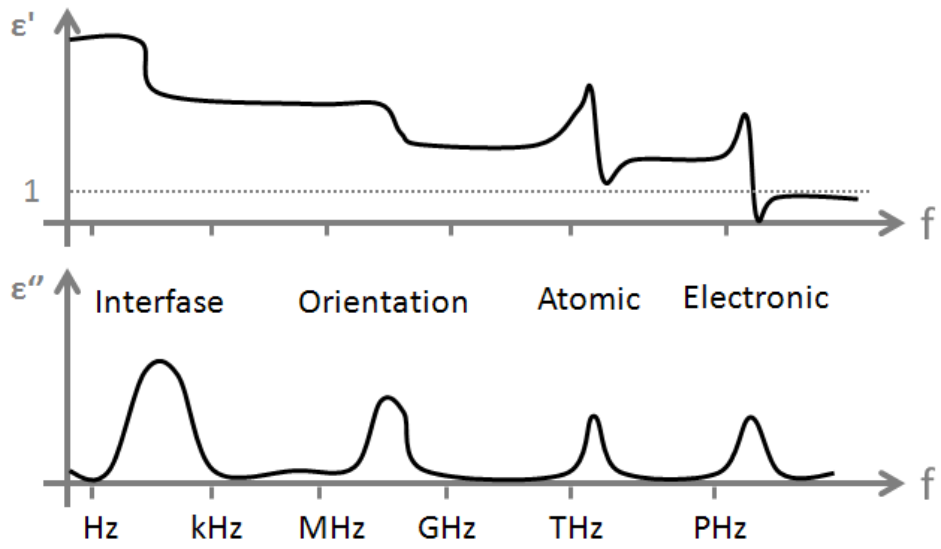

Figure 2.18 *Schematic of frequency dependency of dielectric function with underlying processes. The frequency ranges are just for orientation and may differ depending on the exact process. (Adapted from [78])*

In order to measure the dielectric constant of a material at the nanoscale one has to relate the measured current or force to the dielectric properties of the material through an appropriate theoretical model that takes into account the probe geometry and, eventually, the sample geometry.

In measurements in air environment a number of recent works have been dealing with this aspect. Again one has to distinguish between measurement of dielectric samples adsorbed on conducting substrates and samples adsorbed on thick insulating substrates.

Metallic Substrates

The electrostatic force on the AFM-tip above a bare metallic substrate has been studied extensively in the past. First simple analytical models that tried to approximate the AFM-tip as a sphere above a plane[79] where replaced by more complex models like the cone model from Hudlet et al.[80] as will be detailed also in the next chapter.

However, for the case of a thin dielectric samples supported by the metallic substrate just a few models are available. Various approaches have been made like assuming the tip-sample geometry to be a simple parallel plate capacitor with two dielectrics – one representing the air and the other the thin film. Krayev et al. [81, 82] proposed another model consisting of a spherical capacitor with two dielectrics representing the air and the thin dielectric film. The advantage of these analytical models is their simplicity. Recently our group presented another analytical approximation for thin dielectric films that is related to the Hudlet-formula[18] and will be detailed in chapter 3. Although the accuracy of this analytical approximation is good, its applicability is a bit limited to certain experimental conditions. Another completely different approach consists in performing numerical calculations and simulations to compare them with the experimental results and finally extract the dielectric constant of the sample [31, 83]. In this case, usually the tip geometry is determined in a separate calibration step and the simulation is performed with the extracted specific geometry.

Thick Dielectric Substrates

For thick dielectric substrates clearly less quantitative models are available. Actually, until now, no work has been published quantifying the dielectric constant of a thin dielectric sample on top of a thick insulating substrate.

Studies are still concentrating on the electrostatic problem of a AFM-probe above the bare dielectric substrate. Experiments showed that a simple parallel plate model which would lead to zero force for very thick substrates does not describe the physical reality. Other analytical models, like those of a sphere above an infinite dielectric[84], show at least the qualitative agreement with experimental observations and the force does not vanish for very thick substrates and tends to get independent from the thickness. However, quantitative agreement is not reached.

Again, more realistic and therefore more quantitative models could be obtained using numerical calculations using the generalized image-charge method as reported in Ref.[85] In this article the importance to include not only the apex but also the cone is emphasized, since although it is not contributing directly to the measured force, it may have an indirect effect. Another work is dealing with the indirect effect, additionally, an infinite cantilever would have for the measured force[86].

However, so far no closed methodology was reported to quantitatively extract the absolute value of the dielectric constant from thick insulators by electrostatic force or capacitance measurements. The work on the development of such a methodology is described in chapters 3 and 5.

2.4 Motivation and Objectives of this work

As shown in this chapter, AFM is an extremely versatile tool to investigate electric properties at the nanoscale and hence constitutes a good candidate technique to approach the quantification of the nanoscale dielectric properties of biomembranes. Although a few AFM techniques exist capable of investigating polarization properties, it remains difficult to extract quantitative values of ε_r from the measurements, and most importantly, they do not work in the liquid environment.

One reason for this is on the instrumental side, since for studies at the nanoscale very small quantities have to measured, that can be easily overwhelmed by electronic noise as it maybe for example the case in current sensing based techniques. Electrostatic Force sensing techniques may in principle have an advantage here, since the used cantilevers for force detection are extremely sensitive and naturally, undesired nonlocal electrical signals from the cantilever are suppressed.

Another important aspect is attributed to a lack of sufficiently precise quantitative models to relate measured force with the dielectric constant value of the sample. Indeed, for measurements on insulating substrates like mica or glass that are sometimes required for biological samples, still no quantitative model is available. Moreover, successful measurements of dielectric properties in liquid media, that is fundamental for the functionality of some biological samples, has not been shown until now.

As consequence of the existing limitations for quantitative dielectric imaging the objectives of this work were to extend the quantitative capabilities of Electrostatic Force Microscopy to image the dielectric constant of biomembranes with nanoscale spatial resolution. In particular, I addressed four objectives:

1. To evaluate the possibility to perform quantitative dielectric measurement of biomembranes on metallic substrates and in air with Electrostatic Force Microscopy that may offer higher precision with respect to current sensing techniques.

2. To extend the applicability of quantitative dielectric measurement to the case of thick insulating substrates in order to facilitate its use with biomembranes that cannot be prepared on metallic substrates.

3. To develop a setup for dielectric imaging in liquid environment based either on direct current detection or on the principles of electrostatic force microscopy.

4. To perform nanoscale dielectric measurements on biomembranes in their natural liquid environment.

3 Quantitative Electrostatic Force Microscopy

The main goal of this work and of the work of our research group is the quantitative extraction of the dielectric constant on biomembranes and other samples. As mentioned earlier, one important issue, apart from the measurement itself, is the interpretation of the obtained *dC/dz*-image or curve. This is because the *dC/dz*-signal depends apart from the dielectric constant also strongly on the probe-geometry. For this reason, using the *dC/dz*-image alone, in principle, it is just possible to make comparative measurements stating that one material has a higher dielectric constant than the other – and this only in the case that for the measurements the same unmodified AFM-tip has been used and the sample geometry is not different. Therefore, to obtain a good quantitative estimation of the absolute dielectric constant value independently of the used AFM-tip, it is necessary to apply a calibration procedure to extract first of all the effective tip-geometry to subsequently convert the *dC/dz*-image into a quantitative dielectric image.

In what follows, I will shortly review the different analytical approximations that relate the measured electrostatic force for a conductive AFM-tip above a conductive substrate with the tip geometry.

As mentioned earlier, when calculating the dielectric constant with the calibrated geometry and the *dC/dz*-image, analytical expressions are only available for a limited number of sample geometries. In the case no analytical model is available, finite element simulations can be used that are capable to calculate the electrostatic force for any geometry – although being clearly less flexible in usage. In order to cope with this drawback I developed in context with my work a number of finite element models (FEM) and scripts offering now almost the same flexibility and applicability like an analytical expression.

3.1 Analytical approximations of the probe-substrate force

Metallic substrates

To calibrate the effective electrical tip geometry with an EFM-measurement an electrostatic force versus distance curve on a flat metallic surface is acquired and compared with a theoretical prediction of this force. As explained above in section 2.2.5 the force depends apart from the applied voltage on the capacitance gradient, *dC(z)/dz*. The element that senses most of the force when approaching close to the surface, is the apex that can be modeled as a sphere with radius R_0. The force for a sphere above a metallic plane can be calculated and agrees with experimental observation for close tip sample separations ($z < R_0$)[79, 87, 88]. However, for larger distances ($z >> R_0$) the force is also influenced by the microscopic part of the tip[88, 89] that is modeled as a cone with an aperture angle of θ_0 and a height of H. The described geometry with the corresponding parameters is shown in Figure 3.1. For such a model Hudlet et al.[80] developed the approximation

$$\frac{dC(z)}{dz} = 2\pi\varepsilon_0 \left\{ \overbrace{K^2\left[\ln\left(\frac{H}{z+R_0\left(1-\sin\theta_0\right)}\right)-1+\frac{R_0\cos^2\theta_0/\sin\theta_0}{z+R_0\left(1-\sin\theta_0\right)}\right]}^{Cone} + \overbrace{\frac{R_0{}^2\left(1-\sin\theta_0\right)}{z\left(z+R_0\left(1-\sin\theta_0\right)\right)}}^{Apex} \right\} \quad (3.1)$$

$$K = 1/\ln\left[\tan\left(\theta_0/2\right)\right]$$

that relates the capacitance gradient to the tip geometry. An alternative expression for *dC*(*z*)*/dz* can be derived modeling the tip as a hyperboloid, however, this model is just exact under certain conditions and I will not

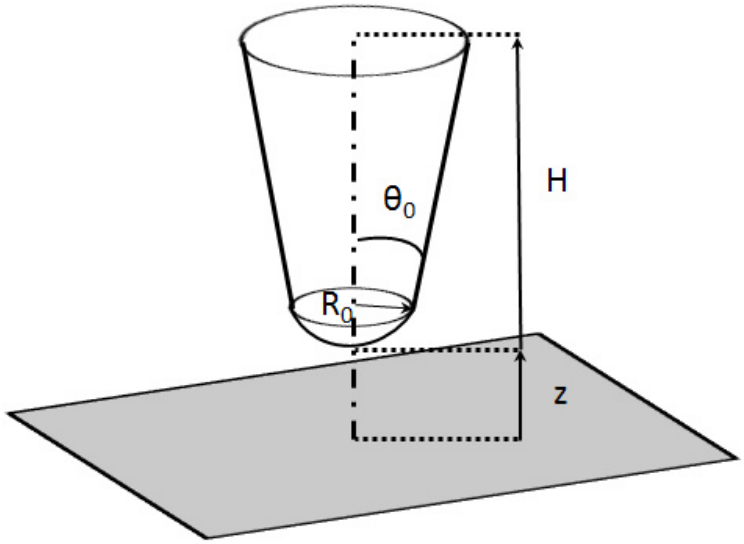

Figure 3.1 *Cone-Apex-model used by Hudlet et al. [80] to find an analytical approximation for the force on the tip above a metallic substrate.*

consider it further. The cone-apex model from Hudlet et al.[80] was experimentally revised and fits very well with experimental force-approach-curves provided the very small force contribution from the cantilever is considered[90]. The extracted tip parameters R_0, θ_0 and H are in good agreement with the physical dimensions[90].

In order to extract with the calibrated geometry the dielectric constant of an insulating thin film on the metallic substrate our group developed in recent years[17-19, 91] an approximation for the capacitance gradient contribution of the apex in dependency of the thickness, h, and dielectric constant, ε_r, of the insulator:

$$\frac{\partial C_{apex}(z,\varepsilon_r)}{\partial z} = 2\pi\varepsilon_0 \frac{R_0{}^2\left(1-\sin\theta_0\right)}{\left(z+h/\varepsilon_r-h\right)\left(z+h/\varepsilon_r-h+R_0\left(1-\sin\theta_0\right)\right)} \qquad (3.2)$$

Under the conditions that the tip radius, R_0, is bigger than the tip sample distance, z, and the dielectric film is thin (h<100nm) and not to small in

diameter ($h<<D$, $D>R_0$) equation (3.2) can be used to extract information about the dielectric constant. This is shown in detail in chapter 4 for two different types of thin film insulators. In other cases a modified version of equation (3.2) can be derived (see sections 4.7.3 – 4.7.4) or finite element simulations should be applied.

Insulating substrates

Depending on the sample under study not always metallic substrates can be used to measure the sample of interest. In these cases, nevertheless, it is possible to measure an electrostatic force. However, approximating the electrostatic forces acting on the AFM-tip above the insulating substrate is more challenging than in the case of metallic substrate and only a small number of works trying to engage this issue have been published until now [85, 86, 92]. One main difference with respect to metallic substrates is that the local electric field lines from the apex are indirectly influenced by the macroscopic parts of the AFM-tip (cone and cantilever). Chapter 5 will summarize the work to reach a methodology to quantify the local dielectric constant of thick insulating substrates that enables quantitative dielectric measurements of samples on dielectric substrates.

3.2 Finite Element Method (FEM): Introduction into electrostatic modeling with Comsol Multiphysics™

Most problems in physics that consider slightly more complex geometries have no analytical solution and approximations are only valid in very limited ranges. Therefore, one has to restore to numerical methods. This is also the case for the electrostatic problem of the AFM-tip above the dielectric sample and substrate I was dealing in my work.

The numerical method I applied in all my work is the Finite Element Method (FEM), a simulation method that is especially powerful for geometrical models involving irregular shapes and curved surfaces. It solves the partial differential equation (PDE) of interest on as many points as necessary in the defined geometry. For the electrostatic problem of the AFM-tip in air above the substrate this is the Poisson Equation. The result of this calculation is for each point of the geometry the potential, V, and the electric field, E, that can be used to calculate for example the electrostatic force on the AFM-tip. Important to mention, the points where V and E get calculated are defined in a meshing step. A particular aspect of FEM is that the shape of mesh elements is triangular (or tetrahedral in 3D) so that the specific geometry can be followed much better than with other methods.

Beside in science, applications of FEM are also found in the field of engineering where sometimes complex three-dimensional geometries are involved. FEM is a computational intensive method that requires, depending on the specific problem, beside CPU-time also big amounts of RAM (in this case at least 4 GB). To do all the simulation in the work I present here, I used the commercially available FEM-software Comsol Multiphysics™ that has a very user-friendly graphical interface to define the geometry and run the simulations, but works also with a scripting language in conjunction with Matlab™ when more specific and repetitive simulations are required.

To perform a finite element simulation of a particular problem, usually the following steps are followed:

1. The geometry is defined by drawing the sub-domains.

2. Boundary conditions are defined on the borders of the sub-domains.

3. Electric properties in the domains are defined.

4. A mesh is generated refining especially the mesh elements where the gradient of the electrical potential is high in order improve the quality of the solution.

5. The electrostatic problem is solved to obtain V and E. Usually V is plotted to see the quality of the solution.

6. The quantity of interest is calculated. For the case of the electrostatic force, the Maxwell-Stress-Tensor is integrated over the whole tip surface.

To reduce the calculation effort, it is sensible to make use of existing symmetries in the geometry that is calculated. For the model of the AFM-tip above the substrate I assumed like in the derivations of Hudlet et al.[80], that the tip is a cone and axis-symmetric with the z-axis. The simulations can be run in 2D-mode then. To give a practical idea of the simulation results I show in *Figure 3.2* a plot of the solved model (colors are the potential).
The symmetry-axis is on the left and the tip consisting of apex, cone and cantilever is located just a few nanometers above the substrate. The insets show the defined mesh (above) especially refined on the surface of the tip, a zoom onto the edges of the cantilever (middle) with rounded edges to make an accurate calculation of the electrostatic force on these boundaries possible and a zoom onto the tip-apex (bottom). Notice, to make the simulation more realistic the inner domain is enclosed by outer domains that use the infinite elements function to effectively transform the position of the outer boundaries to infinity.

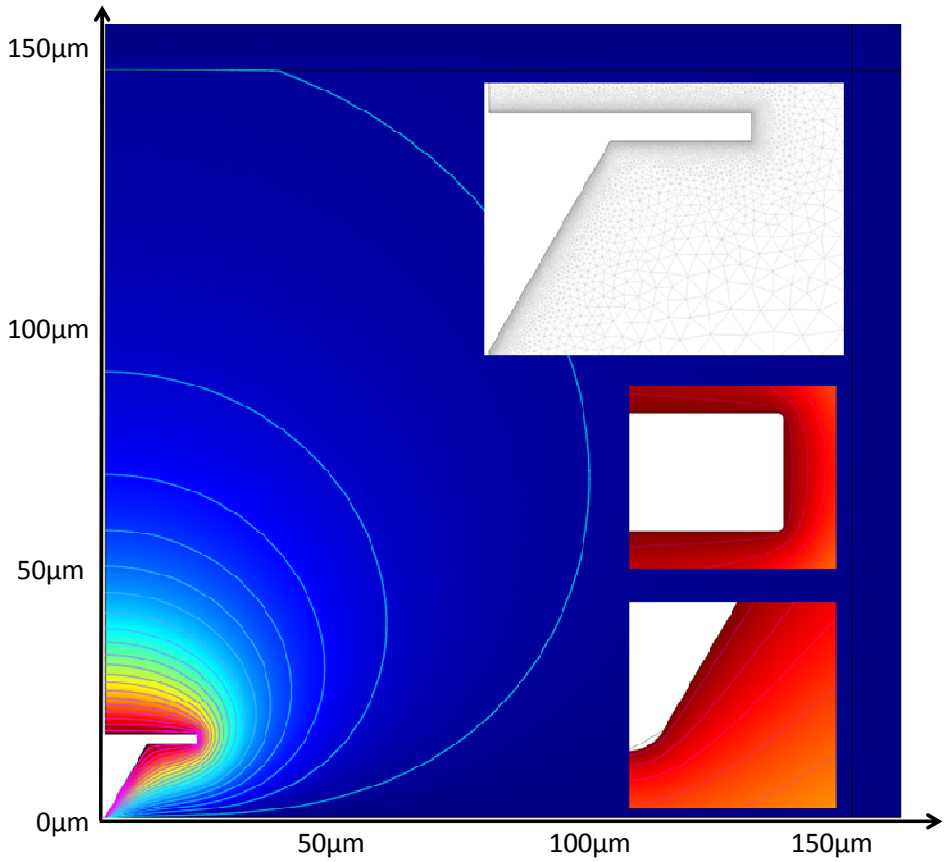

Figure 3.2 *Finite Element Model of an axis-symmetric AFM-tip above a metallic substrate. The potential is plotted in colors. In the outer sub-domains the infinite element function is active. The insets show the used mesh and a zoom onto the cantilever edge and the apex.*

Bottom boundaries are set to *ground*, boundaries on the tip are set to *port*, left side boundaries are *axis-symmetry*, top and right side boundaries are *insulating* or *zero charge*.

The size of tip domain is chosen at least 4 times bigger than the tip dimensions so that at least 90% of the applied potential has dropped off in this domain. Only then effects of the domain size in the simulated force curves are clearly below 0.1zF/nm. Nevertheless the possible domain size is limited since too big domains create too many mesh elements and also problems during the

meshing of the very small apex (degenerated triangles or cavities are generated).

The mesh-size on the tip-boundaries was set to 20 nm, except from the apex where the mesh size was set to the size of the tip radius R divided by 20. The global mesh quality was set to extra fine.

To obtain the electrostatic force o the AFM-tip the Maxwell-Stress-Tensor in z direction was integrated over the whole tip geometry following the equation:

$$F_z = \frac{1}{4}\varepsilon_0\varepsilon_r(E_r \cdot E_z \cdot n_r + \frac{1}{2}(E_z^{\,2} - E_r^{\,2}) \cdot n_z) \cdot V_{ac}^{\,2} \qquad (3.3)$$

where n represents the respective normal vector. In *Comsol-electrostatics mode* this equation reads:

*Maxwell=1/2*pi*r*((Vr*VVz*nr+0.5*(Vz^2Vr^2)*nz)*epsilon0_emes)*epsilonr_emes*

Vr=-nr(lm1)/r/(epsilon0_emes*epsilonr_emes)*
Vz=-nz(lm1)/r/(epsilon0_emes*epsilonr_emes)*

To improve accuracy the variable *lm1* defined on the boundaries and derived from the weak constraints is used to calculate the electric field *Vr* and *Vz.*

3.2.1 A ready tool for standardized electric tip calibration using finite element simulations

In order to quantify the dielectric image of the sample with EFM I used the following procedure:

1. A normal topography image is acquired in dynamic or tapping mode.
2. A *dC/dz*-image is acquired scanning the sample again a few tens of nm out of contact and at a defined constant height above the flat substrate.
3. Since the *dC/dz* signal depends not only on the sample dielectric constant, but also on the probe geometry the AFM-tip has to be calibrated by a *dC/dz*-approach curve onto the bare metallic substrate.
4. The tip geometry is calibrated in a fitting procedure as detailed below and the dielectric image is calculated with the tip geometry, the acquired topography and the *dC/dz* image.

Since the tip geometry is a very important parameter it is advisable to repeat the tip calibration from time to time.

As mentioned, in order to perform a quantitative extraction of the dielectric constant, ε_r, of a sample it is necessary to calibrate tip-geometry in a first step. In such a calibration procedure a theoretical expression is fitted to the experimental *dC(z)/dz*-curve giving the best fitting geometric parameter R_0 and θ_0 and corresponding error bounds. For the case of metallic substrates this theoretical expression can be an analytical approximation as shown in section

3.1. However, as mentioned for insulating substrates and more specific sample geometries no analytical expressions are available and the alternative approach is to use finite element simulations. Unfortunately, one of the big shortcomings of finite element simulations is that they give just the solution for one specific set of parameters (e.g. one tip geometry, one tip substrate distance z). In consequence they are not very flexible and easy to use compared with analytical expressions.

To provide, however, a methodology capable to calibrate the tip geometry for measurements on dielectric substrates my approach was to:

1. Simulate a large number tip-sample geometries covering the whole range of possible parameters (apex radius R=1-120nm, cone angle θ=5-44°, cone height H=5-20 µm, cantilever width L=0-70 µm, substrate dielectric constant ε_r=2-10). The simulations had to be very precise and fast at the same time to finish in a finite time (e.g. 1 month).

2. Generate a 5-dimensional interpolation function Force(H, L, R, Q, ε_r) as a fitting function on non-linear grid.

3. Write a script capable to perform a fitting procedure with the generated interpolation function to put out the desired parameters.

The large set of simulations was performed with Comsol™ using the scripting in Matlab™. The total number of simulations performed for one interpolation function is around 500.000.

The final calibration tool performing the interpolation and fitting is written in Mathematica™. The tool works successfully and is used by the group for the electrical tip calibration. Further details are described in chapter 5.

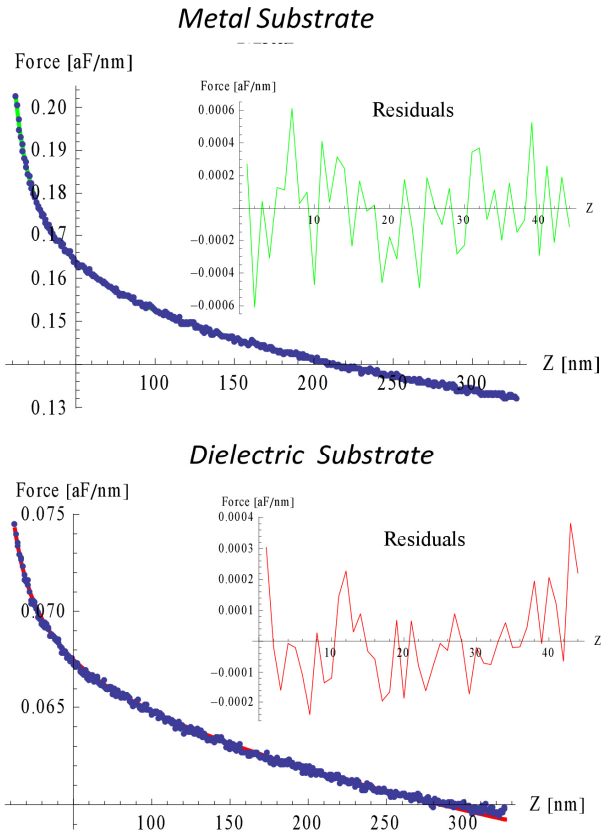

Figure 3.3 *Calibration tool to calibrate the AFM-tip geometry from EFM-measurements. The dC/dz-approach curves onto a metallic and a dielectric substrate are shown. Fit and corresponding residuals (inset) are plotted.*

4 Quantitative dielectric constant measurement of supported biomembranes by DC-EFM

4.1 Abstract

A simple method to measure the static dielectric constant of supported biomembranes with nanometric spatial resolution is presented. The dielectric constant is extracted from DC electrostatic force measurements with the use of an accurate analytical model. The method is validated here on thin silicon dioxide films (8 nm thick, dielectric constant ~ 4) and Purple Membrane monolayers (6 nm thick, dielectric constant ~2), providing results in excellent agreement with those recently obtained by nanoscale capacitance microscopy using a current-sensing approach. The main advantage of the force-detection approach resides in its simplicity and direct application on any commercial atomic force microscope with no need of additional sophisticated electronics, thus being easily available to researchers in materials science, biophysics and semiconductor technology.

This chapter reproduces almost literally the article: Quantitative dielectric constant measurement of thin films by DC electrostatic force microscopy, Nanotechnology 20, 395702 (2009) by G. Gramse, I. Casuso, J. Toset, L. Fumagalli and G. Gomila.

In this article I was in charge of performing the experiments, the theoretical modeling and processing the results. In this part of the work I followed suggestions in the experimental methodology by I. Casuso and L.Fumagalli and in the theoretical part by J. Toset and my supervisor. The article was written by me with the collaboration of my supervisor and the senior researcher L. Fumagalli.

4.2 Introduction

As we mentioned in the introduction, probing the nanoscale dielectric constant of biomembranes is fundamental in biology, because many bioelectric processes depend on the value of this property at the nanoscale [93]. Since standard characterization techniques are not capable of addressing the dielectric constant of biomembranes at this scale, new techniques are needed to achieve higher spatial resolution.

The large number of electrical scanning force microscopy (SFM) techniques applied in recent years to study electrostatic and dielectric properties of nanostructures and thin films both at low and high frequency [11, 12, 15, 17-20, 32, 38, 69, 70, 82, 83, 94-103] still present some fundamental problems. In particular, the long range nature of the electrical interaction and the complexity of the tip-sample geometry, make the accurate modelling of experimental data and hence the correct quantification of the dielectric properties rather difficult.

For thin dielectric films this difficulty has been recently overcome by the derivation of a simple analytical model that accurately quantifies the tip-thin film capacitance [18]. Applying this model to local capacitance measurements obtained with a current-sensing nanoscale capacitance microscope [15, 20] the precise quantification of the low-frequency dielectric constant of thin silicon dioxide films [17] and supported biomembranes [19] has been successfully achieved at the nanoscale. However, current-sensed dielectric microscopy on ultrathin films has the drawback of requiring an extremely sensitive instrumentation (sub-attoFarad capacitance resolution) that is usually not available with commercial SFM.

In this work we adapted the method and analytical model validated with the current-sensing approach to DC electrostatic force microscopy (DC EFM) and provide a simple measurement approach for supported biomembranes and thin dielectric films in particular, using standard SFM. We will show that, in spite of its simplicity, the DC force-detection based approach

can provide quantitative values of the static dielectric constant of supported biomembranes and thin films at the nanoscale with a performance comparable (or better) to nanoscale capacitance measurements. In particular, we will show that for ultrathin films (thickness <10 nm) and low dielectric constant materials (ε_r <10), a precision below ~5% and a spatial resolution better than ~70 nm can be easily obtained with a commercial atomic force microscope (AFM) with no need of any additional electronic instrumentation.

4.3 Theoretical model and measurement protocol

Let us consider a conductive AFM probe positioned above the dielectric film of the thickness *h* with the tip apex separated by an initial distance z_0 from the conductive substrate, as schematically shown in Figure 4.1. When a DC voltage is applied between the probe and the substrate, the cantilever deflects by an amount *D*, yielding a new equilibrium position of the apex at a distance $z = z_0 - D - h$ from the thin film. The deflection *D* depends on the spring constant *k* of the cantilever, the potential difference between tip and sample (the applied voltage *V* reduced by the surface potential V_{SP}) and the total capacitance C_T between the probe and the sample, according to the relation

$$D \equiv z_0 - h - z = -\frac{1}{2k}\frac{\partial C_T}{\partial z}\left(V - V_{SP}\right)^2 \tag{4.1}$$

The Van der Waals interaction has not been included, since it is negligible at the tip-substrate distance considered here (tens of nanometers).

The total probe-sample capacitance C_T can be modelled as the sum of two contributions, the stray capacitance C_{stray} given by the micrometric components of the probe (cone and cantilever) and the apex contribution, C_{apex}. The apex capacitance, C_{apex}, depends on the local properties of the sample and for thin dielectric films, it can be modelled using the formula already experimentally validated by nanoscale capacitance microscopy and finite-element numerical simulations [17]

$$C_{apex} = 2\pi\varepsilon_0 R \ln\left[1 + \frac{\tilde{R}}{z + h/\varepsilon_r}\right] + K(R,\theta) \tag{4.2}$$

where $\tilde{R} = R(1-\sin\theta)$, ε_0 is the vacuum permittivity, ε_r the relative dielectric constant, *h* the film thickness, *R* the apex radius, θ an angle defining the apex surface (typically the cone angle) and *K* is an irrelevant constant term depending on the tip geometry. This model is valid for smooth surfaces with topography variations with a lateral spatial variation longer than the spatial

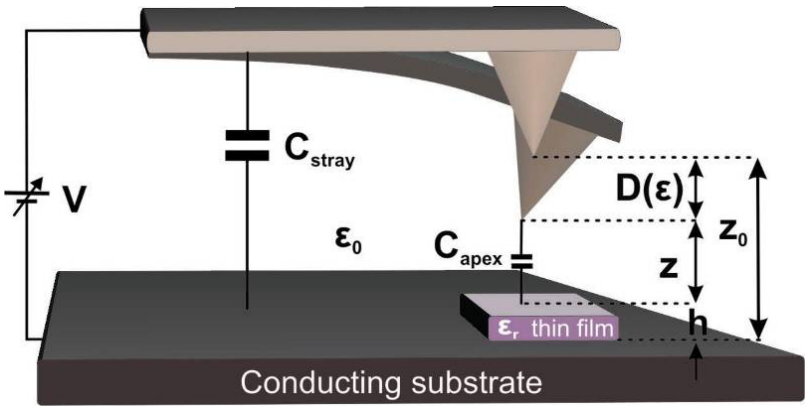

Figure 4.1 *Schematic representation of a DC electrostatic force microscopy measurement on a thin film for dielectric constant extraction. A DC voltage bias is applied between a conducting probe and substrate, resulting in a deflection D of the cantilever, which depends on the static dielectric constant of the thin film. Reprinted from Ref.* [91] *(copyright 2009 of IOP).*

resolution of the technique. In the case of rough surfaces one needs to restore to theoretical approaches including the effect of roughness (see for instance [104]).

On the other hand, the stray capacitance, C_{stray}, is independent from the local properties of the thin film, provided the film thickness is in the nanometre range [86]. In addition, for nanometric displacements around the measuring position, the stray capacitance can be assumed to vary linearly with the tip-sample distance and hence it only gives a constant deflection term, D_0 [86, 105]. For larger displacements one may need to consider an explicit z dependence of the stray contribution term [80, 90].

Substituting equation (4.2) in equation (4.1), the total DC electrostatic deflection of the cantilever over a thin dielectric film can then be expressed as

$$D = \frac{\left(V - V_{SP}\right)^2 \pi \varepsilon_0 R \tilde{R}}{k} \left[\left(z + \tilde{R} + h/\varepsilon_r \right) \left(z + h/\varepsilon_r \right) \right]^{-1} + D_0 \qquad (4.3)$$

Equation (4.3) constitutes a generalization to larger tip-sample distances of the expression proposed by Sacha *et al*.[85] In addition for metallic samples, since $h/\varepsilon_r \to 0$, equation (4.3) reduces to the well known formula by Hudlet *et al*. [80]

$$D = \frac{\left(V - V_{SP}\right)^2 \pi \varepsilon_0 R \tilde{R}}{k} \left[\left(z + \tilde{R} \right) \cdot z \right]^{-1} + D_0 \qquad (4.4)$$

Equation (4.3) can be solved to express the dielectric constant as a function of the cantilever deflection,

$$\varepsilon_r(D) = 2h \left\{ -2z - \tilde{R} + \left(\left[2z + \tilde{R} \right]^2 - 4z\left(z + \tilde{R} \right) + 4 \frac{\left(V - V_{SP}\right)^2 \pi \varepsilon_0 R \tilde{R}}{k\left(D - D_0\right)} \right)^{-\frac{1}{2}} \right\}^{-1} \qquad (4.5)$$

Note that, in order to express equation (4.5) in terms of measurable quantities, the tip - sample distance *z* should be substituted with $z_0 - D - h$.
Equation (4.5) provides a simple analytical expression that can be used to reconstruct quantitative maps of the dielectric constant from static EFM images. We will practically demonstrate this here by implementing a protocol similar to the one used in Ref. [19] for current-detected dielectric measurements.

After taking the topography of the thin film in dynamic mode to obtain its thickness *h*, the tip is retracted out-of-contact at a distance z_0 above the substrate and scanned *at constant-height* with a DC applied voltage while the cantilever deflection is recorded, as shown in Figure 4.2.

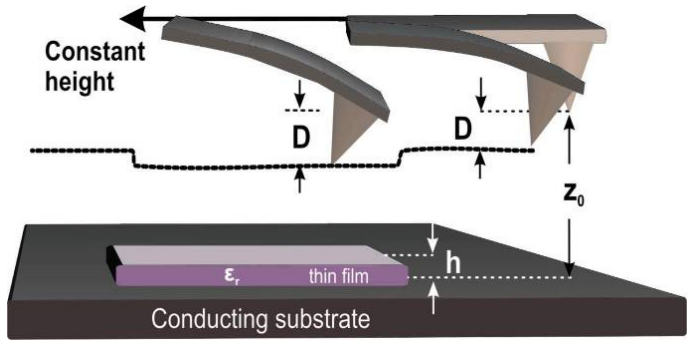

Figure 4.2 *Schematic representation of a DC EFM protocol to map the dielectric constant of thin films at the nanoscale. After acquiring the topography, the AFM tip is scanned at constant height with a DC voltage applied, while the probe deflection is recorded. From the topographic and deflection data the dielectric constant is obtained by using equation (4.5). Reprinted from Ref. [91] (copyright 2009 of IOP).*

From the thickness and deflection data, the dielectric constant is extracted point-by-point using equation (4.5). The initial distance value z_0 is obtained in a quantitative way from force curves with no potential applied measured at the beginning and at the end of each scan line. The remaining parameters appearing on the right hand side of equation (4.5), i.e. $\left(k, V_{SP}, R, \theta, D_0\right)$ are accurately calibrated as described in section 4.7.3. Note that the initial distance z_0 as well as the applied voltage V and spring constant of the cantilever k are chosen so that the probe will not collapse onto the substrate or sample during the constant-height scan (see Ref. [105]).

4.4 Validation of the method

We validate the method on two different samples, a silicon dioxide thin film and a supported biomembrane, namely Purple Membrane (PM). The $Si0_2$ thin film has been deposited on a flat gold substrate in the form of a squared pattern by using Focused Ion Beam (FIB) deposition. The $Si0_2$ square has the nominal dimensions (length x width x height) = (6 µm x 6 µm x 8 nm).

The Purple Membrane has been obtained by isolation from *Halobacterium Salinarum* following standard procedures [106]. The membrane patches with typical diameters below 1 µm and thickness around 6 nm have been adsorbed on a highly ordered pyrolytic graphite (HOPG) substrate by placing a drop of PM solution (concentration of 0.1mM in MilliQ water) under an electric field of approximately 10V/cm for ~3 min. Subsequently the sample was rinsed gently and dried under dry N_2 flow.

We used a commercial AFM (Nanotec Electrónica S.L, Spain) controlled with the WSxM software. Two types of conductive probes were employed: the Pt-Ir coated tips on the $Si0_2$ sample (*SCM-PIT-20, Nanoworld®*, nominal spring constant k = 2.8 N/m) and boron-doped diamond tips on the PM sample (*CDT-FMR, Nanosensors*, nominal spring constant k = 2.8 N/m). Spring constant of medium values were chosen as a trade-off between force sensitivity and snap-in distance under a DC applied voltage [105], as discussed in section 4.5. All the measurements reported in this session were carried out at ambient conditions with 10 V applied.

4.4.1 Nanoscale dielectric constant measurement on a thin SiO2 film

A topographic image and profile of the SiO_2 thin film, obtained with the Pt-Ir tip is shown in Figure 4.3A. The SiO_2 film shows the nominal thickness of ~8nm except at the edges where it is higher due to the deposition process. Figure 4.3B shows the corresponding deflection profile obtained by scanning the probe above the sample at an initial tip-substrate distance z_0 ~ 36nm with 10 V applied. The measured cantilever deflection profile displays a striking resemblance to the topography profile shown in Figure 4.3A, indicating both the sensitivity and locality of force-detected dielectric measurements.

Figure 4.3C shows the dielectric constant calculated using equation (4.5) from the profiles given in Figure 4.3A and Figure 4.3B on the central points of the scan line where the dielectric film is ~8nm thick. The calibrated parameters used in the calculation are: $V_{SP,substrate}$= 0.04V, $V_{SP,sample}$= 0.15V, R = 87nm, k = 2.5N/m and $D_{0,Si02}$ ~ –3.7 nm (see section 4.7.1 for calibration details).

The obtained dielectric constant values display the statistical distribution shown in the histogram in figure 3D with a mean value of $\varepsilon_{r,Si02}$=4.0 ± 0.9 and the error corresponding to one standard deviation.

It is worth remarking that the uncertainty in the dielectric constant σ_ε~ 0.9 is consistent with the noise present in the deflection detection system (σ_Δ ~ 0.1 nm) as computed from the relationship $\sigma_\varepsilon \sim \frac{\partial \varepsilon}{\partial D}\,\sigma_\Delta$ (see section 4.7.2 for statistical details). This indicates that the main source of uncertainty in the present measurements comes from the deflection detector noise. The obtained dielectric constant is well in agreement with values reported in the literature for bulk samples (fused silica ε_r = 3.8) [107] and for similar thin SiO_2 films measured at the nanoscale by nanoscale capacitance microscopy (ε_r ~ 4) [17].

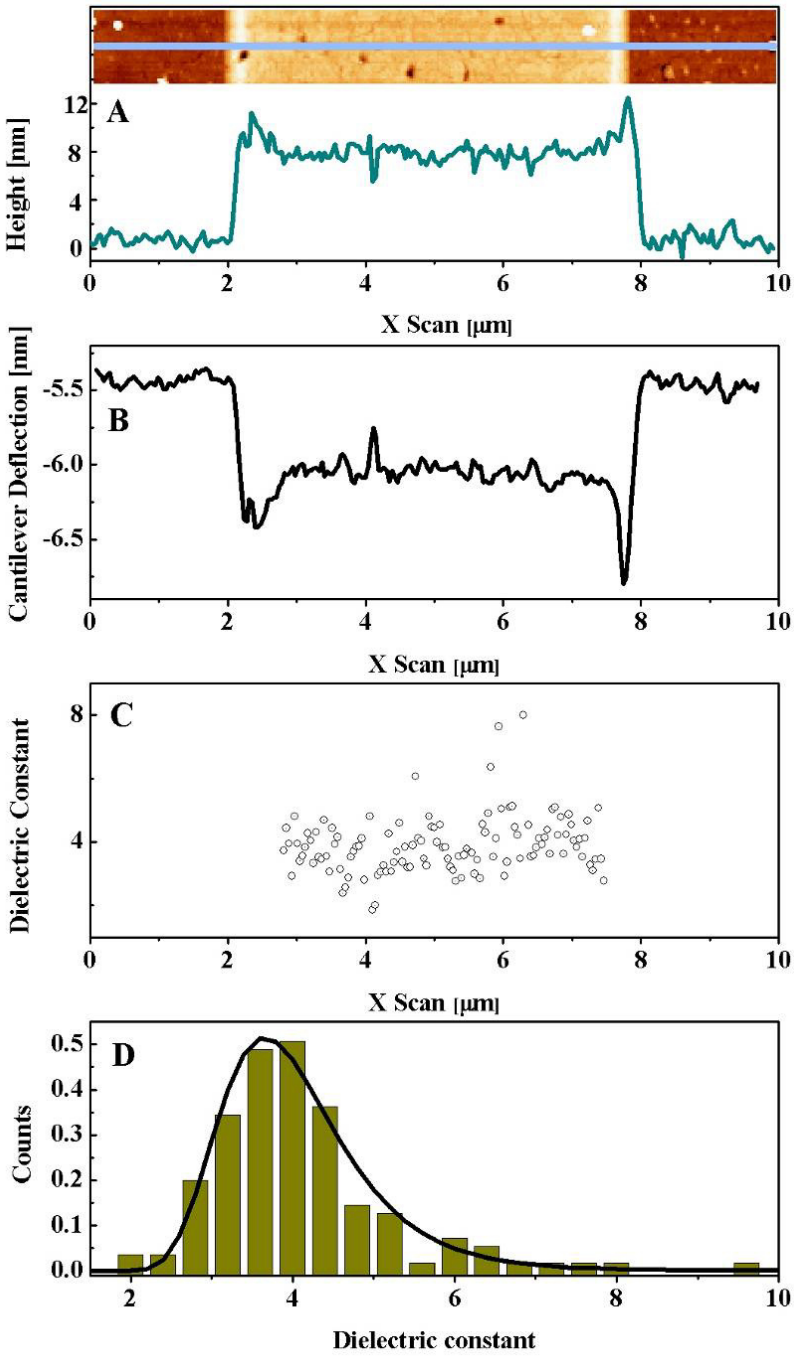
A
Height [nm]
12
8
4
0
0
2
4
6
8
10
X Scan [μm]
B
Cantilever Deflection [nm]
-5.5
-6.0
-6.5
X Scan [μm]
C
Dielectric Constant
8
4
X Scan [μm]
D
Counts
0.5
0.4
0.3
0.2
0.1
0.0
Dielectric constant

Figure 4.3 *Nanoscale dielectric constant extraction for a ~8 nm thin SiO_2 film on gold. The topography (A), cantilever deflection (B), extracted dielectric constant (C) and statistical distribution of the dielectric constant (D) are plotted. A least square fit of the statistical distribution is plotted as a solid line in (D) from where a value $\varepsilon_{r,SiO2} = 4.0 \pm 0.9$ is obtained (Calibrated parameters: initial scan height z_0=36 nm, applied voltage V=10 V, spring constant k=2.5 N/m, stray deflection $D_{0,SiO2} \sim -3.7$ nm and apex radius R=87nm). Reprinted from Ref. [91] (copyright 2009 of IOP).*

4.4.2 Nanoscale dielectric constant measurement of Purple Membrane

The topographic image of a Purple Membrane patch on a HOPG substrate obtained with a diamond tip is shown in Figure 4.4A. The lateral dimensions of the patch are around 500 nm x 1 μm with a thickness of around 6 nm. The two protrusions that reach 12nm height are small adsorbed membrane pieces.

The electrostatic deflection image is shown in Figure 4.4B together with a histogram of measured deflection values (left inset) and a representation of the measured initial distance values for each scan line (right inset). The deflection image of the membrane patch shows again a striking resemblance to the topographic image, thus constituting a good indication of the locality of the measurement. The only appreciable difference can be seen on a band of lines below the middle part of the image that correspond to a number of scan lines that were unintentionally taken at a significantly higher scan height, as revealed by the right inset in Figure 4.4B. This fact introduces three levels of deflection on the membrane patch, namely, ~ 5.7 nm (green) corresponding to the flat parts of the membrane ~ 6.1 nm (blue) corresponding to the region with the protrusions and ~ 5.3 nm (red) for the scan lines taken at a higher height (the substrate deflection is ~ 5.0 nm (orange)).

Figure 4.4C displays the reconstructed dielectric constant image together with the histogram of values on selected areas (inset). The image values have been computed by using equation (4.5) with the deflection and topography image given in Figures 4.4A and 4.4B, including the initial distance values shown on the right inset of Figure 4.4B. The calibrated parameters used in the calculation are in this case: k = 3 N/m, R = 167 nm, $V_{SP,substrate}$=0.01V, $V_{SP,PM}$=0.11V and $D_{0,PM}$ ~ –0.5 nm (see Appendix 1). The values of the dielectric constant obtained on a flat region of the membrane (squared area I in figure 4.4C) follow the statistical distribution shown in the inset of Figure 4.4C, with mean $\varepsilon_{r,I}$=1.78 ± 0.07. This value is in good agreement with the value recently obtained on a similar sample by means of nanoscale capacitance microscopy (ε_r= 1.9 ± 0.1) [19]. Again, the standard deviation of the dielectric constant (σ_ε~0.07) is consistent with the deflection detection noise (σ_D~0.06 nm) displayed by the measuring system. This shows that even when different scan lines are involved in the calculations, the main source of noise continues to be the deflection detection noise.

It is worth remarking that the obtained dielectric constant value is insensitive to the scan height provided its value is recorded precisely as we did here, thus showing the robustness of the present method. This can be observed by the fact that the dielectric constant value extracted in the area II in Figure 4C scanned at a different scan height, $\varepsilon_{r,II}$=1.82±0.06, agrees with the value extracted in area I, $\varepsilon_{r,I}$=1.78±0.07.

Figure 4.4 *Nanoscale dielectric constant measurement on a Purple Membrane patch. The topography (A), the cantilever deflection (B) and the extracted dielectric constant (C) are displayed. In the right inset in B the simultaneously acquired lift height is plotted for each line. Histograms in the inset of B and C show the distribution of the cantilever deflection and the dielectric constant on the purple membrane, respectively. (Calibrated parameters: applied voltage V=10V, spring constant k=3.0 N/m, stray deflection $D_{0,PM}$ ~ –0.5 nm and apex radius R=167nm). Reprinted from Ref. [91] (copyright 2009 of IOP).*

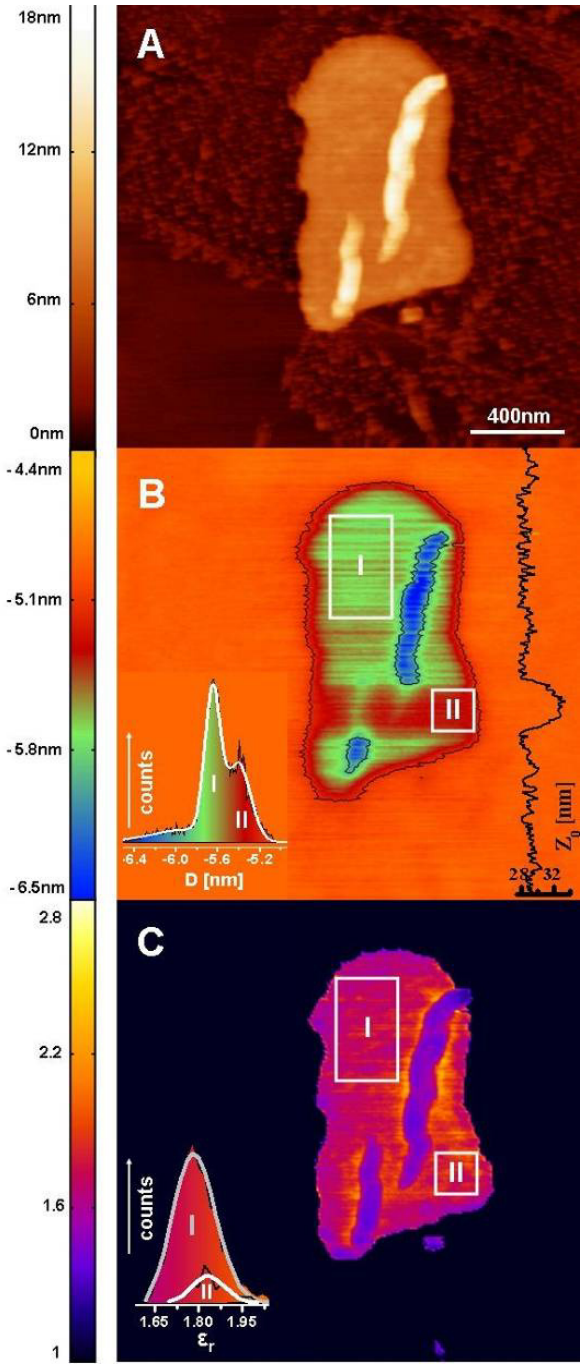
18nm
12nm
6nm
0nm
-4.4nm
-5.1nm
-5.8nm
-6.5nm
2.8
2.2
1.6
1
A
400nm
B
I
II
counts
-6.4 -6.0 -5.6 -5.2
D [nm]
Z_0 [nm]
28 32
C
I
II
counts
1.65 1.80 1.95
ε_r

Finally, we note that the dielectric constant obtained at the edges or on the nanometric protrusions of the membrane is slightly smaller (ε_r ~1.5) and exceeds the experimental error obtained on the flat regions. This is probably due to the fact that the model is only valid on flat thin films larger than the spatial resolution of the technique, whereas the size of the protrusions is at or below the resolution limit. In the present case the lateral resolution can be estimated to be ~80 nm, defined as half the distance needed for the deflection to pass from the average value on the bare substrate to that on the flat membrane region (data not shown). This value is in good agreement with the theoretical lateral resolution of the technique [108] ~ $\sqrt{Rz_0} \approx 70nm$.

4.5 Discussion

In the previous section we have shown the ability of DC EFM to quantify the static dielectric constant of two different thin films at the nanoscale. Here we will analyze the factors that determine the uncertainty of the extracted values and establish the best application range of the technique.

According to the results reported in Section 4.4 the uncertainty of the dielectric constant value, represented by the standard deviation of values, σ_ε, is mainly determined by the deflection detection noise of the AFM system, σ_D, through the relationship $\sigma_\varepsilon \sim \frac{\partial \varepsilon}{\partial D}\,\sigma_D$. Several parameters appear in this equation, which can play a role in the final standard deviation of dielectric constant σ_ε. In order to illustrate the most relevant factors, we will consider the case of the measurement performed on the Purple Membrane patch. By taking as initial parameters those of the experiment, namely, k=3 N/m, V=10 V, ε_r=2, z_0=30 nm, h=6 nm, R=167 nm, we will analyze how the uncertainty of the measurement evolves when varying each of them individually, while keeping the others fixed. In each case, three levels of deflection detection noise will be considered, namely, σ_D = 0.06 nm, 0.03 nm and 0.01 nm, corresponding, respectively, to the noise of our setup, of a state-of-the-art commercial AFM and to further optimized AFM for static measurements.

Figure 4.5 shows the predicted variation for the relative error in the dielectric constant as a function of (a) initial scan height, (b) applied voltage, (c) spring constant, (d) apex radius (lateral resolution), (e) relative dielectric constant of the material and (f) film thickness. In each case the parameters are varied in a range satisfying the condition that the tip does not collapse onto the sample. Figure 4.5 reveals a rather different impact of each parameter on the uncertainty of the measurement.

Explicitly, for the present case, the relative error depends in each case roughly as: $\sim z_0^{\beta}$ (β=1-2), $\sim V^{-2}$, $\sim k^{1}$, $\sim R^{-\alpha}$ (α=1-2), $\sim \varepsilon_r^{1}$, $\sim h^{-\gamma}$ (γ=1-2).
According to these results, for a given instrumental detection noise, the

precision of the measurement can be greatly increased by reducing the scan height and spring constant, and by increasing the applied voltage, as expected.

However, the condition that the probe does not collapse onto the sample or substrate imposes a trade-off between these parameters. Since the collapse distance does not depend on the spring constant of the cantilever but on the voltage at which the electrostatic collapse occurs [105], it turns out that intermediate spring constant cantilevers (k~1-10 N/m) are expected to provide the best results, since softer cantilevers would not allow applying large enough voltages, while stiffer cantilevers would produce deflection values below the deflection noise of the instrument.

On the other hand, by increasing the spatial resolution (decrease in the apex radius) a large increase in the uncertainty of the measurement is observed. This means that also here a trade-off should be made between spatial resolution (apex radius) and dielectric constant precision.

Concerning the parameters of the thin film, ε_r and h, the relative error increases linearly with ε_r and decreases slightly faster with h. This means that in principle increasing the sample thickness could constitute a good strategy to increase the precision of the measurement. However, this is not the case in practice since only slight variations of this parameter are allowed without the need to increase the scanning height, which will result in an overall decrease of precision.

Therefore, the best results will be obtained in the ultrathin limit (<10 nm), with a precision still acceptable in the molecularly thin (<2 nm) or thicker limits (>10 nm). In all the cases, since the uncertainty increases linearly with the dielectric constant of the material, measurements will be significantly more precise on low dielectric constant materials (ε_r<10) than in higher dielectric constant materials. The increase in the uncertainty with increasing dielectric constant value is a consequence of the fact that the measurement is not performed in contact with the sample. In this condition the applied potential partitions between the air gap and the thin film in such a way that the interaction between probe and thin film gets remarkably less sensitive to the dielectric constant of the material than expected from contact measurements.

According to the above discussion, the present technique is expected to be

best suited for ultrathin films (h<10 nm) and low dielectric constant materials (ε_r<10). For these thin films, if an appropriate trade-off between the different parameters and measuring conditions is achieved, dielectric constant values with relative errors well below ~5% and a spatial resolution below ~70 nm can be obtained with a commercial AFM system.

Higher spatial resolution can be achieved at the cost of precision, unless the deflection detection noise of the system is reduced. To this end, besides instrumental optimization, one can reduce the experimental noise by increasing the measurement time and averaging a number of identical measurements. Further improvements can only be achieved by moving to a more sensitive detection scheme such as alternating applied voltage EFM (AC-EFM), which however requires additional instrumentation (i.e. lock-in amplifier) not always available with standard AFM.

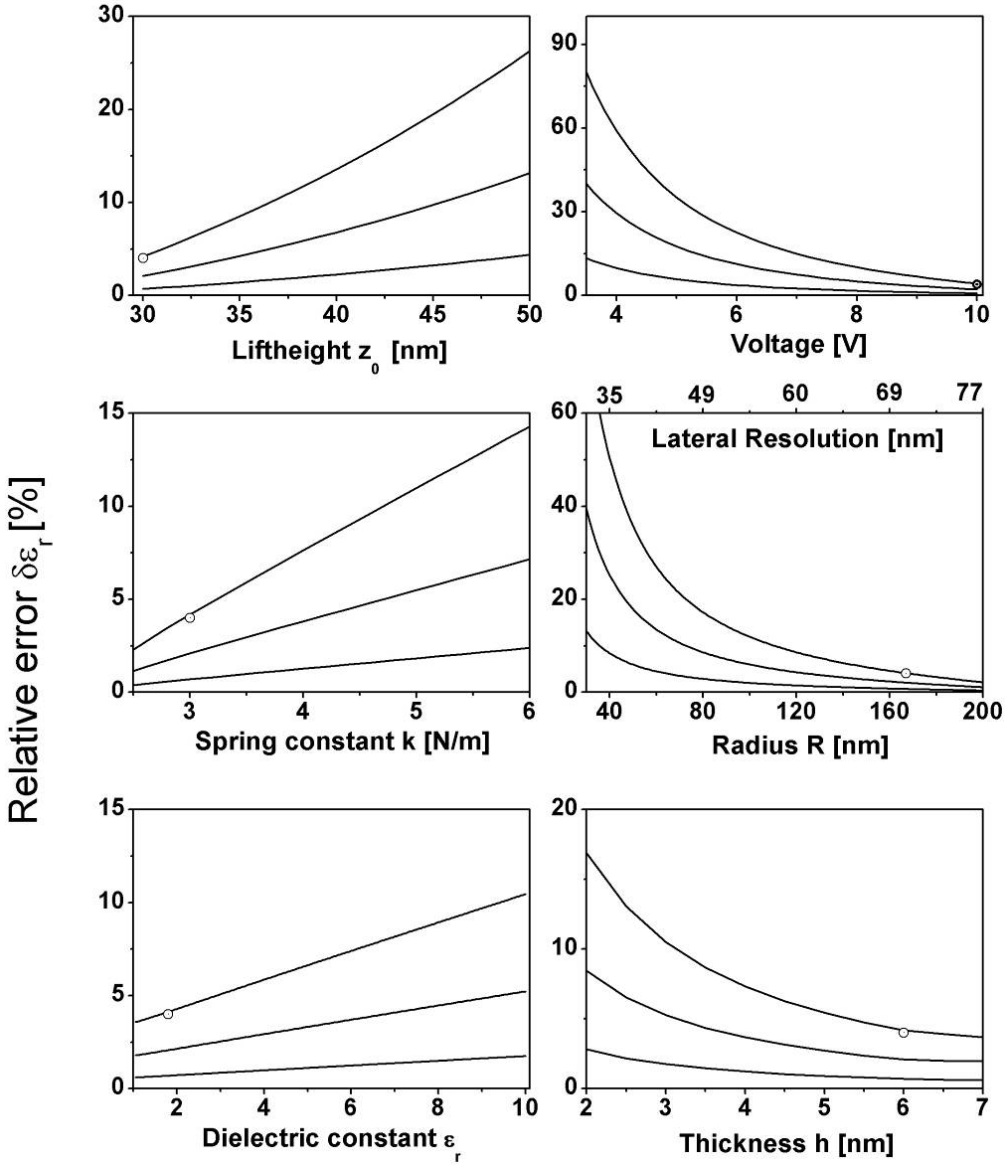
Relative error δε_r [%]
Liftheight z_0 [nm]
Voltage [V]
Spring constant k [N/m]
Lateral Resolution [nm]
Radius R [nm]
Dielectric constant ε_r
Thickness h [nm]

Figure 4.5 *Relative error of ε_r as a function of (a) initial scan height, (b) voltage applied, (c) spring constant, (d) apex radius (lateral resolution), (e) relative dielectric constant of the material and (f) film thickness. In each figure three levels of noise are considered (from top to bottom): σ_D=0.06 nm, 0.03 nm and 0.01 nm. The remaining parameters are k=3 N/m, V=10 V, ε_r=2, z_0=30 nm, h=6 nm, R=166 nm, θ=30°, D_0=0.5nm and V_{SP}=0.1V. In each figure the symbol corresponds to the experimental conditions of the purple membrane experiments reported here. Reprinted from Ref.* [91] *(copyright 2009 of IOP).*

4.6 Conclusion

In this chapter we have demonstrated a simple methodology based on DC electrostatic force microscopy to obtain quantitative values of the static dielectric constant of supported biomembranes and thin insulating films at the nanoscale. we have shown that, in spite of its simplicity, the proposed methodology implemented on a conventional AFM system can provide dielectric constant values with relative errors below a 5% and spatial resolutions below ~70 nm for ultrathin (thickness <10 nm) and low dielectric constant materials (relative dielectric constant < 10) materials. The technique has been validated on a ~8 nm thin SiO_2 film and on a ~6 nm thin biological membrane, with results in excellent agreement with dielectric constant values found in the literature for bulk samples or obtained with the current-sensing based nanoscale dielectric microscopy, recently reported. This method constitutes a very simple approach to the measurement of nanoscale dielectric constant on thin films as it can be implemented on virtually any commercially available AFM with no need of additional electronics or complex numerical simulations, thus making this technique easily accessible to researches in material science, semiconductor technology and biophysics.

4.7 Appendix

4.7.1 Parameter calibration

In order to obtain quantitative values for the dielectric constant from equation (4.5), precise calibration of the parameters appearing in this equation is essential.

The spring constant of the cantilever, k, has been calibrated here by analysing the thermal oscillation of the cantilever as described in Ref. [109]. We have obtained the values k_{PtIr}= 2.5 ± 0.1 N/m and $k_{diamond}$= 3.0 ± 0.1 N/m for the Pt-Ir and diamond tips, respectively.

The surface potential, V_{SP}, was estimated by acquiring the DC deflection while sweeping the voltage between -3V and 3V on the bare substrate as well as on the dielectric sample at different tip-sample separations (for details see Ref.[110]). Fitting the deflection curve to a parabolic function of the voltage, the following surface potentials where obtained: $V_{SP,PtIr\text{-}Au}$= 0.04 ± 0.02V, $V_{SP,PtIr\text{-}SiO2}$= 0.15±0.02 V, $V_{SP,diamond\text{-}HOPG}$= 0.01 ± 0.02 V, $V_{SP,diamond\text{-}PM}$=0.11 ± 0.03 V.

The probe radius, R, was calibrated by measuring a deflection distance curve on the conducting substrate with a DC voltage applied and fitting it to equation (4.4), valid for metallic samples, with the apex radius R and stray deflection D_0 as free parameters (for the extraction of the radius the mean spring constant values have been used, i.e. k_{PtIr}=2.5 and $k_{diamond}$=3.0, while in order to reduce the number of parameters in the fitting process, θ was set to 30°).

Following this procedure we obtained the values R_{PtIr}= 87±1 nm, $D_{0,PtIr}$=–4.0 ± 0.1 nm and $R_{diamond}$= 167±1 nm, $D_{0,diamond}$= − 0.17±0.01 nm. The goodness of the procedure is shown in Figure 4.6, showing residuals with an almost uniform distribution (standard deviations 0.11 nm and 0.05 nm for the PtIr and diamond probes, respectively). Note that the larger deflections on the

PtIr probes are due to the larger voltage applied (10 V) as compared to the voltage

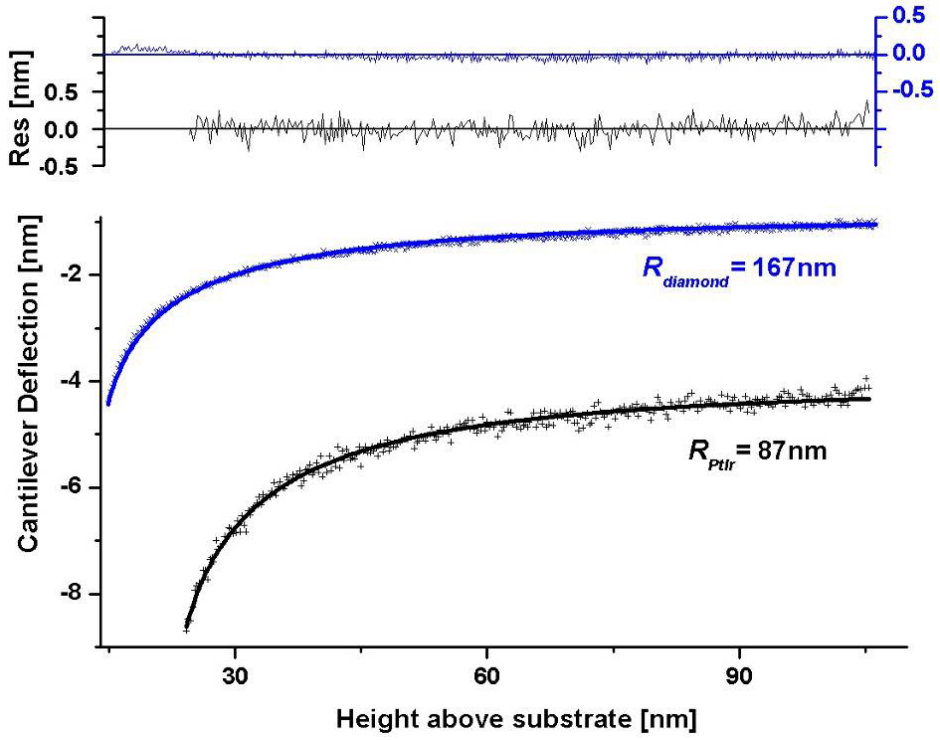

Figure 4.6 *Cantilever deflection as a function of tip-substrate distance taken on the conducting substrate with a DC voltage applied used for tip radius calibration. The Pt-Ir probe curve (black symbols) is obtained with V=5V, the diamond probe curve (blue symbols) with V = 10V. Solid lines are the least square fitting of the experimental data to equation (4.4) and fit residuals are plotted on top, showing standard deviation of ~0.11nm and ~0.06nm respectively. The obtained radius are R_{PtIr}= 87 ± 1 nm and $R_{diamond}$= 166 ± 1 nm. Reprinted from Ref.* [91] *(copyright 2009 of IOP).*

applied when using the diamond probe (5 V). Note also that for the PtIr probe the extracted radius is appreciably bigger than the nominal value. This difference can be explained by two effects that add up for this type of probes, namely, (i) the Pt-Ir probes can get blunt very easily, thus displaying usually a bigger apex radius and (ii) for small radii the use of a constant stray contribution term in equation (4.4) is less accurate thus giving rise to slightly larger apex radius values. These two facts are not relevant for the diamond probes and do not affect the extraction of the dielectric constant, as we have shown.

Finally the stray deflection contribution, D_0, has been quantified using equation (4.4) for metallic samples from the deflection measured on the conductive substrate during the scan line taken at constant-height. To reduce the uncertainty on this parameter several deflection data obtained on the flat substrate have been averaged out. The values obtained are then $D_{0,Si02} \sim -3.7$ nm and $D_{0,PM} \sim -0.5$ nm.

4.7.2 Statistical analysis of the data

The measured deflection values display a statistical dispersion due to the detection system noise that follows the Gaussian distribution

$$\mathrm{p(D)} = \frac{1}{\sigma_D \sqrt{2\pi}} \exp\left(-\frac{(D-\mu_D)^2}{2\sigma_D^{\,2}} \right) \tag{4.6}$$

where μ_D and σ_D represent the mean and standard deviation of the distribution, respectively. Accordingly, the dielectric constant values obtained from the deflection through the function $\varepsilon_r(D)$ given in equation (4.5) are also statistically distributed and follow the distribution

$$p(\varepsilon_r) = p(D) \cdot \left| \frac{\partial D(\varepsilon_r)}{\partial \varepsilon_r} \right| \tag{4.7}$$

which in general is non-Gaussian. The mean and standard deviation values of the dielectric constant are then given by

$$\overline{\varepsilon}_r = \int \varepsilon_r \, p(\varepsilon_r) d\varepsilon_r; \quad \sigma_\varepsilon = \sqrt{\int (\varepsilon_r - \overline{\varepsilon}_r)^2 \, p(\varepsilon_r) d\varepsilon_r} \tag{4.8}$$

In this paper we firstly obtained the distribution by fitting the histogram of measured dielectric constant to equation (4.7) with μ_D and σ_D as free parameters and then calculated the mean and standard deviation using equations (4.8). For the results reported here, it can be shown that these values can be equivalently obtained using the approximated relation of the non-Gaussian distribution of dielectric constant to the first order in the deflection noise

$$\overline{\varepsilon}_r \sim \varepsilon_r(\mu_D) + \frac{1}{2}\frac{\partial^2 \varepsilon_r(\mu_D)}{\partial D^2}\sigma_D^2 \tag{4.9}$$

and

$$\sigma_\varepsilon \sim \left|\frac{\partial \varepsilon_r(\mu_D)}{\partial D}\right| \sigma_D \tag{4.10}$$

This justifies the use of equation (4.10) in the precision analysis given in Section 4.4.

4.7.3 Analytical formula for the electrostatic force on small AFM-tips including the cone contribution

As we mentioned in section 2.3, the formula relating the dielectric constant with the capacitance gradient and consequently with the measured electrostatic force is just valid under a limited number of conditions. Especially for tips with smaller apex radii than the ones we used in this chapter, I showed that the use of equation (3.2) can yield incorrect dielectric constant values. This is because for small tips (R<50-100nm) not only the apex but also the cone is contributing to the measured force-difference. I found that under these conditions instead the following analytical equation can be used to extract the correct dielectric constant from the measured capacitance gradient difference, ΔC':

$$\Delta C' = C'_{sample}(z)' - C'_{metal}(z), \tag{4.11}$$

where the sample capacitance gradient is:

$$C'_{sample}(z) = 2\pi\varepsilon_0 \left\{ \overbrace{K^2 \left[\ln\left(\frac{H}{z + h/\varepsilon_r - h + R_0(1-\sin\theta_0)} \right) - 1 + \frac{R_0 \cos^2\theta_0 / \sin\theta_0}{z + h/\varepsilon_r - h + R_0(1-\sin\theta_0)} \right]}^{Cone} + \overbrace{\frac{R_0^{\,2}(1-\sin\theta_0)}{(z + h/\varepsilon_r - h)(z + h/\varepsilon_r - h + R_0(1-\sin\theta_0))}}^{Apex} \right\} \tag{4.12}$$

$$K = 1 \Big/ \ln\left[\tan\frac{\theta_0}{2} \right]$$

In order to obtain the metal capacitance gradient, $C'_{metal,}$ the dielectric constant in this equation is simply set to the value $\varepsilon_r = 1$.

To show the good agreement of equation (4.12) with numerical calculations, I compare in Figure 4.7 the force difference between the bare metallic substrate and a membrane of the dimensions 5nm x 1000nm and dielectric constant ε_r=3 (black, line) that I calculated with the finite element method and the force difference calculated using the proposed equation (4.12) (red line) and equation (3.2) (blue line) that has been used by us earlier.

The comparison is shown for a tip of small apex radius *R=20 nm*, a big apex radius R=100 and in both cases a cone angle of θ*=30°.* As can be seen, the new equation reproduces the finite element simulations much better than the older one. Especially at close distance, where measurements are usually carried out, the equation (4.12) agrees almost perfectly with the simulations what demonstrates the good quality of this approximation. However, for big tip radii the difference between both models is very small and the in this chapter applied equation 3.2 gives also correct results.

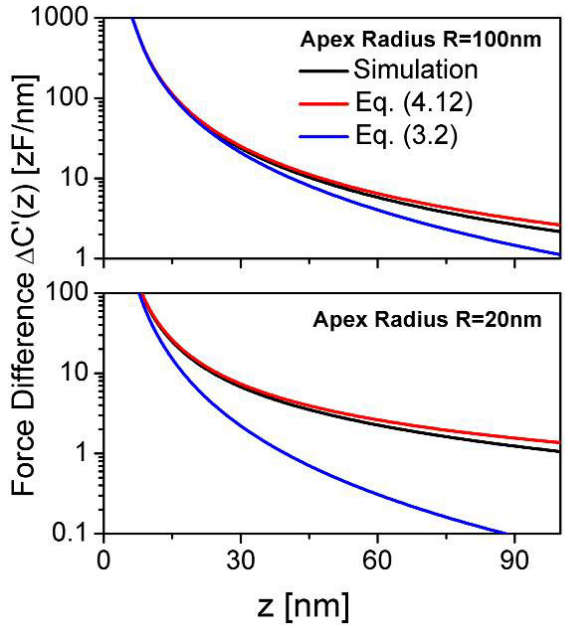

Figure 4.7 *Capacitance gradient differences between metallic substrate and membrane of 5nm in height, 1000 nm in diameter and dielectric constant of ε_r=3. The differences are plotted for varying tip substrate distances. Geometric tip parameters are R=20nm, R=100nm, θ=30°, H=15 µm. Simulations are compared with equation 4.12 and 3.2, respectively. Note, the log scale on the y-axis.*

5 Quantifying the dielectric constant of thick insulators using EFM

5.1 Abstract

This chapter deals with extending the methodology developed in the previous chapter to the case in which thick insulating substrates, instead of metallic substrates, are considered. As I have mentioned, the use of insulating substrates such as glass or mica turns out to be very advantageous when dealing with supported biomembranes. Here we present a systematic analysis of the effects that the microscopic parts of electrostatic force microscopy probes (cone and cantilever) have on the electrostatic interaction between the tip apex and thick insulating substrates (thickness > 100μm). We discuss how these effects can influence the measurement and quantification of the local dielectric constant on thick insulating substrates. We propose and experimentally validate a general methodology that takes into account the influence of the cone and the cantilever, thus enabling to obtain very accurate values of the dielectric constants on thick insulators. Finally, the locality of the technique is discussed.

This chapter reproduces almost literally the article: "Quantifying the dielectric constant of thick insulators by electrostatic force microscopy: Effects of the microscopic parts of the probe", Nanotechnology 23, 205703, 2012 by G. Gramse, G. Gomila and L. Fumagalli and it includes also a part of the article "Quantifying the dielectric constant of thick insulators using electrostatic force microscopy", Applied Physics Letters 96, 183107, 2010, by L. Fumagalli, G. Gramse, D. Esteban-Ferrer, M. A. Edwards, and G. Gomila. In these two articles I was in charge of performing the theoretical modeling. In this part of the work I followed suggestions in the modeling methodology by M. A. Edwards. The experimental data was acquired and processed by L. Fumagalli. This part of the work was supervised jointly by the senior researcher L. Fumagalli and my supervisor. The first article and the part of the second article reproduced here was written in both cases by me, in collaboration with my supervisor and the senior researcher L. Fumagalli.

5.2 Introduction

Measurement and quantification of the dielectric constant, ε_r, at the nanoscale has been demonstrated using scanning force microscopy based on capacitance[17, 19] and electrostatic force [82, 83, 91, 102, 111, 112] detection for the case of thin insulating films (thickness < 1µm), with examples ranging from thin oxide films and polymer blends to supported biomembranes. On *thick* insulators (thickness > 10µm), on the other hand, quantifying ε_r is much more difficult, not only because the signal-to-noise ratio is smaller, but also because the data interpretation sensitively depends on the modeling of the probe. This is due to the fact that the geometry of the microscopic parts of the probe, that is, the cone and the cantilever, can *indirectly* influence the local electrostatic interaction between the tip apex and the thick dielectrics, as suggested by some theoretical works [85, 86, 113, 114]. However, the ability to quantify the dielectric constants on thick insulators would open new possibilities, such as the study of interfacial effects of insulators [115] and thick nanocomposite insulators [116]. Particularly, it would enable the electrical/dielectric characterization of molecules and nano-objects (single biomolecules[117], self-assembled monolayers[38, 118], liquid layers[38], nanotubes [119], nanoparticles[120]) directly on millimeter-scale insulating substrates like mica or glass cover slips, thus avoiding the difficulties in preparation on conductive substrates.

Here, we systematically analyze from a theoretical point of view the influence of the cone height and the cantilever area on the local electrostatic interaction between the tip apex and thick dielectric substrates and hence on the quantification of the local dielectric constant. Based on these results, we propose and experimentally validate a general methodology to properly account for these effects. We show that adding a disc that simulates the cantilever further improves the accuracy of the obtained dielectric constants.

The final result is a very accurate and systematic methodology to extract the dielectric constant of the nanometric volume at the surface of a thick insulating material. This methodology is also readily applicable to quantitative measurements on bio-membranes.

The chapter is organized as follows. In section 5.3 we describe the probe-thick insulator system and the numerical approach used to solve the corresponding electrostatic problem. In section 5.4 we analyze how the cone and the cantilever affect the tip-substrate electrostatic interaction. In section 5.5 we investigate their influence on the obtained dielectric constant from EFM measurements and propose a general methodology to extract the dielectric constants on thick insulators, taking into account the microscopic effects of the cone and cantilever. In section 5.6 we address the locality of the technique. Finally in section 5.7 we summarize the main conclusions of this chapter.

5.3 Theoretic Modeling

To analyze the effect of the microscopic parts of the EFM probe (the cone and the cantilever) on the tip apex – thick insulator interaction, we considered the simplified model given in Figure 5.1. The probe consists of a truncated cone of height H and cone aperture angle θ ended with a semi-spherical apex of radius R. In addition, a disc of radius and thickness w is located on top of the cone, where L is the part of disc radius not covered by the cone base. Here, for simplicity, we will refer to L as to the cantilever disc radius. The tip apex is positioned at a distance z from the thick insulator substrate of dielectric constant ε_r. we assume that the insulating substrate has infinite lateral and

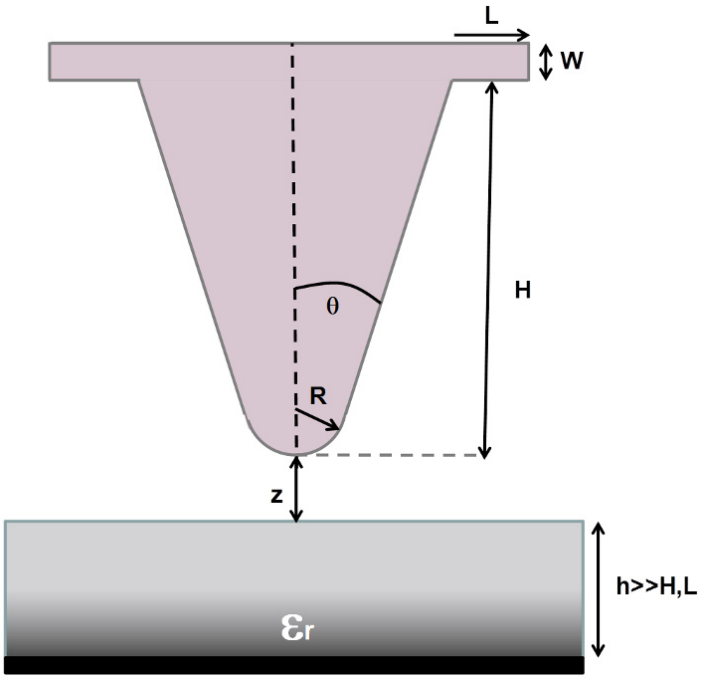

Figure 5.1 *Schematic representation of the probe-thick insulator system modeled with 2D finite-element numerical calculations. A disc over the cone is used to model the cantilever effects. The scheme is not to scale. Reprinted from Ref.* [121] *(copyright 2012 of IOP).*

vertical size, since the width is much larger than any microscopic part of the probe and the thickness is larger than 100 µm - see Ref [122] where we showed that for this range of thickness the local electrostatic forces become independent of the insulator thickness, reaching the limit of an infinite-thick slab.

To analyze the electrostatic field over a bare metallic substrate, we considered the same probe model of Figure 5.1 but substituting the insulator with a metallic surface located at a distance *z* from the tip apex.

We modeled the cantilever as a simple disc, although in fact it has rectangular or triangular shape. This simplification gives an excellent approximation, provided that the disc radius is chosen properly, as we will discuss in section 5.5. The main reason for using the disc geometry is that it is axisymmetric. Hence, it enables the use of 2D numerical solvers, which are

much faster and accurate than 3D solvers when large geometries including nanometric features (here the apex) have to be calculated.

The electrostatic problem was solved numerically by the finite-element package COMSOL Multiphysics 4.0 (AC /DC electrostatic module). The infinite lateral and vertical dimensions of the simulation box (air and substrate domain) were implemented by using the built-in infinite elements function around an inner domain of finite size having ten times the width and height of the largest tip dimension. Constant potential boundary conditions were assumed on the probe surface and at the bottom of the insulating substrate (here taken as ground), while insulating boundary conditions were used on the lateral and upper sides of the simulation box. The calculation was done with the direct axisymmetric 2D solver PARDISO (calculation time per point between 6 and 10 seconds on a computer with a 2.5 GHz CPU and 4 GB RAM).

The force acting on the probe was calculated by integration of the built-in Maxwell-stress-tensor function over the probe surface. To pass from the 2D calculations to the 3D ones, the corresponding $2\pi r$ factor was included, where r is the distance from the 2D probe surface to the symmetry axis. We estimated the accuracy of our calculations to be better than 1% against the analytical expression of the electrostatic force acting on a conducting sphere in front of an infinite dielectric substrate [84]. To analyze the electrostatic interaction independently of the applied potential and to get rid of non-local contributions, the calculated force $F_{2\omega}(z,\varepsilon_r)$ was converted into *capacitance gradient variations* $\Delta C'(z,\varepsilon_r) = C'(z,\varepsilon_r) - C'(z_0,\varepsilon_r)$, as we already detailed in Ref.[122].

We systematically calculated the capacitance gradient as a function of all the parameters, covering the range of values of interest (R = 1-120 nm, θ=5º-40º, H = 5-20 μm, L = 0-35 μm, ε_r = 1-11, z = 6-800 nm, w = 2 μm) using an automatic script (with a total computational time of 3 weeks). We then implemented a code in Mathematica 7.0 that interpolates the calculated values, generates two functions, corresponding to the metallic and the dielectric substrate respectively, and finally fits them to the experimental data with no need for further finite-element calculations.

5.4 *Effects of the microscopic probe geometry on the local electrostatic interaction.*

The local electrostatic interaction between the probe and the thick insulator depends on the size of the microscopic parts of the probe, and thus on the cone height, *H*, and the cantilever disc radius, *L*. To show it, we analyzed the capacitance gradient variation, $\Delta C'(z, \varepsilon_r)$, as a function of the tip-surface distance *z* (approach curve) for different probes of variable size *H* and *L* but fixed apex radius and cone angle (*R* = 30 nm and $\theta = 30°$). For clarity, we also calculated and separated the capacitance contribution of the cone, $\Delta C'_{cone}(z,\varepsilon_r)$, from the contribution of the cantilever, $\Delta C'_{cant}(z, \varepsilon_r)$, where $\Delta C'(z, \varepsilon_r) = \Delta C'_{cone}(z, \varepsilon_r) + \Delta C'_{cant}(z, \varepsilon_r)$. For a given probe size, we calculated and analyzed the approach curves on both metallic and insulating substrates.

5.4.1 *Metallic substrates*

Figures 5.2a and 5.2b show calculated approach curves, $\Delta C'_{metal}(z)$, on a metallic substrate for probes with variable disc radius *L* = 0, 10, 20 and 30 μm for small (*H* = 5 μm, Figure 5.2a) and large cone heights (*H* = 15 μm, Figure 5.2b). Separated contributions from the cone and cantilever parts are shown in the insets. In all cases, the cone contribution, $\Delta C'_{metal,cone}(z)$, is independent of *L* and *H*. This confirms the functional dependence given by the analytical approximation derived by Hudlet *et al.* in Ref. [80] (dashed line in the insets of Figure 5.2)

$$C'_{metal,cone}(z) = 2\pi\varepsilon_0 \left[\frac{R^2(1-\sin(\theta))}{z(z+R(1-\sin(\theta)))} + \frac{1}{\ln\left(\tan(\theta/2)\right)^2} \left(\ln\left[\frac{H}{z+R(1-\cos(\theta)} \right] - 1 + \frac{R\frac{\cos(\theta)^2}{\sin(\theta)}}{z+R(1-\sin(\theta))} \right) \right] \quad (4.1)$$

where the capacitance gradient associated to the cone is independent of *L* and it includes the cone height *H* through a logarithmic term that cancels out when computing capacitance gradient variations.

The cantilever contribution instead shows a linear dependence on the vertical displacement, Δz, i.e. $\Delta C'_{metal,cant}(z,H,L;z_0) \approx a_{metal}(H,L)\Delta z$, where a_{metal} is a function that increases with *L* and decreases with *H*. The linear dependence is a consequence of the fact that *H , L* >> Δz and hence the Taylor expansion to the first order can be applied. Note that the cantilever contribution becomes comparable to the cone contribution in the case of small cone heights (*H* < *L*), while for *H* > *L* it is almost negligible in front of the cone contribution. Hence, the total capacitance gradient $\Delta C'_{metal}(z)$ is independent of the cone height and cantilever disc radius when *H* > *L* (Figure 5.2b), while for small cone heights when *H* < *L* (Figure 5.2a) it can depend on them through the direct cantilever contribution. For AFM-tips with small cone heights the latter result should be kept in mind, since in general microscopic parts of the probes are assumed not to play any role in the analysis of EFM measurements on metallic substrates.

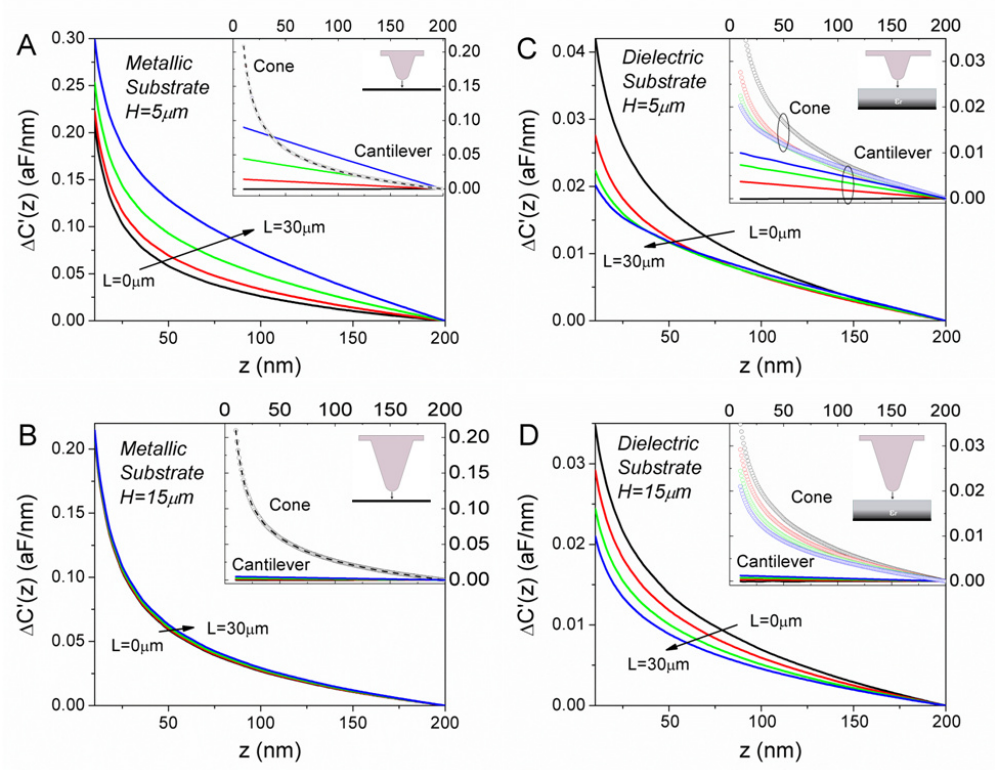

Figure 5.2 *Calculated capacitance gradient approach curves on (a, b) a metallic and (c, d) insulating substrates for probes with (a,c) small (H = 5 μm) and (b,d) large (H = 15 μm) cone heights for different disc cantilever radii (L = 0, 10, 20, 30 μm). In all curves the apex radius and cone aperture angle are R =30 nm and θ = 30°. The dielectric constant of the insulating substrate is ε_r = 6. Insets: separated contributions of the cone (symbols) and cantilever (solid lines) to the total capacitance gradient variations. The dashed line in the inset of (a, b) gives the calculations using the analytical formula of Eq. (5.1) for the cone contribution on a metallic substrate. Reprinted from Ref.* [121] *(copyright 2012 of IOP).*

5.4.2 Thick insulating substrates

Figures 5.2c and 5.2d show the capacitance gradient approach curves calculated for the case of an insulator substrate ($\varepsilon_r = 6$), $\Delta C'_{dielec}(z, \varepsilon_r)$, with the same probe sizes considered in Figures 5.2a and 5.2b, respectively. Again, the insets of Figures 5.2c and 5.2d show the separated contributions of the cone and cantilever. The main difference with respect to the case of a metallic substrate is that on a thick insulator the cone contribution, $\Delta C'_{dielec,cone}(z, \varepsilon_r)$, depends on both the cone height, H, and the disc radius, L. For a given cone height, H, the cone contribution *decreases* with increasing the disc radius.
Moreover, for a given disc radius L, the cone contribution decreases (increases) when increasing the cone height for $H > L$ ($H < L$). This indicates that the microscopic parts of the probe might have an indirect influence on the local tip-surface interaction, thus giving such a complex behavior as theoretically anticipated in Refs. [85, 86, 108, 113, 114]. We support this statement with Figure 5.3, where local and non-local potential distributions are shown for four representative probes corresponding to: (Figure 5.3a) $H = 5\ \mu$m, $L = 0\ \mu$m, (Figure 5.3b) $H = 15\ \mu$m, $L = 0\ \mu$m, (Figure 5.3c) $H = 5\ \mu$m, $L = 30\ \mu$m, and (Figure 5.3d) $H = 15\ \mu$m, $L = 30\ \mu$m. The local voltage drop in the air gap below the tip apex (insets), which ultimately determines the local force acting on the probe, is affected by the dimensions of the microscopic parts of the probe (H and L). The value of this voltage drop follows the same qualitative dependencies on H and L as the cone capacitance gradient contribution described above, thus providing an explanation to that. The effect on the capacitance gradient is less pronounced than on the voltage drop, because the former is an integral quantity that tends to smooth out variations. Note that indirect effects related to the microscopic probe geometry do not happen in the case of a metallic substrate and hence quantifying the electrostatic interaction is clearly easier.

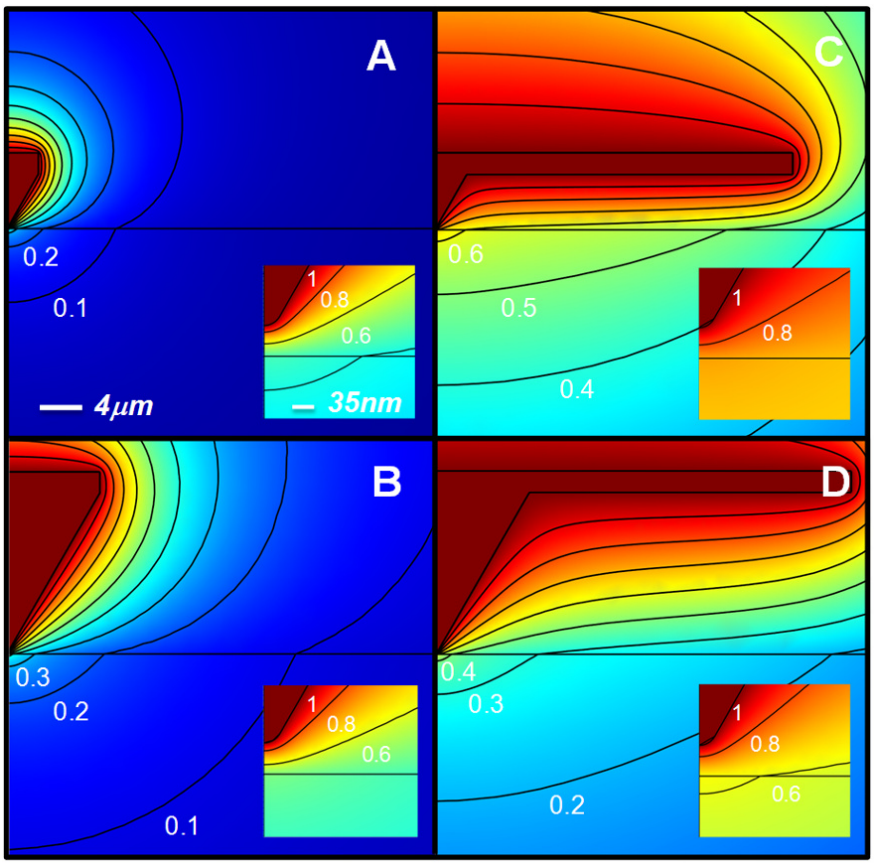

Figure 5.3. *Microscopic (non-local) and nanoscopic (local) (in the insets) electric potential distributions for probes of a given apex geometry (R = 30 nm, θ= 30 °) and variable microscopic geometry: (a) (H = 5 μm, L = 0 μm), (b) (H = 15 μm, L = 0 μm), (c) (H = 5 μm, L = 30 μm) and (d) (H = 15 μm, L = 30 μm). The thick insulator substrate has a dielectric constant of ε_r = 6. The probe is at 1V while the backside of the substrate is at ground, 0 V. Note that the voltage drop in the air gap below the tip (insets), which determines the force acting on it, depends on the microscopic geometry of the probe (cone and cantilever). Only the first 20 μm of the dielectric substrates are shown. The color scale is the same for all the figures. Reprinted from Ref. [121] (copyright 2012 of IOP).*

The cantilever contribution, on the other hand, $\Delta C'_{dielec,cant}(z, \varepsilon_r)$, shows a linear behavior with the tip vertical displacement, Δz, (see Figures 5.2c and 5.2d, insets), that is, $\Delta C'_{dielec,cant}(z;\varepsilon_r) \approx a_{dielec}(H, L, \varepsilon_r)\Delta z$. The slope a_{dielec} increases when increasing L, decreasing H or increasing ε_r. To understand the linear behavior of $\Delta C'_{dielec,cant}(z, \varepsilon_r)$ with Δz, a similar reasoning as for metallic substrate can be followed. Note that also in the case of dielectric substrates, the direct contribution of the cantilever becomes comparable to the cone contribution for small cone heights ($H < L$).

We can now explain the complex dependence of the total capacitance gradient, $\Delta C'_{dielec}(z, \varepsilon_r)$, on H and L given in Figures 5.2c and 5.2d. For probes with a high cone (Figure 5.2d) ($H > L$) the total capacitance is dominated by the cone contribution and hence it *decreases* when increasing the cantilever dimensions (and also when increasing the cone height). Instead, for short cone height probes (Figure 5.2c), when $H < L$, initially the capacitance gradient is dominated by the cone and hence it decreases when increasing L, but at some point it stops decreasing and starts increasing as a result of the direct contribution from the cantilever.

In summary, it has been shown that the local electrostatic force between the probe and a thick dielectric substrate depends on the microscopic geometry and size of the cone and the cantilever mainly due to their indirect effects on the local tip-substrate interaction. In addition, direct effects from the cantilever can be relevant for short cone probes.

5.5 Quantification of the dielectric constant of thick insulators

According to the results presented in section 5.4, the microscopic geometry of the probe needs to be taken into account in any geometrical model used to quantify the local dielectric constant of *thick* dielectric substrates using EFM. In this section, we show that the simplified 2D axisymmetric model of Figure 5.1 can include them in an effective manner, thus optimizing the quantification procedure demonstrated in Ref. [122] by adding a disc to the cone model that we used.

We validated the method with the AM-EFM experiments performed on different insulating substrates (PEN, PMMA, borosilicate glass, mica as dielectric substrates and HOPG as metallic substrate) that we reported and analyzed in Ref. [122] (experimental data kindly provided by Dra. L. Fumagalli). This first set of experiments was obtained using commercial conductive diamond coated probes (CDT-CONTR, Nanosensors). In addition, a second set of measurements was performed on mica and HOPG using another type of conductive diamond coated probes (CDT-FMR Nanosensors), which differ from the previous one only in the cantilever size (450x50x2 μm^3 vs 225x28x3 μm^3, respectively), while they have similar cone heights (12.5 ± 2.5 μm, as obtained from the datasheet), cone angles and apex radii. The spring constants of the probes are different due to their different cantilever geometry (0.2 N/m vs 2.8 N/m, respectively).

As for the case of the numerical calculations, we obtained the capacitance gradient variation $\Delta C'(z,\varepsilon_r)$ from the measured approach force curves $F_{2\omega}(z,\varepsilon_r)$ (see Ref.). The experiments were performed under dry environment (0% RH) by flowing N_2 through the AFM chamber to avoid water layers on the surfaces.

The dielectric constants of the substrates were obtained from the measured capacitance gradient approach curves by using the 2D geometric model in Figure 5.1 and following the two step procedure proposed in Ref. [122], but generalized to include a variable microscopic geometry. First, we calibrated the apex geometry of the probe (R and θ) by a least square fitting of the

metallic theoretical curve to the experimental curve taken on the metallic substrate with *H* and *L* fixed to given initial values. Then, with the obtained probe geometry, the dielectric constant was extracted by a least square fitting of the dielectric theoretical curve to the experimental curve taken on the insulator using the dielectric constant as the only fitting parameter. The same procedure was then repeated for different values of the microscopic geometric parameters *H* and *L* to evaluate how they affect the extracted dielectric constant and the goodness of the fittings. The only constraint set to the values of *H* and *L* was that the goodness of the fitting gave $r^2 > 0.9999$.

Figure 5.4 shows the measured capacitance gradient curves obtained on (a) mica, glass, PEN, PMMA and (inset) HOPG with the CDT-CONTR probe [122], and on (b) mica and (inset) HOPG with the CDT-FMR probe. Note that the noise in Figure 5.4b is higher due to the higher spring constant of the CDT-FMR probes as compared to the CDT-CONTR probes. Examples of the fittings obtained with our procedure are given in Figure 5.4 (solid lines) for $H = 12.5\ \mu$m and $L = 3\ \mu$m, showing very good fitting for both the insulating and metallic substrates.

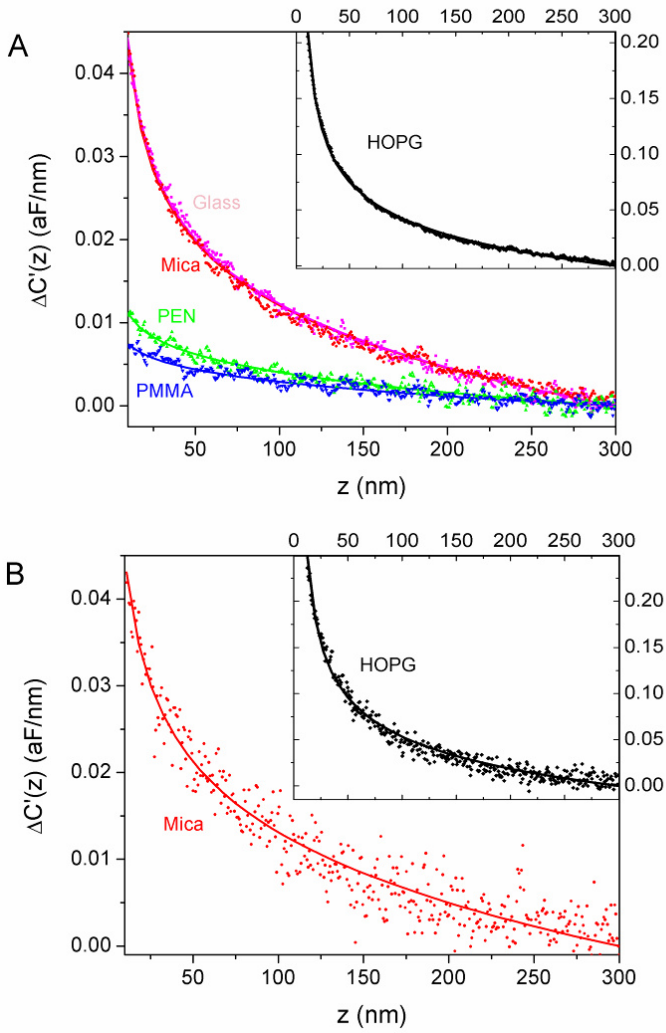

Figure 5.4 *Experimental capacitance gradient as a function of the tip-surface distance obtained (a) with the same CDT-CONTR probe (conductive diamond coated, spring constant 0.2 N/m), on different substrates: HOPG (black), glass (magenta), mica (red), PEN (green) and PMMA (blue) (ref. [122]); (b) with the same CDT-FMR probe (conductive diamond coated, spring constant 2.8 N/m), on HOPG (black) and mica (red). Solid lines correspond to theoretical least square fittings of the data using the 2D geometric model of Fig. 1 with H = 12.5 μm and L = 3 μm. The fitted parameters are given in Table 2. Reprinted from Ref. [121] (c 2009 of IOP).*

Similarly, good fittings can be obtained for other values of *H* and *L*. Figure 5.5 shows the extracted dielectric constant values, ε_r, together with the geometrical parameters of the probe, *R* and θ obtained from the experimental data in Figure 5.4a (CDT-CONTR probe) as a function of the cantilever disc radius *L* and cone height *H*. In Figures 5.5a and 5.5b we observe that the extracted tip radius and cone angle (*R* and θ) are practically not affected by the microscopic probe geometry and size of the probe (*H, L*). This is because good fittings are obtained only for *H* > *L* and for these values, the probe - metallic substrate interaction is nearly independent of the microscopic geometry. On the contrary, Figure 5.5c shows that for a given cone height, *H*, the extracted dielectric constant increases when increasing *L*. Moreover, for a given cantilever disc radius, the dielectric constant increases (decreases) when increasing *H* for *H* > *L* (*H*< *L*). This behavior is clearly reminiscent of the dependence of the local electrostatic interaction between the probe and the thick insulating substrate described in section 5.4.
Remarkably, the dependence of the extracted dielectric constants on the macroscopic parameters *H* and *L* for *H* > *L* can be described by the following simple phenomenological relationship

$$\varepsilon_r(H,L) \approx \varepsilon_{r0}\left[1+\alpha\log\left[H(\mu m)\right]\right]\left[1+\beta\frac{L(\mu m)}{H(\mu m)}\right] \quad H > L\,, \quad (4.2)$$

where, ε_{r0}, α and β are three parameters independent of *H* and *L* and given in Table 5.1 for each substrate.

The results of Figure 5.5c demonstrate that the extracted dielectric constant for a thick dielectric substrate significantly depends on the cantilever disc radius, *L*, and on the cone height *H*. Therefore, care should be taken when choosing these geometrical parameters to quantify the dielectric constant.
In Ref. [122] we showed that one can choose a simplified model that consists of only the cone and no cantilever. There, we obtained good agreement with nominal values, only slightly underestimating them, provided the cone height was set to the higher value of the range given by the manufacturer, i.e. *H* = 15 μm (see Table 5.2).

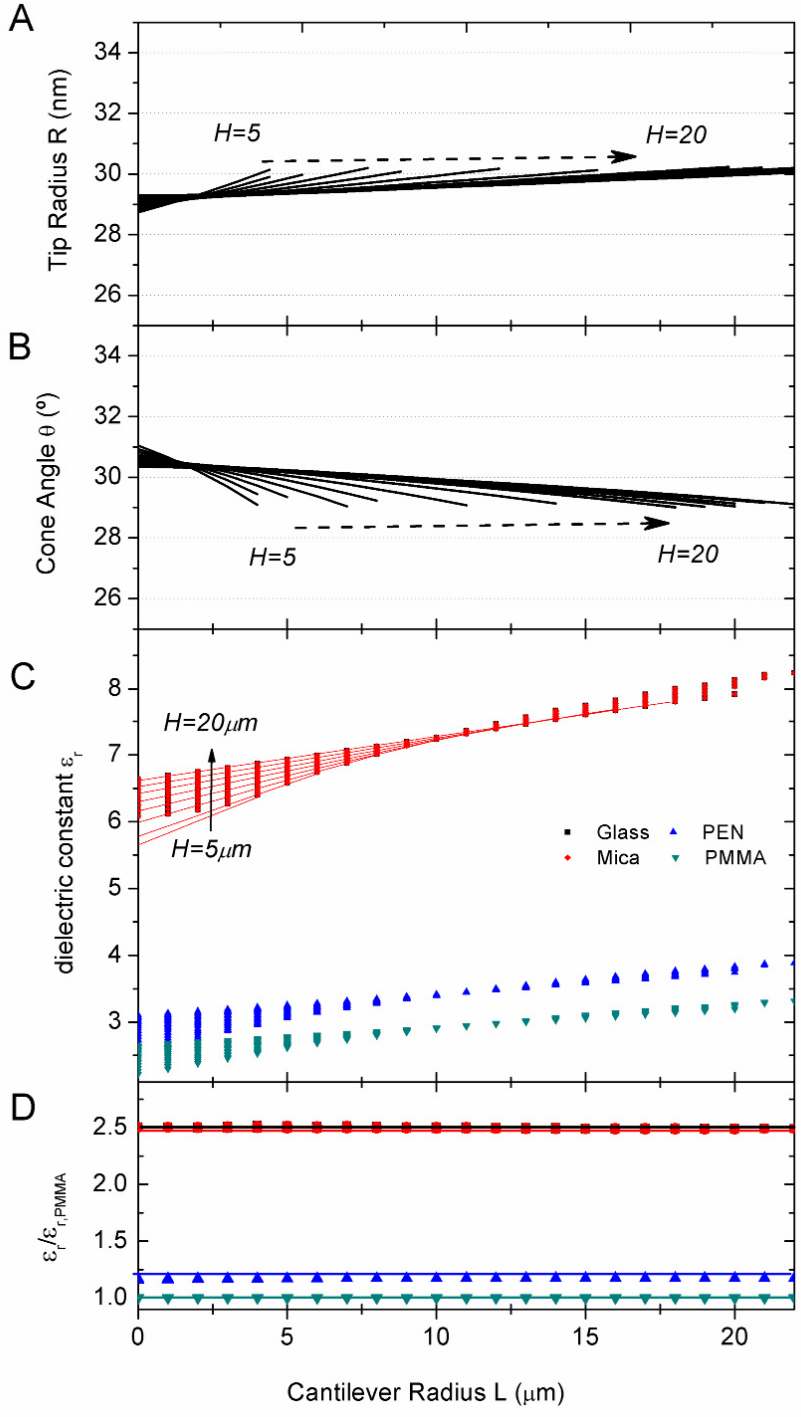
A
Tip Radius R (nm)
H=5
H=20
B
Cone Angle θ (°)
H=5
H=20
C
dielectric constant ε_r
H=20μm
H=5μm
Glass
Mica
PEN
PMMA
D
ε_r/ε_r,PMMA
Cantilever Radius L (μm)

Figure 5.5. *Extracted apex radius (a), cone angle (b) and relative dielectric constant (c) from the data plotted in Figure 5.4a by using the theoretical model with variable L (0-30 μm) and different cone heights H (5-20 μm). (continuous lines). The continuous lines in (c) correspond to the predictions of Eq. (5.2) for the mica substrate. (d) Extracted dielectric constants for glass, mica and PEN (symbols) as a function of H and L, normalized by the values obtained for PMMA for the same H and L. The ratios are almost independent of H and L and roughly equal to the ratios of the nominal values (continuous lines). The data of glass (black) are not visible, because they are identical to the values obtained for mica (red). Only values of H and L giving a fitting with $r^2 > 0.9999$ have been considered. Reprinted from Ref.* [121] *(copyright 2012 of IOP).*

Here, as an alternative approach, we demonstrate that one can obtain more accurate values of the dielectric constant by including the contribution of the cantilever and calibrating its effective length, that is the value of *L*, on a reference substrate. For instance, if we set the cone height to its mean manufacturer value (H = 12.5 μm) and use PMMA as reference substrate (ε_r = 2.6), we obtain L = 3 μm for the disc cantilever radius.

Using these geometrical values, for all the substrates analyzed in the present paper we obtained dielectric constants in perfect agreement with nominal values (see Table 5.2), while the cone model used in Ref. [122] gives slightly smaller values. The additional calibration of *L*, then, provides a simple method for accurate quantification of the dielectric constant of thick dielectric substrates.

In summary, the dielectric constant of a given insulator substrate can be obtained by fitting theoretical approach curves to measured ones, with the dielectric constant as single fitting parameter, provided a probe geometry like the one shown in Figure 5.1 is used with the cone height given by the manufacturer, the apex radius and cone angle being determined from approach curves on a metallic substrate and the effective cantilever radius

Table 5.1 *Phenomenological parameters of Eq. (5.2) extracted for the different substrates and probes used in the present study.*

	$\varepsilon_{r,nominal}$	ε_{r0}	α	β
Probe CDT-CONTR				
PMMA	2.6	1.67	0.462	0.191
PEN	3.2	1.89	0.502	0.198
Mica	6-7	4.15	0.467	0.189
Glass	6.7	4.29	0.446	0.184
Probe CDT-FMR				
Mica	6-7	3.95	0.479	0.171

Table 5.2. *Dielectric constants extracted from the data of Figure 5.5 using the cone and cantilever model with H =12.5 μm and L = 3 μm. For comparison, the dielectric constants obtained using the simplified probe model that consists of only the cone used in Ref.[122] are also given. The fitted radii and angles are R = 28.5 ± 1 nm and θ= 30.8 ± 0.4° for the CDT-CONTR probe and R = 39.5 ± 3.6 nm, θ= 34.8 ± 1.3° for the CDT-FMR probe.*

	$\varepsilon_{r,nominal}$	$\varepsilon_{r,cone+disc}$	$\varepsilon_{r,cone}$ (Ref.[122])
Probe CDT-CONTR			
PMMA	2.6	2.61 ± 0.04	2.40 ± 0.04
PEN	3.2	3.11 ± 0.05	3.00 ± 0.04
Mica	6-7	6.57 ± 0.07	6.20 ± 0.04
Glass	6.7	6.67 ± 0.06	6.20 ± 0.04
Probe CDT-FMR			
Mica	6-7	6.80 ± 0.20	-

being determined from an approach curve on a reference substrate of known dielectric constant.

An intriguing aspect of this procedure concerns the surprisingly small value obtained for the effective parameter *L* as compared with any physical dimension of the cantilevers. In particular, we have obtained the same value of *L* for the two types of probes used in this study, which show rather different cantilever size. This result suggests that the parameter *L* is related to an effective cantilever interaction area rather than to the physical area of the cantilever. Further theoretical investigation in this direction would require the full three-dimensional simulation of the cantilever-probe system, which lies beyond the scope of this work.

Finally, we note that the use of a reference substrate has a further unexpected property, that is, it makes the extraction of the dielectric constants independent from the whole microscopic geometry of the probe (both *H* and *L*). Indeed, the ratios of dielectric constant values extracted for different materials for given *H* and *L* are independent from these geometrical parameters and, at the same time, are equal to *the ratios of the corresponding nominal dielectric constant values*. We show it in Figure 5.5d, where the normalized dielectric constants with respect to the dielectric constant values obtained for PMMA are given (symbols) and compared to the ratios of nominal values (continuous lines). Hence, although the absolute value of the extracted dielectric constant depends on *H* and *L*, its relative value with respect to a reference substrate measured with the same probe does not depend on them. As a consequence, by using a reference substrate of known dielectric constant, the dielectric constants of other substrates can be estimated without knowing the detailed micrometric geometry of the probe. This result can also be read from Table 5.1 where we found that the parameters α *and* β are independent from *H*, *L* and ε_r, while the parameter ε_{r0} is almost linear with ε_r.

5.6 Locality of the electrostatic force signal

Apart from the microscopic dimensions of the cone and cantilever another aspect concerns the microscopic dimensions of the substrate under study. A central role hereby has the thickness of the dielectric substrate that for thin substrates is an important parameter that has to be considered. We showed in contrast in *Ref.*[122] that the measured forces for thick substrates >100μm is independent from the exact substrate thickness.

This indicated that the measurements are not equally sensitive to the whole substrate and we found that we are actually just probing the nanometric volume of the substrate just below the tip. To evidence this we performed simulations for a probe above the dielectric substrate and calculated the volume that is actually contributing to the measured signal. In order to reduce the number of parameters and the complexity of the discussion here, we will only analyze the effect that the local parameters R and θ have on the probe volume. The indirect effects of cone height and cantilever will not be the scope in this discussion. Note that for this reason the cone height is always fixed to *H=15 μm* and no cantilever is used. In any case a different L and H would only lead to a small quantitative change of the results and the qualitative conclusions would remain.

As mentioned above we calculated the volume of the insulator that is actually probed through evaluating the difference in the force density on the substrate with the probe at near and far distance, z_0 and z_{ref}. This resembles a typical experiment where also the force differences rather than the absolute forces are regarded. Such a difference is illustrated in Figure 5.6 for the case of z_0 = 10nm, z_{ref} = 20nm. A roughly exponentially decay in $\Delta C'(z_0)$ density is observed with increasing contour radius (note: logarithmic color-scale), showing that most of the contribution comes from close to the dielectric-air surface.

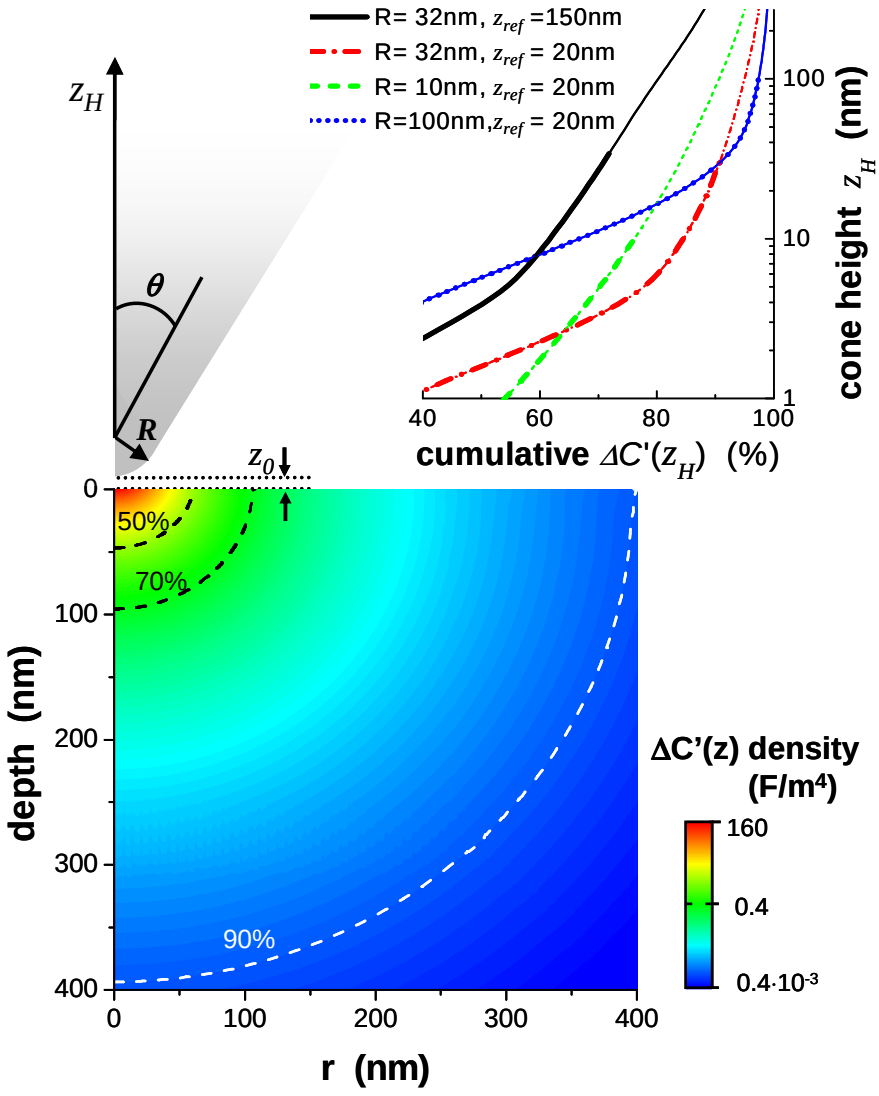

Figure 5.6 *Calculated locality of ΔC'(z) on a ~250μm thick insulator. The ΔC'(z_0) density in the substrate (z_0 = 10 nm, z_{ref} = 20 nm, R = 32 nm, θ = 30º) is given with the contours (dash lines) enclosing the 50%, 70% and 90% of the total variation. Inset: Plot of cumulative ΔC'(z_0) along the probe surface as a function of the cone height z_H for different radii and reference distances. Apex and cone regions of each curve are plotted with thick and thin lines, respectively. Reprinted from Ref. [122] (copyright 2010 of AIP).*

Integration within contours of equal value allows evaluation of the build up of $\Delta C'(z_0)$ while penetrating into the insulator. The integrated values of density distribution, which gives the 50% of the signal confined in a hemispherical region of $r_{50\%}$ ~ 50 nm radius below the tip apex and the 70% within 100nm, confirm the locality of the interaction. Note, however, that the 90% contour penetrates rather deeply into the insulator down to ~ 400 nm. Interestingly this volume does not shrink with the tip radius, e.g. $r_{90\%}$ ~ 617 nm for R = 10 nm, whereas it is slightly smaller with larger tip radius, e.g. $r_{90\%}$ ~ 360 nm for R = 100 nm. This is because with smaller apex the signal is increasingly located on the cone, thus spreading into a larger volume in the substrate.

This is evidenced in the inset of Figure 5.6, which plots the build-up of $\Delta C'(z_0)$ on the probe surface. The apex and cone region of each curve are indicated as thick and thin lines, respectively and illustrate that for R = 32 nm, z_0 = 10nm and z_{ref} = 20 nm, the apex accounts for more than 90% of the total variation, while it reaches 99% for R = 100 nm. Conversely, with smaller radii (R = 10 nm) or larger reference distances (z_{ref} = 150 nm) the cone contribution gains importance (22% and 28% respectively) and correspondingly the probed volume in the insulator gets larger.

5.7 Conclusion

In this chapter we demonstrated by means of finite-element numerical calculations that the microscopic parts of an EFM probe (the cone and the cantilever) affect the local electrostatic interaction between tip apex and a thick insulator substrate, and hence the quantification of the dielectric constant at the nanoscale.

We showed that these effects can be included into a simple 2D axisymmetric probe model. By adding a disc with an effective radius that accounts for the cantilever contribution, we optimized the quantification procedure that we demonstrated in Ref. [122] based on a simple cone model.

Perfectly accurate dielectric constants can be obtained, provided that the cone height is set similar to the real height of the cone and that the cantilever disc radius is taken as a parameter that gives the effective interaction area of the cantilever. This parameter is independent of the dielectric constant of the substrate and hence it can be determined using a reference insulating substrate of known dielectric constant.

Furthermore, the use of a reference substrate enables to obtain the dielectric constants of other substrates even without knowing the detailed microscopic geometry of the probe (cone height and disc radius).

These results offer a general framework under which accurate quantification of the local dielectric constants of thick insulators can be achieved using EFM, opening new possibilities for the dielectric characterization of insulating materials at the nanoscale in general but especially for bio-samples that cannot be measured on metallic substrates.

Also the fact that the actual volume that is probed in the insulating substrate, was found to be located in a very confined region below the apex, indicates that measurements of bio-membranes on thick insulating substrates will be sensitive to the bio-membrane itself and quantitative extraction on such materials will be possible. Experiments performed within our research group confirms this assertion [123](in preparation)

6 Dielectric constant of biomembranes in electrolyte solutions

6.1 Abstract

In the previous chapters we showed that dielectric constant quantification of biomembranes on both metallic and insulating substrates can be performed with nanoscale spatial resolution in air environment. However, the physiological environment of biomembranes is an electrolyte solution. In the present chapter we report quantitative imaging of the local dielectric polarization properties of supported biomembranes in electrolyte solutions with nanoscale spatial resolution. Local dielectric imaging has been achieved by probing high frequency (>1 MHz) electric forces at the nanoscale, which, we show, are dependent on the local dielectric properties of the materials. we demonstrate the possibility to quantify these frequency and ionic concentration dependent electric forces by means of finite element numerical calculations including calibrated probe geometry, and deriving from it the nanoscale dielectric constant of the materials in electrolyte solutions. The developed method is demonstrated by imaging and quantifying the dielectric properties of a 20 nm-thin SiO_2 test microstructure and 5 nm-thin lipid bilayer nanopatches. The technique shows high sensitivity to the dielectric properties of the materials enabling distinguishing insulator materials with close dielectric response. Present results open fascinating possibilities in fields like Electrophysiology or Electrochemistry where quantitative measurements of the nanoscale dielectric properties of materials under electrolyte solutions can provide new insights not accessible until now.

This chapter reproduces almost literally the manuscript in preparation: " Nanoscale dielectric polarizability of biomembranes and insulating thin films imaged and quantified in electrolyte solutions", by G. Gramse, A. Dols, M. A. Edwards, L. Fumagalli and G. Gomila. In this manuscript I was in charge of performing the experimental and the theoretical parts and of processing the results. In this work I followed some experimental and theoretical suggestions by M. A. Edwards. Moreover, the lipid bilayer samples were prepared by A. Dols-Pérez. The manuscript was written by me in collaboration with my supervisor.

6.2 Introduction

We described in the Introduction of this thesis that one of the distinctive aspects of Atomic Force Microscopy (AFM) is its capability to investigate nanoscale phenomena in the liquid environment. This capability has made of AFM an invaluable instrument for in situ imaging and surface characterization of materials under liquids, with a strong impact in fields like Biology[124, 125] or Electrochemistry[52, 126], among others. The number of surface material properties that can be determined with AFM based techniques under liquids covers a wide range of possibilities, including surface stiffness[127-129], electrochemical activity[52, 130], piezoelectric response[95, 131, 132] or surface charge/potential [60, 61, 63, 69, 73, 74, 77].

But still at present some physical surface properties cannot be imaged and quantified in the liquid environment with AFM based techniques. Among them a major example refers to dielectric polarization, the property of materials to orient permanent or induced electric dipoles in response to an external electric field. Measuring dielectric polarization phenomena at the nanoscale under electrolyte solutions is extremely challenging due to the complex frequency dependent response of the electrified solid-electrolyte interface and to the presence of large stray contributions preventing access to local material properties. But yet dielectric information of material surfaces under electrolyte solutions is fundamental to understand a broad variety of electric phenomena in fields like Electrophysiology or Electrochemistry, where dielectric properties of materials at the nanoscale in electrolyte solutions can play an important role. This situation contrast with nanoscale dielectric polarization studies of material surfaces in air, which can be thoroughly

analyzed with a variety of techniques such as scanning capacitance microscopy[13], scanning polarization force microscopy[38], scanning impedance microscopy[11, 14], electrostatic force microscopy[122, 133] or scanning microwave microscopy[98].

In this chapter we propose and implement a high frequency (> 1 MHz) Electrostatic Force Microscopy method for liquid imaging, and its corresponding finite element numerical modeling, able to provide local quantitative dielectric contrast of sample surfaces in electrolyte solutions with nanoscale spatial resolution. High frequencies are used because we found that at these frequencies the electric force acting on a conductive tip in close proximity to a sample becomes local and sensitive to its local dielectric polarization properties. The imaging and quantitative capabilities of the technique are unambiguously demonstrated on a 20 nm thin silicon dioxide microstructure and on 5 nm thin supported lipid bilayer nanopatches in electrolyte solution.

6.3 Experimental Set up

The experimental set up used for the measurements is schematically detailed in Figure 6.1. It consists of an AFM system compatible with both liquid and electrical measurements. A voltage of frequency ω_{el} in the MHz range, whose amplitude is modulated with a frequency ω_{mod} in the kHz range, is applied between a conductive cantilever probe and the bottom of the sample. The high frequency voltage, which is beyond the cantilever mechanical resonance frequency, bends the cantilever in a static way due to the non-linear dependence of the actuation force on the applied voltage. The low frequency signal modulates this cantilever bending allowing an increased signal to noise detection. Dielectric images are obtained by scanning the probe at constant height with respect to the substrate at distances much larger than the Debye screening length (which is typically 10 nm in 1mM electrolyte solutions).

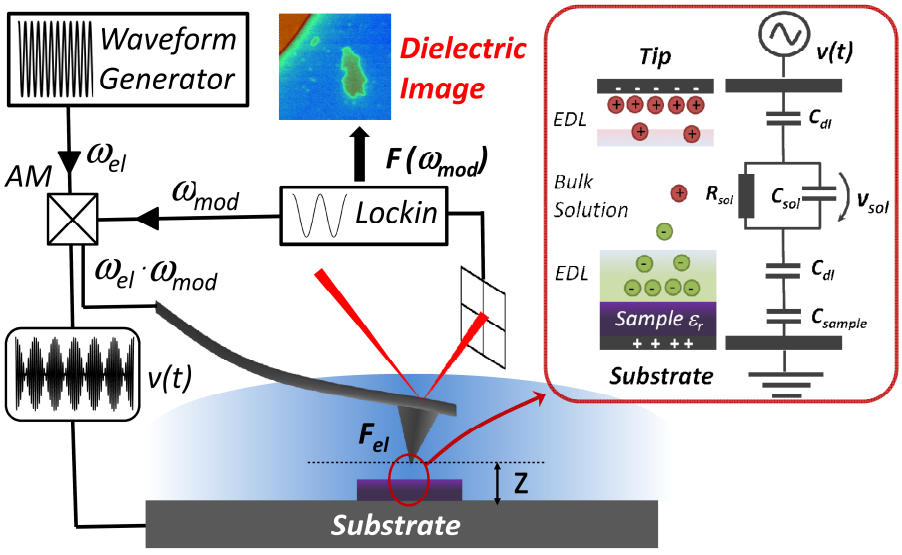

Figure 6.1 *EFM set up to measure the local dielectric polarization properties of samples in electrolyte solution. An amplitude modulated ac-potential with frequency ω_{el} (>MHz) and modulation frequency ω_{mod} (<10kHz) is applied between a conducting tip and a substrate in an electrolyte solution. An external lockin amplifier detects the modulated bending of the cantilever. The cantilever bending depends, among other factors, on the local dielectric properties of the sample, thus allowing imaging them when the probe is scanned at constant height with respect to the substrate.*

Inset: Electrochemical model and equivalent circuit of a surface element of the tip-solution-sample system, where C_{dl} is the double layer capacitance, R_{sol} is the solution resistance, C_{sample} is the sample capacitance and V_{ac} is the applied voltage.

6.4 Theory of Electrostatic Force in Liquid

This experimental set up is able to produce local dielectric images of material surfaces in electrolyte solutions for applied frequencies above a critical frequency in the >MHz range due to the frequency dependent response of the force acting on the probe. Indeed, in an electrolyte solution the electric force acting on the conducting probe in response to an ac applied voltage $V_{ac}(t)$ is given by [134]

$$F_{elec}(z,t) = \frac{1}{2}\frac{\partial C_{sol}(z)}{\partial z}V_{sol}^{2}(z,t) \tag{6.1}$$

where V_{sol} is the voltage drop in the solution and C_{sol} is the capacitance of the solution gap between probe and sample. From the analysis of the equivalent circuit for the probe-solution-sample system sketched in the inset in Figure 6.1 one finds that the voltage drop in the solution is dependent on the dielectric properties of the sample (see details in appendix). In particular, it can be shown that the voltage drop in the solution, and hence the electric force, are detected only for frequencies higher than a critical frequency, f_{act} given by $f_{act}^{-1} = 2\pi R_{sol}\left(C_{eq} + C_{sol}\right)$ where R_{sol} is the solution resistance and C_{eq} is given by $C_{eq} = C_{dl}\cdot C_{sample}\Big/\left(C_{dl} + 2C_{sample}\right)$ with C_{sample} and C_{dl} being the sample and double layer capacitances, respectively.

An estimation of f_{act} can be obtained by assuming a simple parallel plate model for the cantilever and for the tip end and neglecting double layer contributions (see appendix), giving

$$f_{act} = \frac{c\cdot\Lambda}{2\pi\cdot\varepsilon_0\cdot\varepsilon_{r,water}}\left(\frac{\varepsilon_{r,sample}z}{\varepsilon_{r,water}h}+1\right)^{-1} \approx 3MHz\cdot c(mM)\left(\frac{\varepsilon_{r,sample}z(nm)}{\varepsilon_{r,water}h(nm)}+1\right)^{-1} \tag{6.2}$$

where c is the solution ionic concentration, Λ the molar conductivity, h the thickness of the sample, $\varepsilon_{r,water}=78$ is the relative dielectric constant of water, $\varepsilon_{r,sample}$ the sample relative dielectric constant and z the distance between the sample and the tip (or cantilever). Assuming typical experimental parameters, i.e. Λ=13.3 S $m^{-1}mol^{-1}$, c=1 mM, h=10 nm and ε_r=4, and taking $z=z_0$=10 nm for the tip-sample distance and $z=H+z_0$ for the cantilever-sample distance, where H =10 µm is the cone height, we obtain $f_{act,cant}$=60 kHz and $f_{act,tip}$=3 MHz, for the cantilever and tip, respectively. Therefore cantilever electric actuation can be achieved in electrolyte solutions for frequencies $f> f_{act,cant}$~kHz but local dielectric contrast can only be measured when $f> f_{act,apex}$~MHz.

6.5 Materials and Methods

In order to validate this theoretical prediction we have considered a test structure consisting of a 20 nm thin silicon dioxide stripe 2.5 µm wide on a highly doped silicon substrate. Experiments have been performed with a commercial AFM (Nanotec Electronica S.L.) equipped with a custom made liquid cell compatible with electrical measurements made from Teflon and using apiezon-wax for sealing. Solid platinum tips from *Rocky Mountain Nanotechnology* with a spring constant of k~0.3N/m and resonance frequency in solution of ~6 kHz were used. All solutions were prepared from MilliQ and $KClO_4$. We used the Agilent 33250A as external waveform generator and an external Anfatec eLockIn 204/2 to modulate the signal. For the quantitative interpretation of the experiments finite element numerical simulations have been performed with *Comsol MultiPhysics 4.0*, in which we modeled the AFM-tip as a truncated cone of height H with an aperture angle, θ, plus a spherical apex of radius R located at a distance, z, above the dielectric sample of height, h, diameter, D, and dielectric constant ε_r. To account for the very thin layer of native oxide on the silicon substrate a distributed capacitance was added on the conducting part of the substrate, C_{native} (see appendix for further details on the numerical calculations). To make forces measured at different applied

voltages comparable we represent in all experiments a normalized value with units of capacitance gradient, $C'(z) = 2F_{elec} \big/ V_{ac,0}^2$.

6.6 Results

In Figure 6.2a a topographic image of the $Si0_2$ microstructure obtained in conventional intermittent contact mode is shown together with the dielectric images obtained in aqueous electrolyte solutions for two ionic concentrations 1 mM (Figure 6.2b) and 10 mM (Figure 6.2c). The dielectric images were measured with the tip scanning at constant height (z=100nm) over the baseline of the substrate and changing the frequency of the applied voltage every 10 lines from 20MHz (top) to 100kHz (bottom).

As it can be seen the dielectric images nicely reproduce the presence of the 20nm thin silicon dioxide stripes showing the capability to perform local dielectric images in electrolyte solutions. We note from the images that there is only local contrast for applied frequencies above a given characteristic value, which is here f>100 kHz for c=1 mM and f>1MHz for c=10 mM. This is in agreement with the simple dependence of the critical actuation frequency on ion concentration predicted from Equation (6.2), $f_{act} \sim c$. As shown in Figure 6.2d, for rising frequencies the contrast increases monotonically over two orders of magnitude until it plateaus at about 10 MHz for c=1 mM and about 100 MHz (estimated) for c=10 mM. Due to the specific cone geometry this crossover is much smoother than it would be predicted from the simple parallel plate model. We verified this with numerical calculations including a realistic cone geometry for the probe (see appendix for further information).

Notice that due to the high dielectric constant of water ($\varepsilon_{r,water}$=78) the measured capacitance gradients are almost two orders of magnitude higher than in air ($\varepsilon_{r,air}=1$) thus allowing to reach excellent signal to noise ratios by applying the small voltages required to avoid electrochemical surface reactions (here $V_{ac,p}=0.5\ V$).

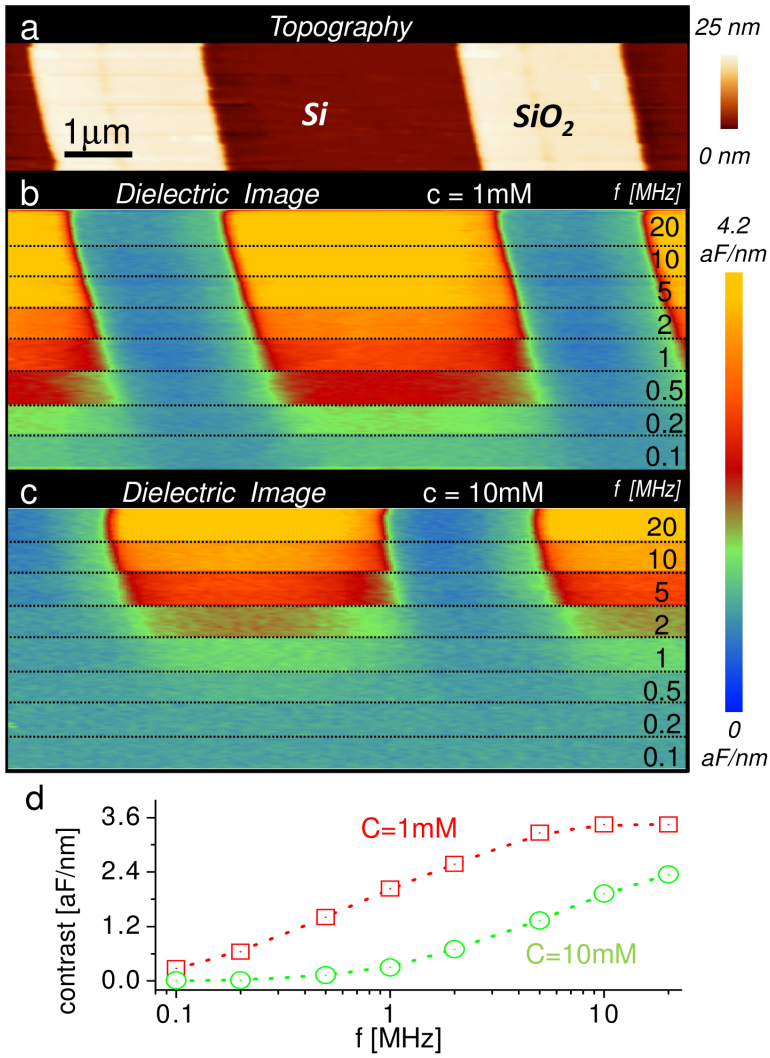

Figure 6.2 *(a) Topography and (b,c) dielectric images (ΔC') of 20 nm thin and 2.5 µm wide Si/SiO_2 microstripes obtained in electrolyte solutions. Dielectric images were obtained at constant height z=100nm from the Si baseline with ion concentrations c=1mM (b) and c=10mM (c) with 0.5 V applied. The applied frequency f_{el} was changed from 20MHz to 0.1MHz to show how the image contrast depends on frequency and finally disappears at low frequencies.(d) Plot of the dielectric contrast (ΔC') extracted from image (b) and (c) as a function of the applied frequency. Dotted line is to guide the eyes.*

The contrast displayed in Figure 6.2 reflects the dielectric properties of the materials, and not only its topography. This can be better evidenced from the approach force curves measured on the Si^{++} substrate and on a SiO_2 stripe, respectively, shown in Figure 6.3 for different frequencies and for a concentration of 1 mM. If the measurements were only sensitive to the oxide topography the curves would appear shifted one with respect to the other by just a distance equal to the thickness of the oxide, i.e. 20 nm, what is clearly not the case, thus showing the sensitivity of the measurements to the local dielectric properties of the sample surface.

The sensitivity to the local dielectric properties of the sample surface allows using these measurements to extract the dielectric constant of the materials. To this end we adapt the procedure developed for air measurements [91, 122]. First, for a given frequency, one calibrates the probe geometry (R and θ) and the native oxide capacitance (C_{native}) by a best fit of numerical calculations to an approach curve measured on the bare Si^{++} substrate. Then one uses these parameters to fit the approach curve on the $Si0_2$ stripe with the dielectric constant being the single fitting parameter.

Proceeding in this way we obtained R=96 nm, θ=10°, C_{native}=1.1 μF/cm^2 and ε_r=4.4±0.5 for the measurements performed at 20 MHz These values are in very good agreement with probe specifications, native oxide dielectric properties and dielectric constant of $Si0_2$, showing the excellent quantitative capabilities of the method.

The sensitivity of the results to the dielectric constant of the thin film are illustrated by the dashed lines in Figure 6.3, which correspond to the results assuming ε_r=5 and ε_r=3. The above predictions are robust against variation of the frequency as can be seen in Figure 6.3 from the excellent adjustment of the theoretical calculations to the experimental results for frequencies 5 MHz and 2 MHz, which have been obtained with the above derived parameters *with no fitting parameter*.

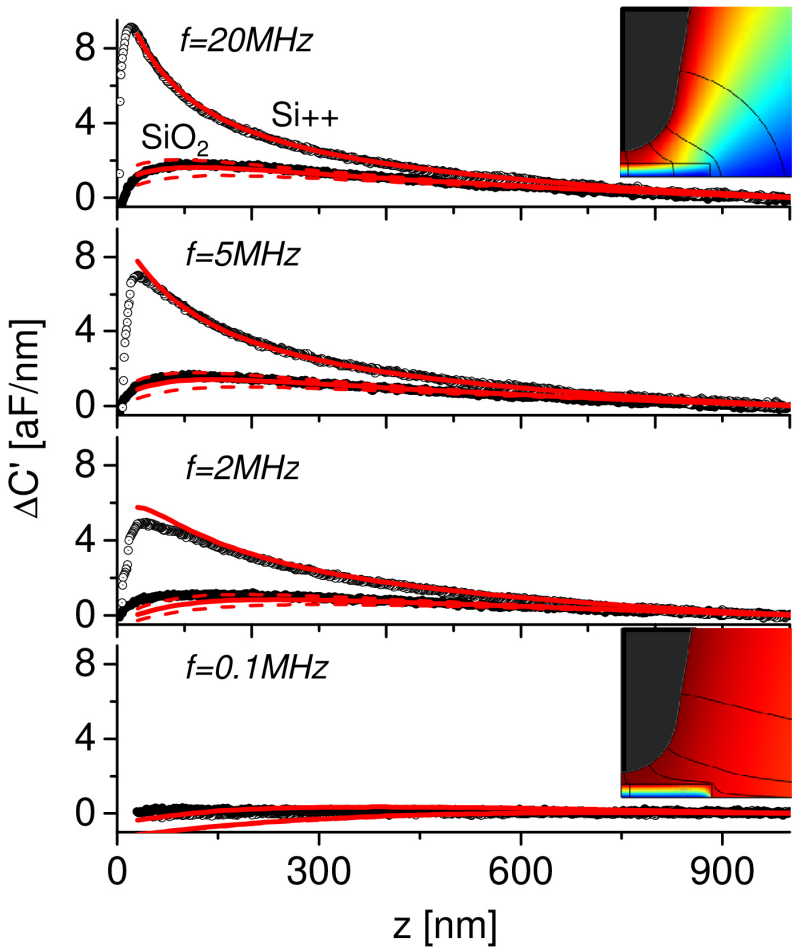

Figure 6.3 *(Symbols) Approach curves onto the Si^{++} and the SiO_2 parts of the microstructure measured at various frequencies in electrolyte solutions (c=1mM and V_{ac}=0.5 V). Solid lines represent numerical results obtained considering a probe with tip radius R=96nm, cone angle θ=10°, a native oxide capacitance C_{native}=1.1µF/cm^2 and a dielectric constant $\varepsilon_{r,oxide}$=4. Dashed lines represent $\varepsilon_{r,oxide}$=3 and 5. Additional model parameters used in the numerical calculations are: cone height H=10 µm, SiO_2 thickness h=20 nm and SiO_2 diameter D=3 µm. Insets show the respective simulated potential distributions for two frequencies (20 MHz and 100 KHz).*

Only at lower frequencies and for very close distances to the surface the theoretical predictions deviate from the measurements since the model does not include the true 3D sample geometry and the effect of double layer capacitances, which become relevant in the corresponding situations. The above results show unambiguously that the local dielectric constant of materials can be obtained in electrolyte solutions with the proposed technique.

Further insight on why the measurements are sensitive to the local dielectric properties of the sample can be gained by comparing the calculated potential distributions shown in the insets of Figure 6.3 for a high frequency (20 MHz) and a low frequency (100 kHz). As it can be seen, only at high frequencies a potential gradient develops below the tip enabling field lines of different intensity to pass through the oxide layer leading to an electrostatic force on the apex sensitive to the local oxide dielectric properties.

As an example of application of the developed methodology, we consider the determination of the local dielectric constant of biomembranes in electrolytic solutions. As we have mentioned earlier, the dielectric constant of biomembranes is a parameter especially important in cell electrophysiology as it ultimately determines the ion membrane permeability, the membrane potential formation or the action potential propagation velocity, among others[93, 135-137]. Knowing the dielectric properties of biomembranes with nanoscale spatial resolution is very important due to the nanoscale hetereogeneous composition of plasma membranes (e.g. lipid rafts). However, no technique is able to provide this quantity with the required nanoscale spatial resolution and in electrolyte solution. As representative model of a biomembrane we consider here dipalmitoylphosphatidylcholine (DPPC) single bilayers. Phosphatidylcholines are the main components of eukaryotic cell membranes[138], and DPPC is one of the most widely used phosphatidylcholine models. The DPPC bilayer patches have been formed on the $Si/Si0_2$ sample studied above by means of the liposome fusion technique.

Figure 6.4 shows the topography (a) and phase (b) images of a single DPPC bilayer (5 nm thin) adsorbed onto the Si/SiO_2-sample in an aqueous solution

with an ionic concentration of 1mM. The topography and phase images show that the lipid bilayer spans over the Si^{++} substrate and the $Si0_2$ stripes. The corresponding dielectric image, obtained at constant distance, *z*=80nm, and at frequency *f*=80 MHz, is shown in Figure 6.4c. The dielectric image clearly resolves the 5 nm thin lipid bilayer on the Si^{++} substrate and, to a lesser extend, on the $Si0_2$ stripe. This is also illustrated in the corresponding profiles taken along the lines marked and shown in Figure 6.4d. Even double lipid bilayers, occasionally present and 10 nm thin (marked with an arrow in Figure 6.4c) can be distinguished in the dielectric image. A zoom onto an isolated DPPC patch next to a bare SiO_2 portion taken at a closer distance (z=50 nm) is shown in Figure 6.4f where we can observe the good spatial resolution of the dielectric image clearly resolving features below 100 nm. These results show the dielectric imaging capabilities of the proposed technique for soft biological samples.

Quantification of the measurements and extraction of the corresponding dielectric constants of the materials present in Figure 6.4 ($Si0_2$ and DPPC) can be obtained by quantitative analysis of the force approach curves following the procedure detailed above. Figure 6.4e shows representative curves measured on Si^{++}, $Si0_2$ and DPPC.

Figure 6.4 *Patches of DPPC adsorbed onto Si/SiO_2 structures. (a) Topography, (b) phase and (c) dielectric image are shown for a large scan. The dielectric image is obtained at a constant lift height of 80nm (d) Profiles of topography, phase and electric image. Notice, in the dielectric image $\Delta C'V_d(z=0)$ is set to zero. (f) Zoom onto an isolated patch next to the SiO_2 structure. The electrical image is acquired at a constant lift height of 50nm. (e) Experimental approach curves (dotted) onto Si (blue), SiO_2 (red) and DPPC patch (green). Applied voltages V_p=0.25V, f=80MHz. Simulations with $\varepsilon_{r,SiO2}$=4 and $\varepsilon_{r,DPPC}$=3.2 are shown as solid lines. Tip radius R=45nm, cone angle θ=15° and native oxide capacitance C_{native}=0.71mF/cm^2 were calibrated as described above. Dashed lines represent simulations for $\varepsilon_{r,DPPC}$=2.2 and 4.2. Additional model parameters used in the numerical calculations: Ion concentration c=1mM, oxide/lipid height and diameter h_{SiO2}=20nm, D_{SiO2}=3μm, h_{DPPC}=5nm, D_{DPPC}= 1.5μm and cone height H=10 μm.*

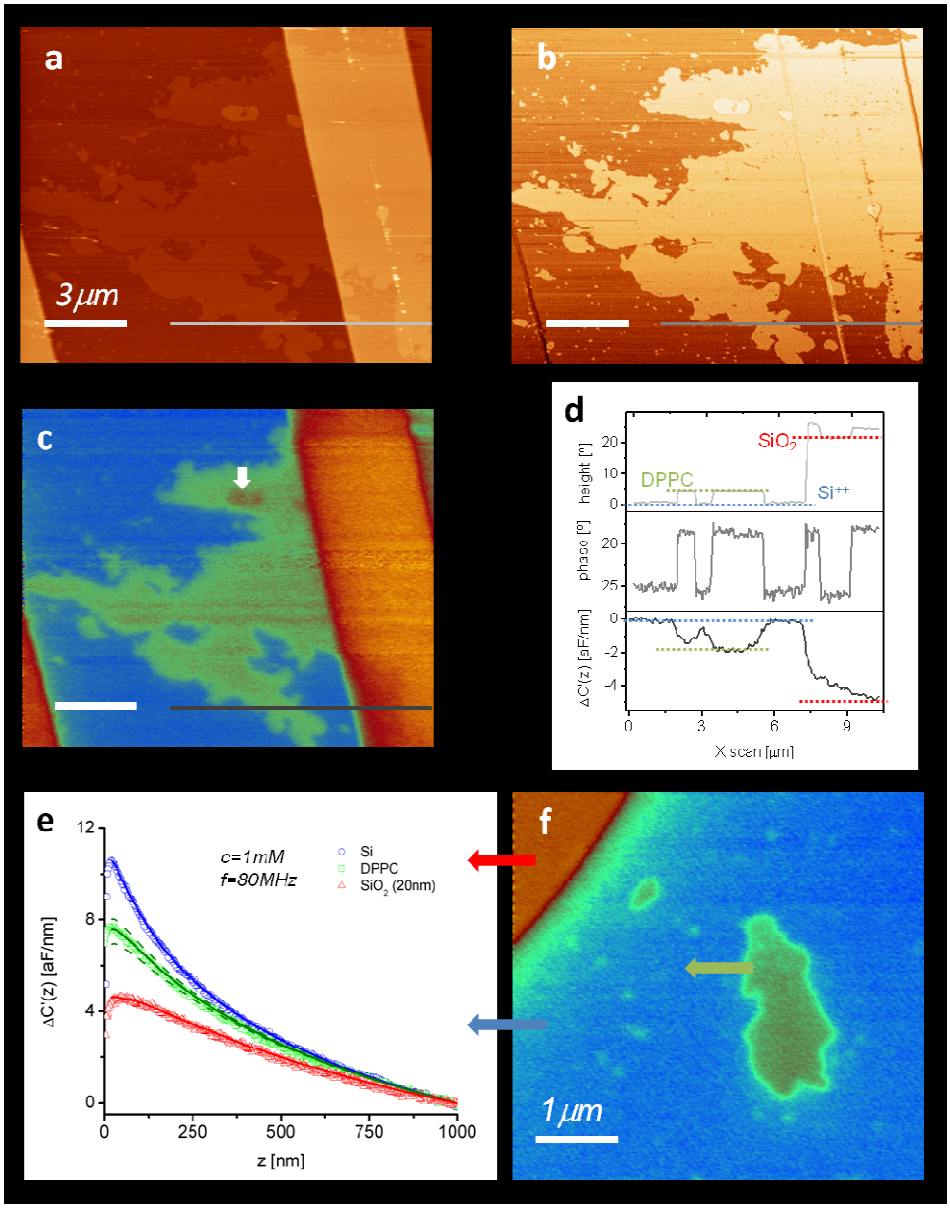
a
3 µm
b
c
d
height [°]
20
10
0
SiO2
DPPC
Si++
phase [°]
20
25
ΔC'(z) [aF/nm]
0
-2
-4
0
3
6
9
X scan [µm]
e
12
8
4
0
ΔC'(z) [aF/nm]
c=1mM
f=80MHz
Si
DPPC
SiO2 (20nm)
0
250
500
750
1000
z [nm]
f
1 µm

6.7 Discussion

Quantification of the measurements gives $\varepsilon_{r,Si02}$=4±0.2 for the $Si0_2$, confirming the above findings, and $\varepsilon_{r,DPPC}$=3.2±0.1 (error bounds from the fitting routine) for the DPPC lipid bilayer. This value is slightly larger than the usual theoretical value quoted for the hydrophobic part of lipid bilayers [139] (ε_r=2-2.5), or the nanoscale value measured by us in dry air conditions for the so called purple membrane [19, 91]. However, it is remarkably close to ε_r~3[140, 141] predicted by recent simulations including the contributions from the water/lipid interface and polar heads. Moreover, putting together the bilayer thickness and the obtained dielectric constant the capacitance per unit area of the DPPC bilayer turns out to be $c_m=\varepsilon_0 \varepsilon_{r,DPPC}/h$=0.57 μF/cm^2. This value is in excellent agreement with experimental values reported in literature and obtained from macroscopic impedance based measurements on supported lipid DPPC layers on gold electrodes (c_m =0.52-0.57 μF/cm^2)[142]. The proposed approach then has demonstrated the capability to quantify the dielectric constant of a biomembrane with the great advantage over macroscopic techniques to provide also information on the thickness of the sample and a spatial resolution below 100 nm.

In the present implementation of the technique we showed a spatial resolution below 100 nm and a remarkable sensitivity to the dielectric constant of the materials, which can discriminate between materials of relatively close dielectric response such as silicon dioxide (ε_r~4) and lipids (ε_r~3). These results, however, do not represent the absolute limits of the technique. At present the technique is essentially limited by the need to be operated at distances larger than several times the Debye screening length. By using novel instrumental advances and appropriate theoretical models, it should be possible to remove this limitation and increase both the spatial resolution and the dielectric sensitivity of the technique.

6.8 Conclusion

In summary, we have demonstrated for the first time imaging and successful quantification of dielectric polarization properties on material surfaces in electrolyte solutions with nanometric spatial resolution. The proposed technique is applicable to both inorganic samples and biosamples, thus opening a number of fascinating possibilities in fields like Electrophysiology or Electrochemistry where nanoscale information on the dielectric properties of materials under electrolyte solutions was not accessible until now.

6.9 Appendix

6.9.1 Dependency of electric force on voltage drop in solution V_{sol} and sample dielectric constant ε_r

In an electrolyte solution the electric force acting on the conducting probe in response to an applied ac voltage $V_{ac}(t) = V_{ac,0} \cdot \sin(\omega t)$ is given by [134]

$$F_{elec}(z,t) = \frac{1}{2} \frac{\partial C_{sol}(z)}{\partial z} V_{sol}^{2}(z) \tag{6.3}$$

The relationship between the voltage drop in the solution and the applied voltage can be obtained by solving the circuit depicted in Figure 6.5. The following derivations in this paragraph are based on a parallel plate model.

After some algebra one finds:

$$\left|V_{sol}(\omega)\right| = V_{ac,0} \frac{f / f_{eq}}{\sqrt{1 + f^{2}\left(1/f_{eq} + 1/f_{sol}\right)^{2}}} \tag{6.4}$$

where we have introduced two characteristic frequencies given by $f_{eq}^{-1} = 2\pi C_{eq} R_{sol}$ and $f_{sol}^{-1} = 2\pi C_{sol} R_{sol}$ and the equivalent capacitance corresponding to the series combination of the sample capacitance and double layer capacitance $C_{eq} = C_{dl} \cdot C_{sample} \Big/ \left(C_{dl} + 2C_{sample}\right)$. Notice, that since the double layer capacitance is usually much bigger than the sample capacitance it can be neglected except for the case when measuring a metallic substrate with a metallic tip.

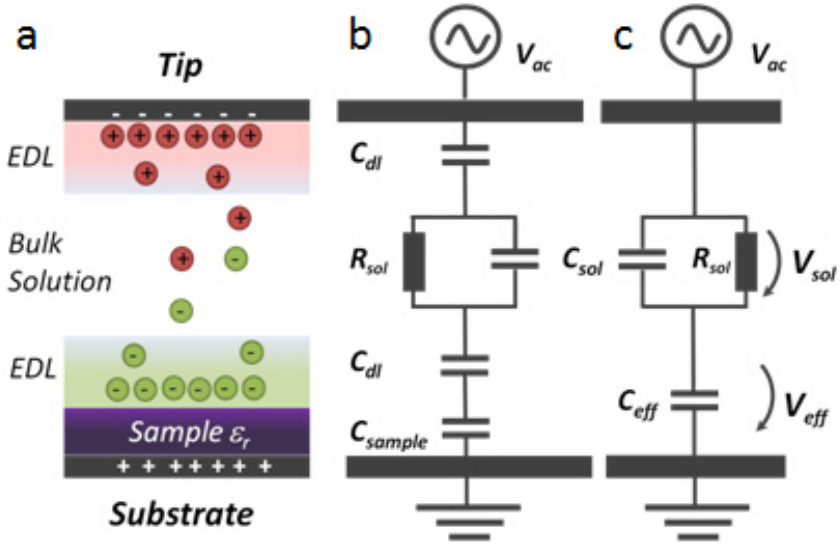

Figure 6.5 Electrochemical model (a) and equivalent circuit (b,c) of a surface element of the tip-solution-sample system, where C_{dl} is the double layer capacitance, R_{sol} is the solution resistance, C_{sample} is the sample capacitance and V_{ac} is the applied voltage. The double layer and the sample capacitance can be added up to an effective capacitance, C_{eq}, as described in the text.

As one can read from Eq. (6.4), the voltage drop, V_{sol}, is highly frequency dependent. There is a high frequency limit where some voltage drops off in the solution and an electrostatic force can be measured, a low frequency limit where the voltage drops off completely in the dielectric and consequently no force can be measured:

$$\begin{aligned} \lim_{f\to\infty} F_{elec} &= 1/2\, C'_{sol}(z)\cdot C_{eq}\Big/\left(C_{eq}+C_{sol}\right) \\ \lim_{f\to 0} F_{elec} &= 0 \end{aligned} \tag{6.5}$$

and a transition between both cases.

We visualize this in Figure 6.6a where we plot the calculated normalized force (capacitance gradient C'(z) per surface area) as a function of the frequency for

the circuit depicted in Fig. 1c with the parameters: $R_{sol}=z(\Lambda c)^{-1}$, $C_{sol}=\varepsilon_0\varepsilon_{r,water}/z$, $C_{eq}=\varepsilon_0\varepsilon_{\rho,sample}/h$, Λ=13.3 S $m^{-1}mol^{-1}$, h=10 nm, z_0=10 nm, $\varepsilon_{\rho,water}=78$ and $\varepsilon_{r,sample}=4$.

The transition frequency defined as $f_{act}=f\left[\frac{1}{2}F_{elec}(f\to\infty)\right]$ and marked by the dotted lines in Figure 6.6a is:

$$f_{act}=\left[2\pi R_{sol}\left(C_{eq}+C_{sol}\right)\right]^{-1}=\frac{c\cdot\Lambda}{2\pi\cdot\varepsilon_0\cdot\varepsilon_{r,water}}\left(\frac{\varepsilon_{r,sample}z}{\varepsilon_{r,water}h}+1\right)^{-1}$$
$$f_{act}\approx 3MHz\cdot c(mM)\left(\frac{\varepsilon_{r,sample}z(nm)}{\varepsilon_{r,water}h(nm)}+1\right)^{-1} \quad (6.6)$$

From Eq. (6.6) we argued in section 6.3 that nonlocal electric cantilever actuation (where $z=H+z_0\sim 10\mu m$) can be achieved in electrolyte solutions for frequencies $f>f_{act,cant}$~kHz, but local dielectric contrast from the apex (where $z=z_0\sim 10nm$) can only be measured when $f>f_{act,apex}$~MHz.
Another important consequence of Eq. (6.6) visualized in Fig. 6.6b is that for low (high) distances, z, and large (small) sample thicknesses, h, the actuation frequency gets $f_{act}=f_{sol}$ ($f_{act}=f_{eq}$).

This finding is important since it means that when approaching the tip to the sample, and once the relaxation frequency of the solution, f_{sol}, is reached, the transition frequency is **independent** from the distance, z, and from the thickness, h, of the dielectric sample. In such case the actuation frequency just

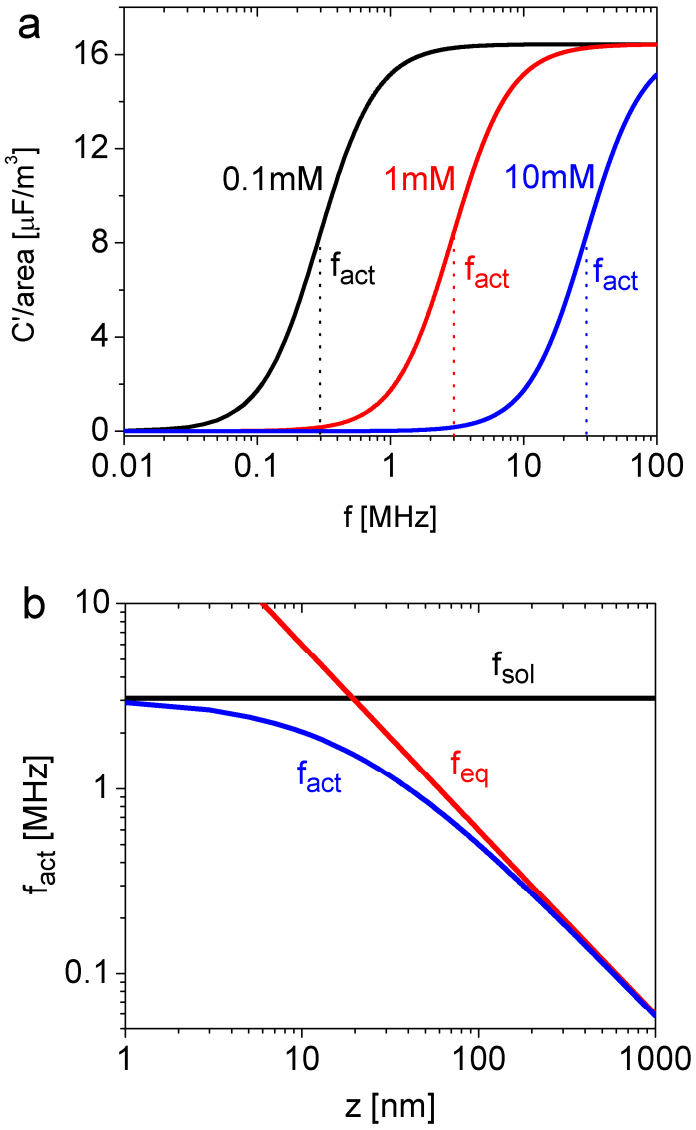

Figure 6.6 *(a) Normalized force on a parallel plate configuration consisting of a dielectric (ε_r=4, h=10nm) and an ion containing domain (ε_r=78, z=10nm) for changing ion concentrations c=0.1mM, 1mM and 10mM (black, red and blue). (b) Evolution of the actuation frequency with changing tip sample distance, z (c=1mM). For high separations $f_{act}=f_{eq}$ and for low separations $f_{act}=f_{sol}$.*

depends on the ion concentration and is $f_{act} \approx 3MHz \cdot c(mM)$. This defines ultimately the frequency necessary to obtain local dielectric contrast during a complete force distance curve. We visualize this is in Figure 6.7, where we plot the corresponding approach curves for the case of a low and a high frequency (*f=1/2 f_{sol}* and *f=2 f_{sol}*) and different sample dielectric constants. As can be seen, different dielectric constants gives clearly more contrast at high frequency. Moreover the curves at high frequency are steeper indicating a higher locality of the signal.

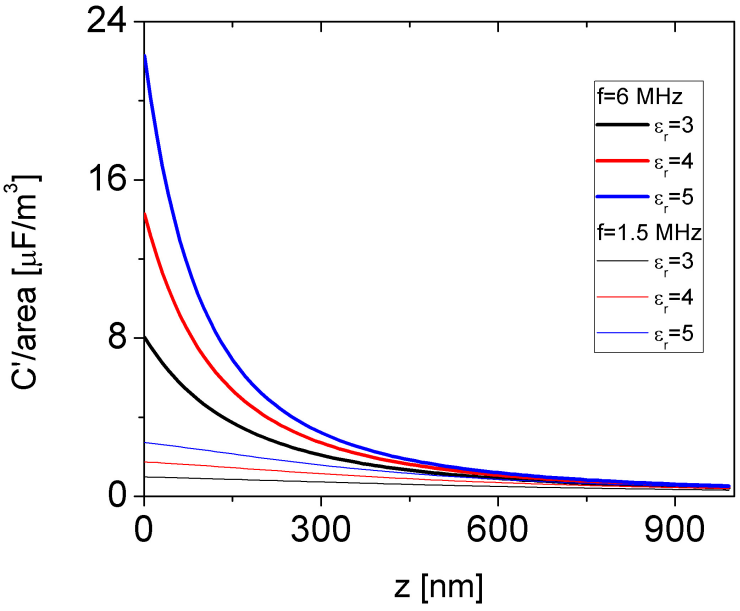

Figure 6.7 *Normalized force approach curves for a parallel plate configuration at high frequency (thick lines, f=2 f_{sol} =6MHz) and low frequency (thin lines, f=1/2f_{sol}=1.5MHz). Other parameters are: h=10nm and $\varepsilon_{r,sample}$=5 (blue), 4 (red), 3 (black), c=1mM, Λ=13.3 S $m^{-1}mol^{-1}$.*

6.9.2 Data Interpretation using Finite Element simulations

Measured forces obtained with the described heterodyne detection method were normalized to give $C'(z) = 2F_{elec} / V_0^2 = 4F_{elec,f_{\mathrm{mod}}} / V_0^2$, where V_0 is the amplitude of the applied ac-potential with the frequency *f* and $F_{elec,f_{\mathrm{mod}}}$ is the measured electrostatic force modulated at a frequency f_{mod}.

For the quantitative interpretation of the experiments we compared our results to forces calculated with a finite element model of the AFM tip above the dielectric sample and substrate. To obtain the electrostatic force acting on the specific tip geometry the equation $\nabla\left(\left(\sigma + i\omega\varepsilon_r\varepsilon_0\right)\nabla V\right) = 0$ was solved using the electrostatic AC/DC module of Comsol Multiphysics 4.0, and from its solution, the harmonic force on the AFM-tip was calculated by using the built-in Maxwell stress tensor. All simulations were carried out in the 2D axisymmetric mode (electric quasistatics, meridional electric currents).

The geometry was defined like shown in Figure 6.8 with the tip parameters: tip radius, *R*, cone angle, θ, and cone height *H*. The sample is defined by the parameters: sample height, h, sample radius, l, and sample dielectric constant $\varepsilon_{r,mem}$. Notice, the sample is a cylinder since we are working in axisymmetric 2D mode. To account for the native oxide on the highly doped silicone sample we added a distributed capacitance on top of the conducting substrate that is set to ground. The solution is defined by its dielectric constant $\varepsilon_{r,sol}$ and its solution conductivity σ_{sol} =c Λ_{sol}, depending on the electrolyte concentration, c, and the molar conductivity Λ_{sol}.

The domain containing the solution is enclosed by the outer boundary conditions *electric insulation* or $\vec{n} \cdot \vec{J} = 0$. Notice, in order to cancel out any effect from the finite size of the simulated volume we added an additional outer simulation box where we use the function “infinite elements” to move the outer boundaries to infinity. The defined geometry was meshed refining especially the tip and sample surface and solved using the parametric solver PARDISO with the frequency as parameter. The Maxwell-Stress-Tensor was integrated over the whole tip surface to obtain the tip force.

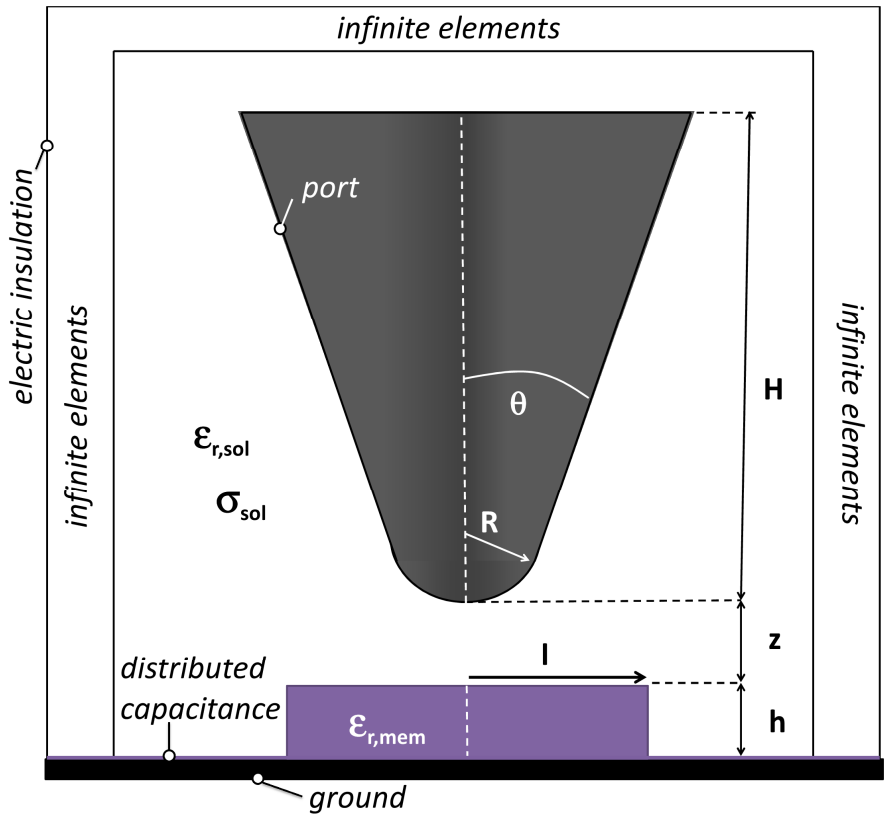

Figure 6.8 *Schematics of simulated model. The AFM-tip is defined by its tip radius, R, cone angle, θ, and cone height H. Cone height is fixed to H=15µm. The sample is defined by its sample height, h, sample radius, l, and sample dielectric constant $\varepsilon_{r,mem}$. A distributed capacitance is added on the conducting substrate. Tip and sample are surrounded by water defined by its dielectric constant $\varepsilon_{r,sol}$ and solution conductivity $\sigma_{r,sol}$. Extension of solution simulation box is infinity (infinite elements).*

To facilitate the data analysis simulations were carried out for an extensive set of parameters (*R = 25-125 nm; θ = 10–30 °; h = 5, 20nm; l = 750, 1500 µm; c = 0.1, 1, 10 mM; f = 20 kHz – 80 MHz; z = 10- 1000 nm;* C_{thin} *= 0.035-0.25 F/m*^{2}*,* $\varepsilon_{r,mem}$ *= 2-10*) and the data was interpolated using *Mathematica 7* to obtain finally a fitting function for the experimental data analysis. In this way we are able to investigate the effect of every simulation parameter almost like with a normal analytical function and we can extract the sample-dielectric constant fitting best to the measured data.

6.9.3 Calculating Forces: Parallel Plate Model versus Cone Model Simulations

Although, many valuable insights can be gained from investigating the electrostatic force in a parallel plate configuration, there are substantial quantitative differences between the force in such a configuration and the more realistic tip cone-substrate model. We show this in Fig. 5 where we plot (a) the frequency dependency of the force at z=15nm and (b) the distance dependency of the force at a fixed frequency *f*=20MHz for the parallel plate model (thick line) and the cone model (dashed line). The forces are calculated for a 5nm thin and laterally infinite dielectric of ε_r=4. As one observes in Figure 6.9a the frequency transition is much smoother for the cone model and (nonlocal) forces are still present at frequencies below 100 kHz. In general it becomes difficult to define a unique transition frequency since apex and cone contribute at different frequencies. Also the approach curves at fixed distance are much smoother for the cone model and rise for *z*>100nm almost logarithmically with decreasing distance, whereas in the parallel plate model the forces rise much steeper close to the surface.

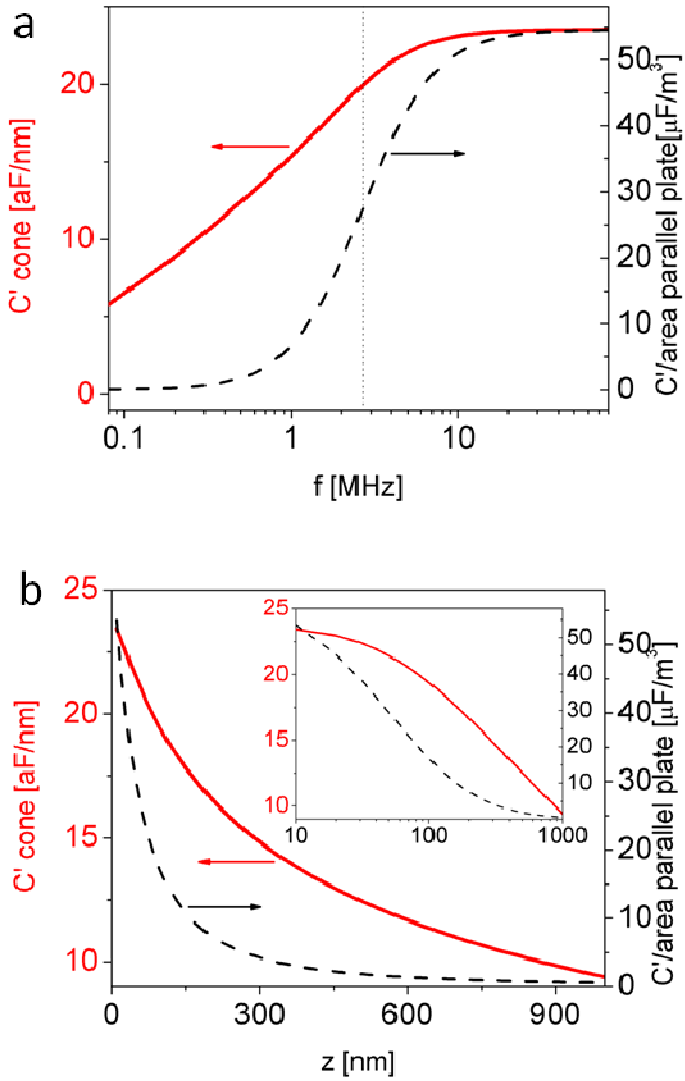

Figure 6.9 *Comparison of electrostatic force calculated for the parallel plate model (dashed, black) and the finite element cone model (solid, red). (a) For varying frequency and fixed distance z=15nm. (b) For varying distance z and fixed frequency f=20MHz. Other parameters are: cone height H=15μm, ion concentration c=1mM, molar conductivity Λ=13.3 S m^{-1}mol^{-1}, apex radius R=60nm, cone angle θ=30°, dielectric thickness h=5nm and dielectric constant ε_r=4. Results for the parallel plate model are normalized by the area. The dotted line represents the actuation frequency of the parallel plate model.*

7 Conclusion and Summary

7.1 Conclusions

The initial objective of my thesis consisted in the development of a current sensing-AFM based technique to measure the dielectric constant of biological samples in their natural ion containing liquid environment. However, with the time we noticed, also from theoretical calculations that this is going to be a very tough aim. The primary experimental difficulty, as also noticed by other researchers, is to develop a probe that can be used to measure topography, but at the same time shields well stray capacitances and can be used for local, electrical current measurements. To approach the problem from a different direction, I also started to test EFM to see whether one can perform quantitative dielectric measurements of biosamples on metallic substrates with it – at this time still in air. And as I showed in chapter 4 even in a DC-detection mode this yielded very good quantitative results of the dielectric constant on purple membrane patches.

I continued with EFM experiments also in the AC-detection mode what encouraged me and also the rest of the group to further explore the capabilities of EFM. In continuation I worked on another more theoretical aspect that was dealing with the interpretation of measurements on insulating substrates like mica. This came just very recently to an end and the scientific community and our group has now a systematic methodology to analyze also dielectric measurements on insulating substrates. This extends the applicability of dielectric measurements to a considerably bigger number of biological samples that require insulating substrates like glass or mica.

However, through all this time in parallel I was trying to make EFM also work in liquid and to elucidate experimentally and theoretically the origin of electrostatic forces in liquid solution. At some point I probably asked myself the right question and I did the right experiments to understand that the frequency-dependency of the electrostatic force is the key. The final result of all this work is the successful implementation of an EFM-based technique to measure the dielectric constant of biosamples in liquid solution as I showed in chapter 6 on the example of lipid bilayers. This technique allows now the investigation of polarization properties of systems that only remain stable in ion containing liquid solutions. Therefore it may open completely new areas of research in the field of Biology.

7.2 Perspectives

The thesis presented here is no closed work and as mentioned in chapter 5 the group is working on the application of the accumulated knowledge to new experiments. Now, that we have a better understanding on the origin of the electrostatic force in thick insulating substrates, also measurements of biomembranes and other samples on these substrates can be interpreted and the dielectric constant can be extracted.

The new developed EFM-technique for measurements in liquid environment is ready to be used for the study on relevant biological membrane-systems. Currently, we are working on the measurement of multi-component phospholipid systems to investigate whether there is a dielectric contrast between both components and if it is big enough to be resolved. This would enable the use of this technique to resolve membrane domains in a label free way which cannot be distinguished solely by their topography.

Then, probably also other membrane systems can be investigated and by increasing the measurement-frequency it will be also possible to increase the ion concentration up to c=0.1M, the natural values of most biological specimen.

Of course the technique is not limited just to membrane systems; also objects with other geometries can be measured. Also on the technical side I see still a lot of potential to increase the sensitivity, resolution and functionality of the technique by for example applying the frequency modulation detection scheme.

Apart from its applicability in liquid environment the implemented detection scheme and the developed theoretical framework show also a route

to access local information on the dielectric constant and conductance in more complex samples like bacteria or virus by performing tomography-type experiments sweeping the frequency during the measurement. In this case the frequency range necessary for the measurement would be probably much lower as simulations performed in our group indicate.

7.3 Summary/Resumen (en Castellano)

Introducción y objetivos

El objetivo de mi tesis era desarrollar nuevas técnicas y métodos para medir las propiedades dieléctricas de biomembranas en aire y en su medio natural, es decir, en solución líquida. La constante dieléctrica (ε_r) de las biomembramas es un parámetro especialmente importante en la electrofisiología celular, ya que fundamentalmente determina la permeabilidad iónica de la membrana, la formación del potencial de membrana o la velocidad de propagación del potencial de acción, entre otros.

El AFM es una herramienta extremadamente versátil para investigar propiedades eléctricas a nanoescala, y por ello constituye una buena técnica candidata para la cuantificación de las propiedades dieléctricas de las biomembranas a nanoescala. Aunque existen algunas técnicas basadas en el AFM capaces de investigar las propiedades de polarización, continúa siendo difícil extraer valores cuantitativos de ε_r de las medidas, especialmente en medio líquido.

Una de las razones radica en la parte instrumental, ya que para los estudios en la nanoescala tienen que medirse cantidades muy pequeñas, y este proceso puede verse entorpecido por ruido electrónico como puede ser el caso, por ejemplo, en las técnicas basadas en la detección de corriente eléctrica. En principio, las técnicas de detección de fuerza electroestática disponen aquí de una ventaja, ya que las sondas utilizadas para la detección de la fuerza son extremadamente sensibles y naturalmente se suprimen señales eléctricas no locales y no deseadas. Otro aspecto importante se atribuye a la falta de modelos cuantitativos suficientemente precisos para relacionar la fuerza medida con el valor de la constante dieléctrica de la muestra. En realidad, para realizar medidas en sustratos aislantes como son la mica o el vidrio, que a veces son necesarios para muestras biológicas, todavía no se dispone de

ningún modelo cuantitativo. Por otra parte, hasta ahora no se han publicado medidas de propiedades dieléctricas en medio líquido, que para algunas muestras biológicas es fundamental para mantener la funcionalidad.

Como consecuencia de las limitaciones existentes de las medidas dieléctricas, el objetivo de este trabajo fue extender las capacidades cuantitativas de la Microscopía de Fuerzas Eletroestáticas para hacer imágenes dieléctricas de biomembranas con resolución espacial a nanoescala. En particular, los tres objetivos hacia los que he enfocado mi trabajo son:

1. Evaluar la posibilidad de ejecutar con Microscopía de Fuerzas Electroestáticas (EFM) mediciones dieléctricas cuantitativas en bimoembranas sobre sustratos metálicos y en aire, lo que puede ofrecer una mayor precisión con respeto a las técnicas de detección de corriente eléctrica.

2. Extender la aplicabilidad de mediciones dieléctricas cuantitativas al caso de sustratos aislantes como vidrio o mica para facilitar su uso con biomembranas que no pueden prepararse en sustratos metálicos.

3. Desarrollar un método para hacer imágenes dieléctricas en medio líquido basado en los principios de la Microscopía de Fuerzas Electroestáticas. Y finalmente, llevar a cabo mediciones dieléctricas a nanoescala en biomembranas en su medio líquido natural.

En las secciones que siguen a continuación aparece resumido cómo se lograron cada uno de estos objetivos.

1. Medidas cuantitativas de la constante dieléctrica de biomembranas con DC-EFM

A diferencia de trabajos previos del grupo, que se basaron en la medida directa de la capacidad, $C(\varepsilon_r)$ con un detector de capacidad de ruido ultra bajo, aquí he demostrado que también es posible extraer la constante dieléctrica de la muestra, ε_r, con un acercamiento más simple que puede aplicarse en

cualquier microscopio de fuerza atómica comercial sin necesidad de otros sistemas electrónicos sofisticados. Con esta aproximación se mide la fuerza electroestática, $F_{el}(\varepsilon_r)$, en la punta conductora del AFM aplicando un potencial dc entre la punta y el sustrato conductor mientras se escanea a una distancia establecida sobre el sustrato y fuera de contacto. Finalmente, se calcula la constante dieléctrica de la muestra a partir de su medida eléctrica y topográfica. Para validar la aproximación he utilizado una muestra de dióxido de silicio antes de aplicar el método a una biomembrana sobre sustrato conductor.

Este trabajo constituye el primer paso de nuestro grupo de técnicas de medidas de corriente (CS-AFM) hacia la Microscopía de Fuerzas Electroestáticas. He podido demostrar, con una aproximación experimental muy simple y controlada y un marco teórico apropiado, que es posible extraer la constante dieléctrica local de muestras aislantes finas con éxito como se demostró previamente con CS-AFM.

A todo esto, descubrí que EFM puede ofrecer mediciones más precisas, ya que las contribuciones no locales debidas al chip y la palanca se suprimen y la punta del AFM como sensor de fuerza es muy preciso. Además tiene el potencial de dar señales con un rango de ruido con órdenes de magnitud más bajo que en la detección de corriente del AFM (especialmente cuando se utiliza en el modo ac-EFM).

2. Cuantificando la constante dieléctrica de sustratos aislantes gruesos utilizando EFM

Este capítulo trata de extender la metodología desarrollada en el capítulo anterior a sustratos aislantes gruesos en lugar de sustratos metálicos. Como he mencionado, el uso de sustratos aislantes, tales como el vidrio o la mica, resulta ser muy ventajoso cuando se trabaja con biomembranas soportadas.

El trabajo resumido aquí se constituye sobre un primer estudio donde hemos demostrado que es posible extraer la constante dieléctrica de las mediciones de EFM utilizando un procedimiento de calibración basado en simulaciones de elementos finitos. En este proceso tan sólo se calibran los parámetros que definen la geometría nanométrica de la punta, es decir, el

radio del ápice y el ángulo del cono, y entonces la constante dieléctrica del sustrato, ε_r, se puede extraer en un segundo paso.

Aquí, a continuación, he investigado los efectos que tienen las partes microscópicas de la punta del AFM (es decir, la palanca y el cono) sobre la extracción de la constante dieléctrica. Este trabajo también estuvo motivado por el hecho de que en nuestro trabajo anterior todavía subestimábamos en parte la constante dieléctrica de los sustratos aislantes medidos.

A diferencia del caso de medidas sobre sustratos metálicos donde la forma microscópica no tiene ningún efecto importante para la extracción de constante dieléctrica de una muestra, esto cambia si se trata de sustratos dieléctricos gruesos. Por consiguiente, he analizado de forma sistemática la influencia de la altura del cono y del área de la palanca en la interacción electroestática local entre la punta y el sustrato y, por lo tanto, la cuantificación de la constante dieléctrica.

La clave reside en que las partes microscópicas de la punta tienen un efecto indirecto sobre la distribución potencial alrededor del ápice y del cono inferior que definen las contribuciones locales de la fuerza medida. Esto es lo que he demostrado con las gráficas correspondientes de la distribución de potencial alrededor de la punta y las curvas de aproximación *dC/dz* resultantes sobre el sustrato que al final representan la medida.

Finalmente propongo una metodología de calibración que ofrece una geometría determinada de la punta y la posibilidad de extraer la constante dieléctrica de sustratos dieléctricos desconocidos. Además, también discuto la dependencia local de este tipo de medida.

Además del beneficio directo que tiene este trabajo para la caracterización de aislantes gruesos a nanoescala, también constituye el fundamento para la cuantificación dieléctrica de muestras dieléctricas finas sobre sustratos aislantes, lo que es esencial para el trabajo con muestras biológicas.

3. Medidas de la constante dieléctrica de biomembranas en soluciones electrolíticas

Además de las dificultades con el sustrato que pueden aparecer cuando se trabaja con muestras biológicas, otro aspecto de todavía mayor importancia es el medio que rodea la muestra. Generalmente en Biología es necesario un medio que contenga iones y agua para que la muestra mantenga su estructura natural y también su función. Pero aunque el AFM puede ser operado en un medio ambiente líquido, hasta la actualidad no existe ningún método que haya podido medir imágenes dieléctricas en solución iónica.

Aquí presento la primera implementación de una técnica que da acceso a imágenes y la cuantificación de las propiedades de polarización dieléctrica de materiales en soluciones iónicas y a la nanoescala. La aproximación que presento está basada en una nueva implementación de EFM en medio líquido que consiste en la medición de fuerzas eléctricas en el rango de frecuencia 1-100 MHz y no en el rango usual de 10-100 MHz. En este rango de frecuencias de MHz demuestro que la fuerza entre muestra y punta presenta de improvisto una dependencia local sobre las propiedades dieléctricas de la superficie del material, mientras que una dependencia local de este tipo se pierde en frecuencias más bajas.

Finalmente he demostrado con éxito la adquisición de imágenes dieléctricas a nanoescala de materiales en soluciones electrolíticas. En particular he mostrado imágenes de una capa de óxido delgado e islas de bicapas de fosfolípidos. La información dieléctrica inequívocamente facilitada por las imágenes queda demostrada por su cuantificación, llevada a cabo con cálculos numéricos de elementos finitos de la fuerza eléctrica actuando sobre la punta, dando la constante dieléctrica local de los materiales. También hay que mencionar que esta es la primera vez que se puede medir la polarización dieléctrica de una membrana en su medio fisiológico y con una resolución espacial a la nanoescala. Los resultados muestran el papel relevante que juegan los grupos polares del cabezal del fosfolípido en la respuesta dieléctrica.

Los resultados mostrados aquí abren un amplio abanico de nuevas posibilidades. Por un lado, permitirán explotar las capacidades únicas de la

EFM (y las técnicas relacionadas) para examinar las propiedades conductivas y no conductivas de objetos y materiales en el medio natural líquido a la nanoescala de una forma similar a como se hace convencionalmente en el aire.

Por otro lado, y probablemente esta es la parte más importante, los resultados permitirán investigar las propiedades de polarización de sistemas que sólo permanecen estables en soluciones líquidas que contienen iones y que hasta ahora no han podido ser abordadas. Me refiero básicamente a las muestras pertenecientes al campo de la Biología y la Electroquímica.

8 Appendix

8.1 Acronyms

Abbreviation	Description
AC	alternating current
AFM	atomic force microscopy / microscope
C-AFM	conductive atomic force microscopy
CS-AFM	current sensing atomic force microscopy
DC	continuous current
EFM	electrostatic force microscopy
KFM	kelvin force microscopy
NIM	nanoscale impedance microscopy
SCM	scanning capacitance microscopy
SEM	scanning electron microscopy
SFM	scanning force microscopy
SPM	scanning probe microscopy
STM	scanning tunneling microscopy
HOPG	highly oriented pyrolytic graphite
SMM	scanning microwave microscopy
SECM	scanning electro-chemical microscopy

8.2 Publications

G. Gramse, I. Casuso, J. Toset, L. Fumagalli and G. Gomila
Quantitative dielectric constant measurement of thin films by DC electrostatic force microscopy
Nanotechnology 20, 395702, 2009

L. Fumagalli, **G. Gramse**, D. Esteban-Ferrer, M. A. Edwards, and G. Gomila
Quantifying the dielectric constant of thick insulators using electrostatic force microscopy
Applied Physics Letters 96, 183107, 2010

G. Gramse, G. Gomila and L. Fumagalli
Quantifying the dielectric constant of thick insulators by electrostatic force microscopy: Effects of the microscopic parts of the probe
Nanotechnology 23, 205703, 2012

G. Gramse, A. Dols, M. A. Edwards, L. Fumagalli and G. Gomila
Nanoscale polarization properties of biomembranes imaged and quantified in electrolytic solution
In preparation

L. Fumagalli, **G. Gramse**, A. Dols and G. Gomila
Quantitative nanoscale dielectric microscopy of nanoparticles and biomembranes on thick insulating substrates
In preparation

L. Fumagalli, **G. Gramse** and G. Gomila
Quantification of electrostatic force microscopy measurements with sharpened probes for high spatial resolution dielectric characterization
In preparation

8.3 Acknowledgements

I would like to thank all those who collaborated in a direct or indirect way in this work.

I especially want to express my thanks to my supervisor Gabriel Gomila guiding me all these years and contributing to this fruitful work.

Thanks also to all my group members for the good working atmosphere and constructive and motivating talks about scientific topics and non-scientific ones. I am especially grateful to Martin Edwards who spent lots of hours with me sharing his knowledge about electrochemistry and finite element simulations.

I also want to express my gratitude to all the external collaborators that helped me on my way who were amongst others Juan Manuel Artés and the group of Manel Puig.

Thanks to all my friends for their support, many of them I also found in IBEC.

Over all, my thank goes to my family, Gemma and Joana who gave me the love and energy to reach this point.

8.4 References

1. Binnig, G.; Rohrer, H.; Gerber, C.; Weibel, E. *Physical Review Letters* **1982,** 49, (1), 57-61.
2. Binnig, G.; Rohrer, H., SCANNING TUNNELING MICROSCOPY. In 1986; Vol. 30, pp 355-369.
3. Binnig, G.; Quate, C. F.; Gerber, C. *Physical Review Letters* **1986,** 56, (9), 930-933.
4. Umeda, N.; Ishizaki, S.; Uwai, H. *Journal of Vacuum Science & Technology B* **1991,** 9, (2), 1318-1322.
5. Kim, G. M.; Kawai, S.; Nagashio, M.; Kawakatsu, H.; Brugger, J. *Journal of Vacuum Science & Technology B* **2004,** 22, (4), 1658-1661.
6. Hantschel, T.; Niedermann, P.; Trenkler, T.; Vandervorst, W. *Applied Physics Letters* **2000,** 76, (12), 1603-1605.
7. De Wolf, P.; Geva, M.; Hantschel, T.; Vandervorst, W.; Bylsma, R. B. *Applied Physics Letters* **1998,** 73, (15), 2155-2157.
8. Eyben, P.; Xu, M.; Duhayon, N.; Clarysse, T.; Callewaert, S.; Vandervorst, W. *Journal of Vacuum Science & Technology B* **2002,** 20, (1), 471-478.
9. Matey, J. R.; Blanc, J. *Journal of Applied Physics* **1985,** 57, (5), 1437-1444.
10. Barrett, R. C.; Quate, C. F. *Journal of Applied Physics* **1991,** 70, (5), 2725-2733.
11. Shao, R.; Kalinin, S. V.; Bonnell, D. A. *Applied Physics Letters* **2003,** 82, (12), 1869-1871.
12. O'Hayre, R.; Lee, M.; Prinz, F. B. *Journal of Applied Physics* **2004,** 95, (12), 8382-8392.
13. Lee, D. T.; Pelz, J. P.; Bhushan, B., Scanning capacitance microscopy for thin film measurements. In 2006; Vol. 17, pp 1484-1491.
14. Pingree, L. S. C.; Hersam, M. C. *Applied Physics Letters* **2005,** 87, (23).
15. Fumagalli, L.; Ferrari, G.; Sampietro, M.; Casuso, I.; Martinez, E.; Samitier, J.; Gomila, G. *Nanotechnology* **2006,** 17, (18), 4581-4587.
16. Casuso, I.; Fumagalli, L.; Gomila, G.; Padros, E. *Applied Physics Letters* **2007,** 91, (6), 3.
17. Fumagalli, L.; Ferrari, G.; Sampietro, M.; Gomila, G. *Applied Physics Letters* **2007,** 91, (24).
18. Gomila, G.; Toset, J.; Fumagalli, L. *Journal of Applied Physics* **2008,** 104, (2), 024315-024315-8.
19. Fumagalli, L.; Ferrari, G.; Sampietro, M.; Gomila, G. *Nano Letters* **2009,** 9, (4), 1604-1608.
20. Ferrari, G.; Sampietro, M. *Review of Scientific Instruments* **2007,** 78, (9), 094703.

21. Lai, K.; Ji, M. B.; Leindecker, N.; Kelly, M. A.; Shen, Z. X. *Review of Scientific Instruments* **2007,** 78, (6).
22. Anlage, S.; Talanov, V.; Schwartz, A., Prinziples of Near-Field Microwave Microscopy. In *Scanning probe microscopy: Electrical and Electromechanical Phenomena at the Nanoscale*, Kalinin, S. V.; Gruverman, A., Eds. Springer: New York, 2006.
23. Gao, C.; Wei, T.; Duewer, F.; Lu, Y. L.; Xiang, X. D. *Applied Physics Letters* **1997,** 71, (13), 1872-1874.
24. Tabib-Azar, M.; Wang, Y. Q. *Ieee Transactions on Microwave Theory and Techniques* **2004,** 52, (3), 971-979.
25. Huber, H. P.; Moertelmaier, M.; Wallis, T. M.; Chiang, C. J.; Hochleitner, M.; Imtiaz, A.; Oh, Y. J.; Schilcher, K.; Dieudonne, M.; Smoliner, J.; Hinterdorfer, P.; Rosner, S. J.; Tanbakuchi, H.; Kabos, P.; Kienberger, F. *Review of Scientific Instruments* **2010,** 81, (11).
26. Lai, K.; Kundhikanjana, W.; Kelly, M. A.; Shen, Z. X. *Applied Physics Letters* **2008,** 93, (12).
27. Lai, K.; Kundhikanjana, W.; Kelly, M.; Shen, Z. X. *Review of Scientific Instruments* **2008,** 79, (6).
28. Takeuchi, O.; Ohrai, Y.; Yoshida, S.; Shigekawa, H. *Japanese Journal of Applied Physics Part 1-Regular Papers Brief Communications & Review Papers* **2007,** 46, (8B), 5626-5630.
29. Girard, P. *Nanotechnology* **2001,** 12, (4), 485-490.
30. Garcia, R.; Perez, R. *Surface Science Reports* **2002,** 47, (6-8), 197-301.
31. Cherniavskaya, O.; Chen, L. W.; Weng, V.; Yuditsky, L.; Brus, L. E. *Journal of Physical Chemistry B* **2003,** 107, (7), 1525-1531.
32. Nonnenmacher, M.; Oboyle, M. P.; Wickramasinghe, H. K. *Applied Physics Letters* **1991,** 58, (25), 2921-2923.
33. Knapp, H. F.; Mesquida, P.; Stemmer, A. *Surface and Interface Analysis* **2002,** 33, (2), 108-112.
34. Goodman, T.; Bussmann, E.; Williams, C.; Taveras, M.; Britt, D. *Langmuir* **2004,** 20, (9), 3684-3689.
35. Datta, S. S.; Strachan, D. R.; Mele, E. J.; Johnson, A. T. C. **2009,** 9, (1), 7-11.
36. Meoded, T.; Shikler, R.; Fried, N.; Rosenwaks, Y. *Applied Physics Letters* **1999,** 75, (16), 2435-2437.
37. Shikler, R.; Fried, N.; Meoded, T.; Rosenwaks, Y. *Physical Review B* **2000,** 61, (16), 11041-11046.
38. Hu, J.; Xiao, X. D.; Salmeron, M. *Applied Physics Letters* **1995,** 67, (4), 476-478.
39. Salmeron, M.; Xu, L.; Hu, J.; Dai, Q. *Mrs Bulletin* **1997,** 22, (8), 36-41.
40. Verdaguer, A.; Sacha, G. M.; Bluhm, H.; Salmeron, M. *Chemical Reviews* **2006,** 106, (4), 1478-1510.
41. Hu, J.; Xiao, X. D.; Ogletree, D. F.; Salmeron, M. *Surface Science* **1995,** 344, (3), 221-236.
42. Hu, J.; Xiao, X. D.; Ogletree, D. F.; Salmeron, M. *Science* **1995,** 268, (5208), 267-269.
43. Hu, J.; Xiao, X. D.; Ogletree, D. F.; Salmeron, M. *Surface Science* **1995,** 327, (3), 358-370.

44. Bard, A. J.; Faulkner, L. R., *Electrochemical Methods: Fundamentals and Applications.* 2nd Revised edition ed.; 2001.
45. von Helmholtz, H. L. F. *Annalen der Physik* **1853,** 89, (211).
46. Chapman, D. L. *Philosophical Magazine* **1913,** 25, (148), 475-481.
47. Bazant, M. Z.; Thornton, K.; Ajdari, A. *Physical Review E* **2004,** 70, (2).
48. Kilic, M. S.; Bazant, M. Z.; Ajdari, A. *Physical Review E* **2007,** 75, (2).
49. Kilic, M. S.; Bazant, M. Z.; Ajdari, A. *Physical Review E* **2007,** 75, (2).
50. Olesen, L. H.; Bazant, M. Z.; Bruus, H. *Physical Review E* **2010,** 82, (1).
51. Ludwig, M.; Kranz, C.; Schuhmann, W.; Gaub, H. E. *Review of Scientific Instruments* **1995,** 66, (4), 2857-2860.
52. Macpherson, J. V.; Unwin, P. R. *Analytical Chemistry* **2000,** 72, (2), 276-285.
53. Eckhard, K.; Schuhmann, W. *Analyst* **2008,** 133, (11), 1486-1497.
54. Kim, S.; Yoo, H.; Lee, K.; Friedman, B.; Gaspar, M. A.; Levicky, R. *Applied Physics Letters* **2005,** 86, (15).
55. Parsegia.Va; Gingell, D. *Biophysical Journal* **1972,** 12, (9), 1192-&.
56. Israelachvili, J. N., *Intermolecular and Surface Forces* Third Edition ed.; 2011
57. Butt, H. J. *Biophysical Journal* **1991,** 60, (4), 777-785.
58. Butt, H. J.; Cappella, B.; Kappl, M. *Surface Science Reports* **2005,** 59, (1-6), 1-152.
59. Pericet-Camara, R.; Papastavrou, G.; Behrens, S. H.; Borkovec, M. *Journal of Physical Chemistry B* **2004,** 108, (50), 19467-19475.
60. Butt, H. J. *Biophysical Journal* **1991,** 60, (6), 1438-1444.
61. Raiteri, R.; Grattarola, M.; Butt, H. J. *Journal of Physical Chemistry* **1996,** 100, (41), 16700-16705.
62. Doppenschmidt, A.; Butt, H. J. *Colloids and Surfaces a-Physicochemical and Engineering Aspects* **1999,** 149, (1-3), 145-150.
63. Hillier, A. C.; Kim, S.; Bard, A. J. *Journal of Physical Chemistry* **1996,** 100, (48), 18808-18817.
64. Giesbers, M.; Kleijn, J. M.; Stuart, M. A. C. *Journal of Colloid and Interface Science* **2002,** 248, (1), 88-95.
65. Wang, J.; Bard, A. J. *Journal of Physical Chemistry B* **2001,** 105, (22), 5217-5222.
66. Barten, D.; Kleijn, J. M.; Duval, J.; von Leeuwen, H. P.; Lyklema, J.; Stuart, M. A. C. *Langmuir* **2003,** 19, (4), 1133-1139.
67. Hu, K.; Fan, F. R. F.; Bard, A. J.; Hillier, A. C. *Journal of Physical Chemistry B* **1997,** 101, (41), 8298-8303.
68. Rentsch, S.; Siegenthaler, H.; Papastavrou, G. *Langmuir* **2007,** 23, (17), 9083-9091.
69. Yang, Y.; Mayer, K. M.; Hafner, J. H. *Biophysical Journal* **2007,** 92, (6), 1966-1974.
70. Yang, Y.; Mayer, K. M.; Wickremasinghe, N. S.; Hafner, J. H. *Biophysical Journal* **2008,** 95, (11), 5193-5199.
71. Johnson, A. S.; Nehl, C. L.; Mason, M. G.; Hafner, J. H. *Langmuir* **2003,** 19, (24), 10007-10010.
72. Heinz, W. F.; Hoh, J. H. *Biophysical Journal* **1999,** 76, (1), 528-538.
73. Sotres, J.; Baro, A. M. *Applied Physics Letters* **2008,** 93, (10).

74. Hirata, Y.; Mizutani, F.; Yokoyama, H. *Surface and Interface Analysis* **1999,** 27, (5-6), 317-323.
75. Raiteri, R.; Butt, H. J. *Journal of Physical Chemistry* **1995,** 99, (43), 15728-15732.
76. Umeda, K.-i.; Oyabu, N.; Kobayashi, K.; Hirata, Y.; Matsushige, K.; Yamada, H. *Applied Physics Express* **2010,** 3, (6).
77. Kobayashi, N.; Asakawa, H.; Fukuma, T. *Review of Scientific Instruments* **2010,** 81, (12).
78. Kao, K. C., *Dielectric Phenomena in Solids*. 2004.
79. Erlandsson, R.; McClelland, G. M.; Mate, C. M.; Chiang, S. *Journal of Vacuum Science & Technology a-Vacuum Surfaces and Films* **1988,** 6, (2), 266-270.
80. Hudlet, S.; Saint Jean, M.; Guthmann, C.; Berger, J. *The European Physical Journal B - Condensed Matter and Complex Systems* **1998,** 2, (1), 5-10.
81. Krayev, A. V.; Talroze, R. V. *Polymer* **2004,** 45, (24), 8195-8200.
82. Krayev, A. V.; Shandryuk, G. A.; Grigorov, L. N.; Talroze, R. V. *Macromolecular Chemistry and Physics* **2006,** 207, (11), 966-969.
83. Lu, W.; Wang, D.; Chen, L. W. *Nano Letters* **2007,** 7, 2729-2733.
84. Smythy, *Static and Dynamic Electricity*. McGraw-Hill: New York, 1968.
85. Sacha, G. M.; Sahagun, E.; Saenz, J. J. *Journal of Applied Physics* **2007,** 101, (2), 024310-024310-4.
86. Sacha, G. M.; Saenz, J. J. *Applied Physics Letters* **2004,** 85, (13), 2610-2612.
87. Abraham, D. W.; Martin, Y.; Wickramasinghe, K. **1988,** 897, 191-8.
88. Hao, H. W.; Baro, A. M.; Saenz, J. J. *Journal of Vacuum Science & Technology B* **1991,** 9, (2), 1323-1328.
89. Belaidi, S.; Girard, P.; Leveque, G. *Journal of Applied Physics* **1997,** 81, (3), 1023-1030.
90. Law, B. M.; Rieutord, F. *Physical Review B* **2002,** 66, (3).
91. Gramse, G.; Casuso, I.; Toset, J.; Fumagalli, L.; Gomila, G. *Nanotechnology* **2009,** 20, (39).
92. Shen, Y. X.; Barnett, D. M.; Pinsky, P. M. *Applied Physics Letters* **2008,** 92, (13).
93. Coster, H. G. L. *Journal of Biological Physics* **2003,** 29, (4), 363-399.
94. Stern, J. E.; Terris, B. D.; Mamin, H. J.; Rugar, D. *Applied Physics Letters* **1988,** 53, (26), 2717-2719.
95. Kalinin, S. V.; Karapetian, E.; Kachanov, M. *Physical Review B* **2004,** 70, (18), 184101.1-184101.24.
96. Lynch, B. P.; Hilton, A. M.; Simpson, G. J. *Biophysical Journal* **2006,** 91, (7), 2678-2686.
97. Cho, Y. S.; Kirihara, A.; Saeki, T. *Review of Scientific Instruments* **1996,** 67, (6), 2297-2303.
98. Gao, C.; Xiang, X. D. *Review of Scientific Instruments* **1998,** 69, (11), 3846-3851.
99. Krauss, T. D.; Brus, L. E. *Physical Review Letters* **1999,** 83, (23), 4840.
100. Cherniavskaya, O.; Chen, L.; Weng, V.; Yuditsky, L.; Brus, L. E. *Journal of Physical Chemistry* **2003,** 107, (7), 1525-1531.
101. Staii, C.; Johnson, A. T.; Pinto, N. J. *Nano Letters* **2004,** 4, (5), 859-862.

102. Crider, P. S.; Majewski, M. R.; Jingyun, Z.; Oukris, H.; Israeloff, N. E. *Applied Physics Letters* **2007,** 91, (1), 013102.
103. Clausen, C. H.; Jensen, J.; Castillo, J.; Dimaki, M.; Svendsen, W. E. *Nano Letters* **2008,** 8, (11), 4066-4069.
104. Lhernould, M. S.; Delchambre, A.; Régnier, S.; Lambert, P. *Applied Surface Science* **2007,** 253, (14), 6203-6210.
105. Toset, J.; Casuso, I.; Samitier, J.; Gomila, G. *Nanotechnology* **2007,** 18, (1), 015503.
106. Oesterhelt, D.; Stoeckenius, W. *Proceedings of the National Academy of Sciences* **1973,** 70, (10), 2853-2857.
107. Ltd, C. R., *Silica and Silicon Dioxide - Properties*. 2008.
108. Gomez-Monivas, S.; Froufe, L. S.; Carminati, R.; Greffet, J. J.; Saenz, J. J. *Nanotechnology* **2001,** 12, (4), 496-499.
109. Hutter, J. L.; Bechhoefer, J. *Review of Scientific Instruments* **1993,** 64, (7), 1868-1873.
110. Palacios-Lidon, E.; Colchero, J. *Nanotechnology* **2006,** 17, 5491-5500.
111. Riedel, C.; Arinero, R.; Tordjeman, P.; Leveque, G.; Schwartz, G. A.; Alegria, A.; Colmenero, J. *Physical Review E* **2010,** 81, (1).
112. Riedel, C.; Sweeney, R.; Israeloff, N. E.; Arinero, R.; Schwartz, G. A.; Alegria, A.; Tordjeman, P.; Colmenero, J. *Applied Physics Letters* **2010,** 96, (21).
113. Shen, Y.; Barnett, D. M.; Pinsky, P. M. *Engineering Analysis with Boundary Elements* **2008,** 32, (8), 682-691.
114. Sacha, G. M.; Cardellach, M.; Segura, J. J.; Moser, J.; Bachtold, A.; Fraxedas, J.; Verdaguer, A. *Nanotechnology* **2009,** 20, (28).
115. Miccio, L. A.; Kummali, M. M.; Montemartini, P. E.; Oyanguren, P. A.; Schwartz, G. A.; Alegria, A.; Colmenero, J. *Journal of Chemical Physics* **2011,** 135, (6).
116. Zhao, M.; Gu, X.; Lowther, S. E.; Park, C.; Jean, Y. C.; Nguyen, T. *Nanotechnology* **2010,** 21, (22).
117. Mikamo-Satoh, E.; Yamada, F.; Takagi, A.; Matsumoto, T.; Kawai, T. *Nanotechnology* **2009,** 20, (14).
118. Benitez, J. J.; de la Fuente, O. R.; Diez-Perez, I.; Sanz, F.; Salmeron, M. *Journal of Chemical Physics* **2005,** 123, (10).
119. Sacha, G. M.; Gomez-Navarro, C.; Saenz, J. J.; Gomez-Herrero, J. *Applied Physics Letters* **2006,** 89, (17).
120. Takagi, A.; Yamada, F.; Matsumoto, T.; Kawai, T. *Nanotechnology* **2009,** 20, (36).
121. Gramse, G.; Gomila, G.; Fumagalli, L. *Nanotechnology* **2012,** 23, (20), 205703.
122. Fumagalli, L.; Gramse, G.; Esteban-Ferrer, D.; Edwards, M. A.; Gomila, G. *Applied Physics Letters* **2010,** 96, (18).
123. Fumagalli, L.; Gramse, G.; Dols-Peréz, A.; Gomila, G. **in preparation**.
124. Scheuring, S.; Seguin, J.; Marco, S.; Levy, D.; Robert, B.; Rigaud, J. L. *Proceedings of the National Academy of Sciences of the United States of America* **2003,** 100, (4), 1690-1693.

125. Cross, S. E.; Jin, Y.-S.; Rao, J.; Gimzewski, J. K. *Nature Nanotechnology* **2007,** 2, (12), 780-783.
126. Manne, S.; Hansma, P. K.; Massie, J.; Elings, V. B.; Gewirth, A. A. *Science* **1991,** 251, (4990), 183-186.
127. Rico, F.; Su, C.; Scheuring, S. *Nano Letters* **2011,** 11, (9), 3983-3986.
128. Alonso, J. L.; Goldmann, W. H. *Life Sciences* **2003,** 72, (23), 2553-2560.
129. Ivanovska, I. L.; de Pablo, P. J.; Ibarra, B.; Sgalari, G.; MacKintosh, F. C.; Carrascosa, J. L.; Schmidt, C. F.; Wuite, G. J. L. *Proceedings of the National Academy of Sciences of the United States of America* **2004,** 101, (20), 7600-7605.
130. Wittstock, G.; Burchardt, M.; Pust, S. E.; Shen, Y.; Zhao, C. *Angewandte Chemie-International Edition* **2007,** 46, (10), 1584-1617.
131. Kalinin, S. V.; Bonnell, D. A. *Physical Review B* **2002,** 65, (12).
132. Rodriguez, B. J.; Jesse, S.; Baddorf, A. P.; Kalinin, S. V. *Physical Review Letters* **2006,** 96, (23).
133. Lu, W.; Xiong, Y.; Hassanien, A.; Zhao, W.; Zheng, M.; Chen, L. *Nano Letters* **2009,** 9, (4), 1668-1672.
134. Sounart, T. L.; Panchawagh, H. V.; Mahajan, R. L. *Applied Physics Letters* **2010,** 96, (20).
135. Malmivuo, J.; Plonsey, J. R., *Bioelectromagnetism: principles and applications of bioelectric and biomagnetic fields*. Oxford University Press: New York, 1995.
136. Dilger, J. P.; McLaughlin, S. G. A.; McIntosh, T. J.; Simon, S. A. *Science* **1979,** 206, (4423), 1196-1198.
137. Warshel, A.; Sharma, P. K.; Kato, M.; Parson, W. W., Modeling electrostatic effects in proteins. In 2006; Vol. 1764, pp 1647-1676.
138. van Meer, G.; Voelker, D. R.; Feigenson, G. W. *Nature Reviews Molecular Cell Biology* **2008,** 9, (2), 112-124.
139. Huang, W.; Levitt, D. G., Theoretical Calculation Of Dielectric-Constant Of A Bilayer Membrane. In 1977; Vol. 17, pp 111-128.
140. Stern, H. A.; Feller, S. E. *Journal of Chemical Physics* **2003,** 118, (7), 3401-3412.
141. Nymeyer, H.; Zhou, H.-X. *Biophysical Journal* **2008,** 94, (4), 1185-1193.
142. Steinem, C.; Janshoff, A.; Ulrich, W. P.; Sieber, M.; Galla, H. J. *Biochimica Et Biophysica Acta-Biomembranes* **1996,** 1279, (2), 169-180.